

The Development and Stability of Palladium-based Thin Films for Hydrogen-related Energy Applications

Verma, N.

DOI

[10.4233/uuid:fad3199c-59c9-4ffc-975c-8a4690085c39](https://doi.org/10.4233/uuid:fad3199c-59c9-4ffc-975c-8a4690085c39)

Publication date

2022

Document Version

Final published version

Citation (APA)

Verma, N. (2022). *The Development and Stability of Palladium-based Thin Films for Hydrogen-related Energy Applications*. [Dissertation (TU Delft), Delft University of Technology].
<https://doi.org/10.4233/uuid:fad3199c-59c9-4ffc-975c-8a4690085c39>

Important note

To cite this publication, please use the final published version (if applicable).
Please check the document version above.

Copyright

Other than for strictly personal use, it is not permitted to download, forward or distribute the text or part of it, without the consent of the author(s) and/or copyright holder(s), unless the work is under an open content license such as Creative Commons.

Takedown policy

Please contact us and provide details if you believe this document breaches copyrights.
We will remove access to the work immediately and investigate your claim.



The Development and Stability of Palladium-based Thin Films for Hydrogen-related Energy Applications

Neha Verma

The Development and Stability of Palladium-based Thin Films
for Hydrogen-related Energy Applications

NEHA VERMA

ISBN: 978-94-6384-358-4

The Development and Stability of Palladium-based Thin Films
for Hydrogen-related Energy Applications

Dissertation

for the purpose of obtaining the degree of doctor
at Delft University of Technology,
by the authority of the Rector Magnificus prof.dr.ir. T.H.J.J. van der Hagen,
chair of the Board for Doctorates,
to be defended publicly on
Wednesday 14 September 2022 at 12:30 o'clock

by

Neha VERMA

Master of Science in Materials Chemistry,
University of Eastern Finland, Joensuu, Finland

Master of Science in Chemistry,
Panjab University, Chandigarh, India

born in Shimla, India

This dissertation has been approved by the promotor.

Composition of the doctoral committee:

Rector Magnificus,	Chairperson
Dr. A.J. Böttger	Delft University of Technology, promotor
Prof. dr. ir. J. Sietsma	Delft University of Technology, copromotor

Independent members:

Prof. dr. B. Dam	Delft University of Technology
Prof. dr. ir. J.M.C. Mol	Delft University of Technology
Prof. dr. O. Thomas	Aix-Marseille Université (France)
Dr. S. Eswara Moorthy	Luxembourg Institute of Science and Technology
Dr. ir. R.H. Vegter	SKF (The Netherlands)



The research described in this thesis was carried out in the Department of Materials Science and Engineering, Faculty of Mechanical, Maritime and Materials Engineering. This research was supported by the Delft University of Technology.

Keywords: Hydrogen energy, Palladium thin films, Adhesive intermediate layers, X-Ray Diffraction, Microstructure, Morphology, Stress, Texture, Dislocations

An electronic version of this dissertation is available at: <http://repository.tudelft.nl/>

Printed by: ProefschriftMaken // www.proefschriftmaken.nl

Front and back cover photos: Optical microscopic images of ~100 nm Palladium thin film

Copyright © 2022 by Neha Verma

Author e-mail: chem.neha@gmail.com | N.Verma@tudelft.nl

All rights reserved. No part of the material protected by this copyright notice may be reproduced or utilized in any form or by any means, electronically or mechanically, including photocopying, recording or by any information storage and retrieval system, without written permission from the author.

Contents

Summary	1
Samenvatting.....	5
CHAPTER-1: Introduction	11
1.1. Background.....	11
1.2. The Pd-H system	12
1.3. Pd-based nanocrystalline thin films.....	13
1.4. Scope and outline of the thesis	15
1.5. References	17
CHAPTER-2: Controlling morphology and texture of sputter-deposited Pd films by tuning the surface topography of the (Ti) adhesive layer	21
2.1. Introduction	22
2.2. Materials and methods.....	24
2.2.1. Thin film sputter deposition	24
2.2.2. Scanning Transmission Electron Microscopy (STEM).....	24
2.2.3. Atomic Force Microscopy (AFM).....	25
2.2.4. X-Ray Diffraction (XRD).....	25
2.2.4.1. Ti layer thickness.....	25
2.2.4.2. Pd thin film texture	25
2.2.4.3. <i>In-situ</i> XRD hydrogen absorption	26
2.2.4.4. Kinetic equation.....	27
2.3. Results and discussion	27
2.3.1. Atomic Force Microscopy	28
2.3.1.1. Ti layer surface topography	28
2.3.2. Scanning Transmission Electron Microscopy	33
2.3.2.1. Ti intermediate layer characterization	33
2.3.2.2. Pd thin film morphology	35
2.3.3. X-Ray Diffraction.....	37

2.3.3.1. Pd films: Texture strength and sharpness	37
2.3.3.2. Pd films: Hydrogen absorption kinetics	39
2.4. Conclusion	44
2.5. References	45
CHAPTER-3: The role of the substrate on the mechanical and thermal stability of Pd thin films during hydrogen (de)sorption	49
3.1. Introduction	50
3.2. Experimental.....	52
3.2.1. Pd thin film preparation.....	52
3.2.2 TEM and SEM: morphology analysis	52
3.2.3. X-ray diffraction (XRD).....	53
3.2.3.1. Texture and stress measurements	53
3.2.3.2. XRD line-broadening: microstructure characterization	54
3.2.4. Experimental set-up for <i>in-situ</i> hydriding	55
3.2.4.1. Room-temperature.....	56
3.2.4.2. Above room-temperature.....	56
3.2.4.2.1. Phase transitions: 303 K – 353 K (PT-only)	56
3.2.4.2.2. High-temperature annealing prior to phase transitions (HT+PT).....	57
3.3. Results and discussion	57
3.3.1. As-prepared Pd thin film microstructure	57
3.3.1.1. Morphology	57
3.3.1.2. Crystallographic texture	60
3.3.1.3. Stress.....	62
3.3.2. Phase transformations: mechanical and thermal stability.....	63
3.3.2.1. Room temperature	63
3.3.2.2. Above room-temperature.....	66
3.3.2.2.1. Phase transitions: 303 K – 353 K (PT-only)	66
3.3.2.2.2. High-temperature annealing prior to phase transitions (HT+PT).....	69

3.3.3. Microstructure from XRD line-broadening	72
3.3.4. Deformation mechanism	75
3.3.4.1. Deformation during phase transitions (PT-only).....	75
3.3.3.2. Deformation in annealed Pd thin films (HT+PT).....	76
3.4. Conclusion	77
3.5. References	77
CHAPTER-4: Stress development in hydrogenated nano-columnar Pd and Pd on Ti thin films.....	83
4.1. Introduction	84
4.2. Experimental.....	84
4.2.1. Pd thin film preparation.....	84
4.2.2. X-ray diffraction measurement.....	85
4.2.2.1. <i>In-situ</i> ω -tilt stress measurement during Pd phase transformation.....	85
4.2.2.2. <i>Ex-situ</i> ψ -tilt stress measurement after hydrogen cycling experiment	86
4.2.3. Stress analysis.....	86
4.3. Results and Discussion	86
4.3.1. Stress analysis: $\text{Sin}^2\psi$ method.....	87
4.4. Conclusion	92
4.5. References	93
CHAPTER-5: Dislocations, texture and stress development in hydrogen-cycled Pd thin films: an <i>in-situ</i> X-ray diffraction study.....	95
5.1. Introduction	96
5.2. Experimental.....	98
5.2.1. Pd thin film preparation.....	98
5.2.2. X-ray diffraction (XRD).....	99
5.2.2.1. Focusing optics diffractometer: Hydrogen cycling	99
5.2.2.2. Parallel-beam diffractometer: Hydrogen cycling	100
5.2.2.3. Texture and stress measurements	101

5.2.2.4. XRD line-broadening: microstructure characterization	101
5.3. Results and discussion	103
5.3.1. Morphology analysis: evolution during cycling.....	103
5.3.2. Texture analysis: Quantification of weak and broad fiber texture	108
5.3.2.1. Texture results for Pd thin films	111
5.3.3. Stress analysis.....	112
5.3.3.1. ω -tilt stress: $\sin^2\psi$ method	112
5.3.3.2. ψ -tilt stress: combining crystallite group method and $\sin^2\psi$ method	113
5.3.4. Defects from XRD line-broadening	117
5.4. Conclusion	121
5.5. References	121
APPENDICES	129
APPENDIX A: Supplementary material to Chapter 3	129
APPENDIX B: Supplementary material to Chapter 5	133
Acknowledgements	151
Publications	155
Curriculum vitae	157

*There is a unique place for every star in the sky,
you don't lose your place if someone else also touches the high.*

SUMMARY

Summary

Pure palladium (Pd) undergoes a phase transformation ($\alpha \rightarrow \beta$) below a critical temperature and pressure in the presence of hydrogen. The transition to β -PdH_x is accompanied by a large volume expansion of about 10%, resulting in plastic deformation and hydrogen embrittlement. This thesis investigates the relation between microstructure (change) and mechanical properties of Pd-based thin films with the goal to develop a stable material for various energy-related applications to support the hydrogen economy. The main focus is on developing pure Pd thin films with open columnar morphology, which has shown resistance to hydrogen embrittlement induced by absorption and desorption of hydrogen and the consequent $\alpha \leftrightarrow \beta$ phase transitions. To realize this, ~ 100 nm thick Pd films are magnetron sputter deposited at room temperature on an oxidized Si wafer substrate (SiO₂/Si). The deposition conditions are optimized based on Thornton's structure zone model to attain desired Pd thin film microstructures. Additionally, adhesive intermediate layers are placed between the thin film and the stiff substrate to enhance the lifetime of Pd thin films when exposed to hydrogen cycling. In view of this, the thesis engages in step-wise investigations to characterize the microstructural properties of hydrogen cycled Pd thin films. In this summary, the main scientific outcomes are compiled with reference to the thesis chapters.

Chapter 2 closely monitors the film-substrate interface in Pd on Ti thin films to adapt the surface topography of the Ti layer, used as an adhesive intermediate layer, intending to control the Pd film microstructure (morphology and texture). A series of Ti layers with a range of thicknesses (1 nm, 3 nm, and 6 nm) at two Ar pressures (0.4 Pa and 3 Pa) are magnetron sputter deposited on a SiO₂/Si substrate. Atomic Force Microscopy analysis shows the formation of closely packed small (few nm) Ti islands resulting in a smooth surface at low Ar pressure, while high Ar pressure leads to a rough surface with widely spaced large Ti islands. Due to this difference in Ti layer growth mechanism, regardless of Pd deposition conditions, the optimized open columnar morphology of the Pd film is diversified (difference in openness close to the substrate and top), eventually leading to dissimilar hydriding properties. The observed variation in morphological features of Pd film is ascribed to the fact that at the early stage of deposition, there is an influence of the substrate surface, which weakens with increasing Pd film thickness. This is understood in terms of the intermediate

layer surface conditions and the resulting Pd adatom diffusion and shadowing effects during the sputtering. Transmission Electron Microscopy (TEM) morphology and X-Ray Diffraction (XRD) texture analysis confirm that for Ti sputter conditions which results in a smooth Ti surface, the Pd film develops with compact morphology and sharp 111-fiber texture.

The hydrogen absorption performance is assessed by following the transformation to β -phase during room temperature (RT) hydriding utilizing in-situ XRD. The time-dependent kinetic curves fitted with various rate equations, used to determine the reaction mechanism of hydrogen absorption, suggest different reaction stages for Pd on Ti films, depending on the growth microstructure. The slow incubation stage is present for both compact and partially compact morphologies for Pd films on Ti but is absent for both Pd on a bare substrate and Pd on Ti films with open morphology. The final stage, which is dominated by 3-dimensional diffusion, is present in all types of Pd films on Ti. This stage is associated in the compact Pd layer with the slow phase transformation of small grains near the Ti layer, as observed in TEM images.

After having investigated the Pd on a bare substrate and Pd on Ti film's microstructural stability during hydriding at RT, the impact of annealing on the performance of the Pd thin film is addressed in chapter 3. More specifically, to apprehend the role of the morphological features on hydriding, Pd thin films with closed (series-1) and open (series-2) columnar morphology are sputter deposited. A comprehensive in situ XRD experimental study at RT, above RT (phase transitions: PT-only), and at high-temperature annealing before phase transitions (HT+PT) provides detailed insight into hydrogen-induced mechanical behavior. For the direct visualization of the specimen surface, a custom-made *in-situ* XRD set-up on a parallel-beam diffractometer is developed. Based on this it is concluded that the lack of voids to accommodate the β -PdH_x phase expansion results in buckle-delamination in compact Pd thin film, while the film with open morphology does not show any hydride-related topographical changes. Introducing adhesive layers – Titanium (Ti) and Polyimide (PI) in closed morphology films– deters buckle formation, but slows down hydride formation. Hydride formation times up to 18 hours are found whereas for Pd films on a bare substrate hydride formation typically occurs in less than 10 mins. These findings suggest that along with open columnar morphology, a strong clamping effect is a dominant factor to strengthen the Pd thin film system.

By using annealing as a probe, the critical temperature at which as-deposited open morphology remains unaltered is explored. Depending on the presence of the intermediate layer high temperature (HT) annealing significantly impacts phase transitions and stability.

Morphology evolution from TEM and Scanning Electron Microscopy (SEM) shows that for temperatures up to 353 K, neither coalescence nor grain growth occurs. The dewetting phenomena start at 473 K when agglomeration starts, resulting in the formation of spherical nanopores. The differences in the number density and the shapes of the annealing-induced nanopores, reflect the difference in film-substrate interaction. For Pd on Ti and Pd on PI films, the as-deposited microcracks that disappear to form large globular nanopores during HT annealing, reappear as wide microcracks after PT. These microcracks indicate an effective mechanism of local stress reduction, thus mitigating the potential hydriding damage. However, due to poor adhesion of the Pd film on a SiO₂/Si substrate, a crack + buckle network propagates, leading to eventual film delamination after HT+PT annealing, as found for closed morphology Pd film after hydriding at RT.

Furthermore, to assess the deformation mechanism in terms of defect parameters a procedure is developed for line-broadening analysis of XRD profiles using the integral breadth. The modified Williamson-Hall plots indicate that in open morphology films, microstrain is caused by the presence of dislocations. It is shown that after PT-only the added free surface, generated by microcracking in the Pd film, helps to reduce the dislocation density while in Pd on Ti film, an increase is due to the rigid substrate so that dislocations pile-up against the film-substrate interface. The Pd on PI film shows a small decrease in dislocation density and almost no microcracks, suggesting that a PI layer allows some strain relaxation inside the Pd crystallites by its flexibility. Thus, a microstructural stabilization mechanism occurs that implies some freedom to expand/contract during hydrogen loading/deloading so that some stress relaxation occurs along open grain boundaries.

Chapters 4 and 5 of this thesis are dedicated to 20 hydrogen loading/deloading cycling (20-L/D) experiments on open morphology (series-2) Pd thin films. Pd thin films with identical microstructures (morphology, stress, and texture) are studied in these chapters to construe the influence of substrate type (film-substrate interface) as a function of hydrogen cycling.

In chapter 4, a method is developed that allows an *in-situ* stress measurement during hydriding on an XRD set-up with focusing geometry. The measurement procedure employs instrumental tilt (ω -tilt) to the sample where ω is the angle between the incident X-ray beam and the sample surface. Various hydrogen L/D experiments on the same set-up are performed to test the applicability of the ω -tilt method for reliable *in-situ* stress results. To encounter the low intensity, asymmetry, and poor profile shape of high angle reflections, peak positions are deduced by various peak fitting methods. It is found that the threshold intensity of 40% of the

maximum intensity is useful to avoid overlapping regions between peaks. The method is tested on open morphology Pd on a bare substrate and Pd on Ti films during 20-L/D cycling, the stress evolution shows agreement with the *ex-situ* ψ -tilt stress measured in parallel-beam geometry.

The ω -tilt stress measurement technique is again validated in chapter 5 by performing 20 L/D cycling tests on an *in-situ* set-up in parallel-beam geometry (ψ -tilt). Additionally, the XRD set-up with a holder covered by a transparent foil shows the absence of buckle formation during hydrogen loading (20 cycles) for all Pd thin films. SEM investigation demonstrates microcrack propagation from a fine web-like network to scattered wide cracks, leading further to buckle-delamination (after 10 cycles) in Pd thin film without an adhesive layer, highlighting the gradual release of stress through evolving film morphology. However, Pd on Ti and Pd on PI films show controlled microcrack widening and remain strongly adhered to the substrate even after 20 cycles. This chapter also presents an easy approach to evaluate stress in Pd thin films that are macroscopically elastically anisotropic by combining the Crystallite Group Method and the $\text{Sin}^2\psi$ -method. The Pd thin films studied in this thesis show fiber texture. A stepwise method is dedicated to calculate the volume fraction of texture components from the fiber texture plot, defined as the density of poles, which is proportional to the diffraction peak integral intensity. This method is first established for strong fiber-textured films with a compact morphology and based on this the volume fraction of $\langle 111 \rangle$ crystallites and random components are calculated for open morphology films.

In accordance with chapter 3, it is concluded that randomly oriented pure screw dislocations of the $\{111\}$, $a/2\langle 110 \rangle$ slip system led to the best fit for modified Williamson Hall plots. The general trend shows an increase in dislocation density with cycling for Pd on Ti film, while for Pd on a bare substrate and Pd on PI films a gradual decrease is observed. In the bare Pd film the buckled region has two free surfaces that allow dislocations to escape, whereas, for Pd on PI film, the dislocations are annihilated at the crystalline-amorphous interface with the PI layer acting as a perfect dislocation sink as required. Furthermore, the defect analysis shows the reversible pattern of crystallite size and dislocation motion when stresses change between tensile and compressive stresses during hydrogen cycling. This cyclic deformation also results in an irreversible texture change, which implies sharpening of the $\{111\}$ -fiber texture for all Pd thin films with open morphology.

The outcomes from these chapters support the utilization of Pd as a material for applications in several hydrogen technologies.

Samenvatting

Zuiver palladium (Pd) ondergaat een faseovergang ($\alpha \rightarrow \beta$) beneden de kritische temperatuur en druk in aanwezigheid van waterstof. De overgang naar β -hydride gaat gepaard met een grote volume-expansie van ongeveer 10%, resulterend in plastische vervorming en waterstofverbrossing. Dit proefschrift onderzoekt de relatie tussen microstructuur en mechanische eigenschappen van dunne Pd films met als doel een stabiel materiaal te ontwikkelen voor energie-gerelateerde toepassingen voor de waterstofeconomie. De focus ligt op het ontwikkelen van dunne films van zuiver Pd met een open kolomvormige morfologie, die beter bestand zijn tegen verbrossing door absorptie van waterstof en de daaruit voortvloeiende $\alpha \leftrightarrow \beta$ faseovergangen. Om dit te realiseren worden, ~ 100 nm dikke Pd films gedeponerd met magnetronspuiting bij kamertemperatuur op een geoxideerd Si substraat (SiO_2/Si). De depositievoorwaarden zijn geoptimaliseerd op basis van Thornton's structuurzonemodel zodat de gewenste microstructuur van de Pd dunne film wordt verkregen. Bovendien worden adhesieve lagen aangebracht tussen de dunne film en het stijve substraat om de levensduur van de dunne Pd films te verlengen bij blootstelling aan waterstofcycli. Met het oog hierop wordt in dit proefschrift systematisch onderzoek gedaan naar de microstructurele veranderingen van Pd dunne films tijdens waterstofcycli. In deze samenvatting worden de belangrijkste wetenschappelijke resultaten beschreven met verwijzing naar de hoofdstukken in dit proefschrift.

In hoofdstuk 2 wordt het grensvlak tussen film en substraat in dunne films Pd op Ti nauwkeurig geanalyseerd om de oppervlakte-topografie van de Ti laag (gebruikt als hechtende tussenlaag) aan te passen zodat een welbepaalde microstructuur van de Pd film (morfologie en textuur) gevormd wordt. Een reeks Ti lagen met verschillende diktes (1 nm, 3 nm, en 6 nm) worden bij twee Ar drukken (0.4 Pa en 3 Pa) met magnetronspuiting op een geoxideerd Si substraat gedeponerd. Atomic Force Microscopy analyse toont aan dat bij lage Ar druk dicht opgepakte kleine (enkele nm) Ti eilanden gevormd worden hetgeen resulteert in een glad oppervlak, terwijl een hoge Ar druk leidt tot een ruw oppervlak met ver uit elkaar liggende grotere Ti eilanden. Door dit verschil in het groeimechanisme van de Ti laag is, onafhankelijk van de condities van de Pd depositie, de open kolomvormige morfologie van de Pd film gediversifieerd (verschil in openheid dicht bij het substraat en het bovenste deel), hetgeen uiteindelijk leidt tot verschillen in waterstofabsorptie eigenschappen. De

waargenomen variatie in morfologische kenmerken van de Pd film wordt toegeschreven aan het feit dat het substraatooppervlak van invloed is op het initiële stadium van deponeren, hetgeen afzwakt met toenemende Pd filmdikte. Dit wordt begrepen in termen van de topografie van de adhesielaag, en de resulterende Pd-adatoomdiffusie en schaduweffecten tijdens het sputteren. Transmissie Elektronen Microscopie (TEM) morfologieanalyse en Röntgendiffractie (XRD) textuuranalyse bevestigen dat voor Ti sputtercondities die resulteren in een glad Ti oppervlak, de Pd film een compacte morfologie en scherpe 111-vezeltextuur ontwikkelt.

De mate van waterstofabsorptie wordt bepaald door de transformatie naar de β -fase te volgen bij kamertemperatuur (RT) met behulp van in-situ XRD. Tijdsafhankelijke kinetische curven die passen bij de verschillende kinetische modellen worden gebruikt om het reactiemechanisme van waterstofabsorptie te bepalen. Deze suggereren verschillende reactiestadia voor Pd films op Ti afhankelijk van de gegroeide microstructuur. De langzame incubatiefase is aanwezig voor zowel compacte als gedeeltelijk compacte morfologieën voor Pd films op Ti, maar is afwezig voor zowel Pd op een kaal substraat als Pd op Ti met open morfologie. De laatste fase, die wordt gedomineerd door 3-dimensionale diffusie, is aanwezig in alle typen Pd films op Ti. Deze fase wordt in de compacte Pd laag geassocieerd met de langzame fase transformatie van kleine korrels nabij de Ti laag, die zijn waargenomen in TEM beelden.

Na het onderzoeken van de microstructurele stabiliteit van Pd op een kaal substraat en Pd op Ti tijdens hydridevorming bij kamertemperatuur (RT), wordt de invloed van gloeien op het gedrag van de Pd dunne film behandeld in hoofdstuk 3. In het bijzonder, om de rol van de morfologische kenmerken op hydridevorming te begrijpen, worden Pd dunne films met compacte (serie-1) en open (serie-2) kolomvormige morfologie gedeponerd. Een uitgebreide in situ XRD studie bij kamertemperatuur (RT), boven kamertemperatuur (faseovergangen: PT-only), en hoge-temperatuur gloeien vóór faseovergangen (HT+PT) biedt een gedetailleerd inzicht in waterstof-geïnduceerd mechanisch gedrag. Voor de directe visualisatie van het preparaatoppervlak is een op maat gemaakte in-situ XRD preparaatouder ontwikkeld. Op basis daarvan wordt geconcludeerd dat het ontbreken van holtes om de β -PdH_x fase-uitzetting te accommoderen resulteert in knik-delaminatie in compacte Pd dunne film, terwijl films met een open kolomstructuur geen hydride-gerelateerde topografische veranderingen vertonen. De introductie van een adhesielaag - Ti en polyimide (PI) in films met compacte morfologie verhinderen knikvorming, maar vertragen de hydridevorming. Tijden voor hydridevorming tot 18 uur worden gevonden, terwijl voor Pd films op een kaal substraat hydridevorming typisch

optreedt in minder dan 10 minuten. Deze bevindingen suggereren dat samen met de open kolomvormige morfologie, een sterk adhesie-effect een dominante factor is om het Pd dunne film systeem te versterken.

Door middel van gloeien wordt de kritische temperatuur onderzocht waarbij de open morfologie van de gedeponeerde film onveranderd blijft. Afhankelijk van de aanwezigheid van de tussenlaag heeft het gloeien bij hoge temperatuur (HT) een aanzienlijke invloed op de faseovergangen en de stabiliteit. Analyse van de veranderingen in de morfologie met TEM en Scanning Electron Microscopy (SEM) toont aan dat voor temperaturen tot 353 K, noch coalescentie noch korrelgroei optreedt. Dewetting begint bij 473 K wanneer agglomeratie optreedt, hetgeen resulteert in de vorming van bolvormige nanoporiën. De verschillen in de dichtheid en de vorm van de door gloeien veroorzaakte nanoporiën, weerspiegelen het verschil in film-substraat interactie. Voor Pd op Ti en Pd op PI, verdwijnen de microscheurtjes tijdens het gloeien en vormen grote bolvormige nanoporiën, die na PT weer verschijnen als brede microscheurtjes. Deze microscheurtjes wijzen op een effectief mechanisme voor lokale spanningsvermindering, waardoor de potentiële schade door hydridevorming wordt beperkt. Echter, door slechte adhesie van de Pd film op een kaal substraat, plant zich een scheur + knik netwerk voort, wat uiteindelijk leidt tot delaminatie van de film na HT + PT gloeien, zoals ook gevonden voor Pd films met compacte morfologie na hydridevorming op kamertemperatuur.

Om het vervormingsmechanisme te beschrijven in termen van defectparameters is een procedure ontwikkeld op basis van lijnverbredingsanalyse van XRD-profielen met behulp van de integrale breedte. De aangepaste Williamson-Hall plots geven aan dat in films met een open morfologie, de microrek wordt veroorzaakt door de aanwezigheid van dislocaties. Er wordt aangetoond dat na PT-only het toegenomen vrije oppervlak gegenereerd door microscheuren in de Pd film helpt om de dislocatiedichtheid te verminderen. De waargenomen toename in dislocatiedichtheid in de Pd film op Ti is te wijten aan de stijfheid van het substraat, waardoor dislocaties ophopen aan het film-substraat grensvlak. De Pd film op PI vertoont een kleine afname in dislocatiedichtheid en bijna geen microcracks, hetgeen suggereert dat een PI laag door zijn flexibiliteit enige relaxatie van rekken binnen de Pd kristallieten toelaat. Er treedt dus een microstructureel stabilisatiemechanisme op dat de Pd laag toelaat om uit te zetten en samen te trekken tijdens het laden en ontladen met waterstof, zodat enige spanningsrelaxatie optreedt langs open korrelgrenzen.

De hoofdstukken 4 en 5 van dit proefschrift zijn gewijd aan experimenten waarbij Pd dunne films met open morfologie (serie-2) 20 waterstof absorptie/desorptie cycli (20-L/D) ondergaan. Pd dunne films met identieke microstructuren (morfologie, spanningstoestand, en textuur) worden in deze hoofdstukken bestudeerd om de invloed van het type film-substraat grensvlak op de microstructurele veranderingen als functie van waterstofcycli te bepalen.

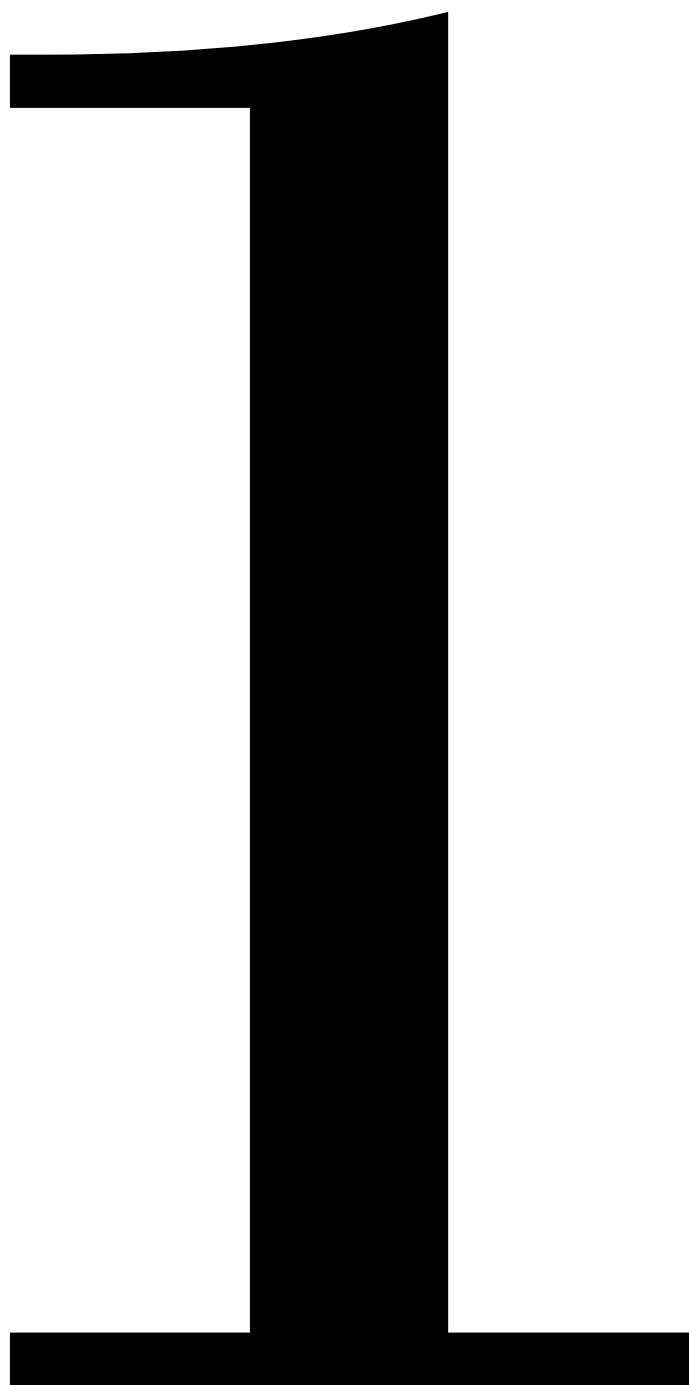
In hoofdstuk 4 wordt een methode ontwikkeld die een *in-situ* spanningsmeting tijdens hydridevorming mogelijk maakt in een XRD opstelling met focuserende geometrie. De meetprocedure maakt gebruik van een instrumentele kanteling (ω -kanteling) van het proefstuk waarbij ω de hoek tussen de invallende Röntgenbundel en het preparaatoppervlak is. De hoeken ω en 2θ liggen dus in hetzelfde vlak. Verschillende waterstof L/D experimenten worden uitgevoerd op dezelfde opstelling om de toepasbaarheid van de ω -kantelmethode voor betrouwbare *in-situ* spanningsresultaten te testen. Om de invloed van lage intensiteit, asymmetrie en slechte profielvorm van hoge-hoekreflecties verminderen, worden de piekposities bepaald met verschillende piekfit-methoden. Gebleken is dat een drempelintensiteit van 40% van de maximale intensiteit nodig is om overlappende gebieden tussen de pieken te vermijden. De methode is getest op open-morfologie Pd op kaal substraat en Pd op Ti tijdens 20-L/D cycli. De spanningsontwikkeling komt overeen met de *ex-situ* ψ -tilt spanning gemeten met parallelle bundel geometrie.

De ω -tilt spanningsmeettechniek wordt opnieuw gevalideerd in hoofdstuk 5 door 20-L/D cyclische testen uit te voeren op een *in-situ* opstelling in parallel-beam geometrie (ψ -tilt). Bovendien tonen de metingen met een preparaathouder met een transparante folie de afwezigheid van knikvorming tijdens waterstofbelasting (20 cycli) aan voor alle Pd dunne films. SEM-onderzoek toont microscheurgroei aan van een fijn webachtig netwerk tot verspreide brede scheuren die leiden tot knik-delaminatie (na 10 cycli) in Pd dunne film zonder adhesie laag, hetgeen de geleidelijke relaxatie van spanning door een evoluerende filmmorfologie bevestigt in systemen met een adhesielaag. Pd op Ti en Pd op PI vertonen een gestage uitbreiding van microscheurtjes maar blijven aan het substraat verbonden, zelfs na 20 cycli. Dit hoofdstuk presenteert ook een eenvoudige benadering om de spanning te bepalen in Pd dunne films die macroscopisch elastisch anisotroop zijn, door een combinatie van de kristallietgroep methode en de $\sin^2\psi$ -methode. De Pd dunne films, die in dit proefschrift bestudeerd zijn, hebben een vezeltextuur. Een stapsgewijze methode is ontwikkeld om de volumefracties van textuurcomponenten te berekenen uit een vezeltextuurplot, gedefinieerd als de dichtheid van polen die evenredig is met de integrale intensiteit van de diffractiepiek.

Deze methode wordt eerst toegepast op compacte films met een sterke vezeltextuur en op analoge wijze worden ook de volume fracties van de $\langle 111 \rangle$ kristallieten en de willekeurige georiënteerde kristallieten berekend voor open-morfologie films.

In overeenstemming met hoofdstuk 3, wordt geconcludeerd dat willekeurig georiënteerde pure schroefdislocaties van het $\{111\}$, $a/2\langle 110 \rangle$ slipsysteem de beste fit voor de gemodificeerde Williamson-Hall plots opleveren. De algemene trend laat een toename van de dislocatiedichtheid met toenemend aantal waterstofcycli voor Pd films op Ti zien, terwijl voor Pd op een kaal substraat en Pd op PI een geleidelijke afname wordt waargenomen. In Pd films op een kaal substraat heeft het knik-gedelamineerde gebied twee vrije oppervlakken die dislocaties toelaten te verdwijnen. In de Pd film op PI worden de dislocaties geannihileerd aan het kristallijn-amorfe grensvlak waarbij de PI laag als een perfect annihilatiepunt voor dislocaties fungeert. Bovendien toont de defectanalyse het omkeerbare proces van kristallietgrootte en dislocatiebeweging aan wanneer de spanningen wisselen tussen trek en druk tijdens waterstofcycli. Deze cyclische vervorming resulteert ook in een onomkeerbare textuurverandering, hetgeen een verscherping van de $\{111\}$ -vezel textuur inhoudt voor alle Pd dunne films met open morfologie.

De resultaten van deze hoofdstukken dragen bij tot het gebruik van Pd als materiaal voor toepassingen in verschillende waterstoftechnologieën.



Introduction

1.1. Background

The global energy consumption is estimated to nearly double by 2050 which prompts a sustainable energy vision of our future. Hydrogen (H_2) is a clean energy carrier [1] that is considered a potential long-term solution to the growing energy crisis and we must decisively overcome the many scientific and technological hurdles that exist between the present state of hydrogen production, separation, storage, transport, and utilization capabilities [2]. This will only be possible if primary requirements are satisfied to help to scale up the technology and to drive down costs. The most common hydrogen production methods, steam reforming of natural gas [3], coal and biomass gasification [4], and water electrolysis [5] yield hydrogen as a component in a gas mixture, syngas. Therefore, hydrogen should be separated from the gas mixture to obtain it in pure form. Currently, the most commonly used technologies for hydrogen purification are pressure swing adsorption [6], cryogenic distillation [7], and separation based on the use of membranes [8]. The latter is divided into two groups: porous and dense membranes. Among these, dense metallic membranes are particularly attractive due to their very high hydrogen selectivity and relatively high hydrogen permeability [9]. Palladium (Pd) is the most popular metal used in hydrogen separation membranes in this respect [10]. In the last decades, the role of palladium in virtually every aspect of the envisioned hydrogen economy has been investigated at both scientific and industrial levels [11-13].

This work focuses on the development and characterization of nanocrystalline Pd-based thin films prepared by sputter deposition to produce films with desired properties, thus enabling their application in hydrogen-based technologies. The properties are highly influenced by the microstructure (morphology and texture) of the films, including residual stress, which strongly affects the stability and performance of the film. Besides these mechanical issues, the investigated films offer great potential to develop improved diffraction analysis procedures, which are of scientific interest in thin film research. Some background information about the

palladium-hydrogen (Pd-H) system and nanocrystalline Pd-based thin films are given in the following sections.

1.2. The Pd-H system

First investigations of the hydrogen (H) absorption and diffusion through palladium (Pd) were carried out by Graham in 1866 [14]. Pd has been used since the 1920s in laboratories to obtain high-purity hydrogen, while palladium membrane technology received commercial attention in hydrogen purification in the late 1950s [15]. For the last few decades, the Pd-H system has been extensively studied as a prototypical hydrogen-storage material, and a model system for studies of hydrogen-metal interactions. Besides, Pd is also used as a catalyst for hydrogenation and dehydrogenation reactions. These studies are motivated by the fact that bulk Pd can absorb up to 900 times its volume of hydrogen gas at room temperature and atmospheric pressure, and its various alloys absorb comparable quantities [16, 17].

Pd has a face-centered cubic (fcc) structure with a lattice parameter of 3.890 Å [18, 19]. On absorption of hydrogen gas, H₂ molecules dissociate into atomic H on the surface of Pd; then the H atoms diffuse into bulk and occupy the octahedral interstitial sites of the fcc Pd lattice. The plots in Figure 1.1 show the absorption isotherms at different temperatures (also called pressure-composition isotherm or PCT curve) for the Pd-H system. At ambient conditions, the palladium hydride exists in two distinct fcc phases: solid solution α -PdH_x (dilute phase, H/Pd ratio $x < 0.015$) and metal hydride β -PdH_x (concentrated phase, $\beta_{\min} x > 0.58$). The occurrence of two coexisting phases between $0.02 < x < 0.6$ is located inside the domelike area of Figure 1.1. The width of this miscibility gap decreases with rising temperatures until a critical threshold $T_c = 300$ °C (bulk Pd) is reached. Above T_c , the miscibility gap is no longer observed.

In the dilute, α , phase the lattice constant increases by up to 0.1% compared to that of pure Pd metal (from 3.890 to 3.894 Å), while in the lower limit for the concentrated β_{\min} phase, the lattice constant changes up to 3.5% (from 3.894 to 4.025 Å), and at H/Pd ratio ≈ 0.7 (β_{\max}), the equilibrium value is 4.040 Å at 25 °C, 1 atm. The volume expansion from the α - to the β -phase is 10.4%. Upon desorption, the volume of the Pd is found to return to the initial value, but not the individual dimensions due to the lattice distortion around the H atoms. This expansion and contraction during $\alpha \leftrightarrow \beta$ transitions result in hydrogen embrittlement [20]. The embrittlement, together with the high cost of Pd, restricts the use of Pd and Pd-based

materials in industrial applications. Therefore, a large number of studies have focused on the residual effects of hydrogen absorption/desorption cycling on the mechanical properties of palladium and palladium-based materials.

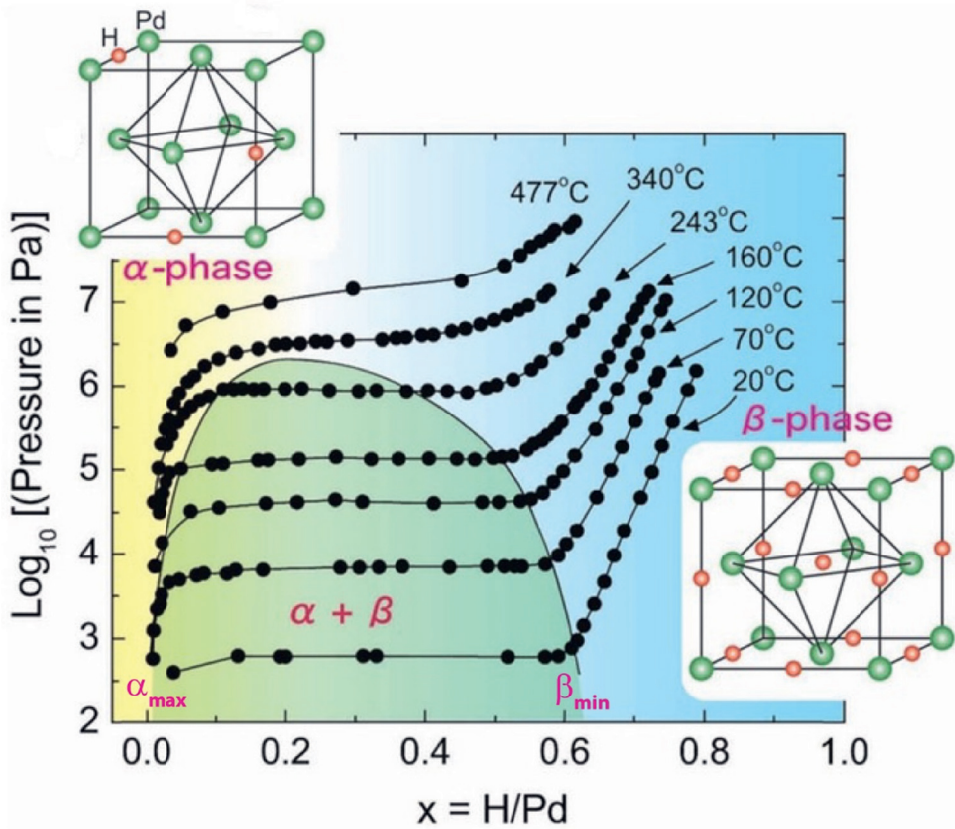


Figure 1.1. Pressure-Composition-Temperature (PCT) isotherms of the Pd-H system, including the regions corresponding to the two phases (α and β) and coexistence region ($\alpha + \beta$) of the system, and the schematic crystal structure of the α and β phases. H/Pd is the number of absorbed H atoms per Pd atom. Adapted from Ref. [21].

1.3. Pd-based nanocrystalline thin films

Pd-based metallic membranes are expensive and the flux through them is low, thus making them a less desirable material for upscaling at the commercial level. They can be improved if the metallic layer can be made thinner. However, a thinner layer has lower mechanical

strength in a self-supporting metal membrane application. In order to meet the challenge of attaining both high selectivity and good mechanical strength, Pd thin films are generated as ultrathin membranes by adhering the Pd layer to a substrate for support [22].

Different film deposition approaches and resulting microstructures are comprehensively discussed in Ohring's book [23]. Thin films (i.e., films having thicknesses from a few tens to a few hundreds of nanometers) are typically produced by physical vapor deposition (PVD). The PVD method used in the present thesis is magnetron sputtering: in the sputtering process, argon ions are created in plasma and accelerated into a target material, consisting of the pure metal from which impacting ions cause atoms to be removed (sputtered). These metal atoms propagate to the substrate and, upon deposition, build up the thin film. To increase the gas ionization, a magnetic ring is located behind the target to enhance the sputter rate by forcing the electrons on a cycloidal path. The deposition chamber maintains a base pressure lower than 1.3×10^{-5} Pa (1×10^{-7} Torr) in an ultra-high vacuum regime. The argon pressure, the substrate temperature, and the deposition rates are the main factors influencing the atom mobility on the surface of the substrate and therefore determine the developing microstructure of the thin film.

Although hydrogen absorption in Pd has been extensively studied since its discovery dating back to 1866, establishing a quantitative understanding of phase transformations and hydride formation in the nanoscale system is still in development [24-28]. Studies on the hydriding behavior of the Pd-H nanocrystalline systems have been also extended to nanoparticle systems [29]. The design and understanding of the role of nanostructuring as a powerful means to optimize material performance is an area of active research [30, 31]. In nanostructured materials, generally small crystallite sizes imply a high density of grain boundaries. The presence of multiple grain boundaries and interfaces gives favorable pathways for hydrogen diffusion and accelerates the kinetics of hydrogen absorption/desorption. For nanostructured palladium hydrides, there are drastic changes in the H_2 pressure-composition phase diagram [32]. The narrowing of the miscibility gap in the nano-PdH_x system relative to that in the bulk material has been reported [33]. The differences in hydriding behavior of nanocrystalline palladium have generally been attributed to the fact that a very large fraction of the hydrogen atoms is located quite close to grain boundaries. The narrowing of the miscibility gap is a surface effect associated with the grain size of the nanocrystalline palladium hydride [34].

The hydrogen solubility is also strongly affected by the morphology and microstructure of the film and the stress between regions of different hydrogen concentrations. For nanoscale systems, surface or interface-related sites become important and change the overall solubility as well the phase boundaries of the Pd-H system. Pd thin films deposited on various substrates revealed that the crystal structure of the substrate has a relatively low impact on the behavior of the film loaded with hydrogen [35, 36]. The dominating factor affecting the behavior of hydrogen-loaded film is the strength of binding between the film and the substrate. The present work will show that the microstructure-substrate relationship of Pd thin films is of crucial importance in enabling tuning and optimization of their performance. The effect of film-substrate clamping on hydrogen absorption and desorption in Pd thin films is addressed at room temperature and after annealing. The X-ray diffraction (XRD) technique is the main tool used for experimental investigation in the present work. Different in-situ XRD set-ups are used for hydrogen loading and deloading, besides characterization of crystal structures, phase contents, strain, crystallographic textures, and microstructural features of Pd thin films.

Pd thin films are widely used in hydrogen technology due to the catalytic effect of the thin Pd layer on the hydrogenation of a variety of materials. Pd films are used also as the gate electrodes of metal-oxide-semiconductor hydrogen sensors. Pd thin films as reliable sensors, capable of measuring H_2 over a wide range of concentrations (from 10^{-8} to 10^{-2}) under different environmental conditions, are developed that can fulfil the needs of the hydrogen industry. Currently, there is enough evidence from the literature and research findings to support the viability and enormous benefits of Pd thin films to be used in fuel cells that can power attributes that require electricity like cars, trucks, busses, household appliances, laptops, and mobile phones. Therefore, the relationship between preparation methods and mechanical stability of pure Pd thin films, as well as other issues affecting high-temperature performance, have to be thoroughly investigated, which is the objective of the present thesis.

1.4. Scope and outline of the thesis

This thesis is dedicated to the development and characterization of nanocrystalline Pd thin films as demonstrated in the chapters 2–5. Based on the available literature on the Pd thin films [37, 38] for various hydrogen-related energy applications, Pd thin films are grown by magnetron sputtering in the present research, enabling a detailed investigation of morphology,

microstructure, mechanical and thermal stability, and performance during hydrogen cycling of the studied Pd thin films.

Chapter 2 deals with the Atomic Force Microscopy (AFM) investigation of the surface topography of Ti layers sputter-deposited with different deposition pressures and thicknesses. Further, the influence of the Ti adhesive intermediate layer on the Pd thin film hydriding kinetics is evaluated by analyzing the growth microstructure of the sputter-deposited Pd layer in terms of morphology and crystallographic texture. The *in-situ* XRD hydriding experiments are interpreted by fitting various analytical rate equations to establish the rate-determining reaction mechanism and kinetic parameters during hydrogen absorption.

Chapter 3 presents a comprehensive *in-situ* XRD experimental study to demonstrate the dependence of the film microstructure and the film-substrate interaction on the mechanical stability of Pd thin films exposed to hydrogen. A custom-made sample holder is implemented for visual observation of the topographical changes on Pd thin films during phase transformations at room temperature. For detection of hydrogen-induced transformations above room temperature, several loading/deloading conditions are investigated. It is shown that annealing significantly impacts the performance and stability of Pd thin films. These findings are further supported by the observation that stress relaxation mechanisms are different for Pd films with a comparable microstructure, but deposited with different adhesive intermediate layers on a stiff substrate.

Chapter 4 develops a measurement procedure that involves applying instrumental virtual tilt (ω -tilt) to the sample about the diffraction axis during 20 hydrogen loading and deloading cycles on an XRD set-up with focusing geometry. Various (repeated) hydrogen loading and deloading experiments on a similar XRD set-up are performed to test the applicability of the ω -tilt method for reliable *in-situ* stress results.

Chapter 5 involves a systematic study of the morphology, grain-orientation distribution (texture), state of stress, and dislocation density evolution during 20 hydrogen loading and deloading cycles at room temperature in Pd thin films sputtered on substrates of different compliances. A methodological sequence to estimate texture volume fractions for thin films with weak fiber texture is described along with a dedicated stress-analysis method combining the $\sin^2\psi$ method and the crystallite group method. Microstructural evolution during the cyclic process is used as a measure to determine the deformation behavior.

1.5. References

- [1] Abe J, Popoola A, Ajenifuja E, Popoola O. Hydrogen energy, economy and storage: review and recommendation. *Int J Hydrogen Energ.* 2019;44:15072-86.
- [2] Dawood F, Anda M, Shafiullah G. Hydrogen production for energy: An overview. *Int J Hydrogen Energ.* 2020;45:3847-69.
- [3] Chen J, Yan L, Song W, Xu D. Methane steam reforming thermally coupled with catalytic combustion in catalytic microreactors for hydrogen production. *Int J Hydrogen Energ.* 2017;42:664-80.
- [4] Sikarwar VS, Zhao M, Clough P, Yao J, Zhong X, Memon MZ, et al. An overview of advances in biomass gasification. *Energy & Environmental Science.* 2016;9:2939-77.
- [5] Wang M, Wang Z, Gong X, Guo Z. The intensification technologies to water electrolysis for hydrogen production—A review. *Renewable and sustainable energy reviews.* 2014;29:573-88.
- [6] Relvas F, Whitley RD, Silva C, Mendes AI. Single-stage pressure swing adsorption for producing fuel cell grade hydrogen. *Ind Eng Chem Res.* 2018;57:5106-18.
- [7] Aasadnia M, Mehrpooya M, Ghorbani B. A novel integrated structure for hydrogen purification using the cryogenic method. *Journal of Cleaner Production.* 2021;278:123872.
- [8] Adhikari S, Fernando S. Hydrogen membrane separation techniques. *Ind Eng Chem Res.* 2006;45:875-81.
- [9] Ockwig NW, Nenoff TM. Membranes for hydrogen separation. *Chemical reviews.* 2007;107:4078-110.
- [10] Al-Mufachi N, Rees N, Steinberger-Wilkens R. Hydrogen selective membranes: a review of palladium-based dense metal membranes. *Renewable and Sustainable Energy Reviews.* 2015;47:540-51.
- [11] Adams BD, Chen A. The role of palladium in a hydrogen economy. *Materials today.* 2011;14:282-9.
- [12] Konda SK, Chen A. Palladium based nanomaterials for enhanced hydrogen spillover and storage. *Materials Today.* 2016;19:100-8.
- [13] Sousanis A, Biskos G. Thin Film and Nanostructured Pd-Based Materials for Optical H₂ Sensors: A Review. *Nanomaterials.* 2021;11:3100.
- [14] Graham T. On the absorption and dialytic separation of gases by colloid septa. *Philos Trans R Soc, London.* 1866;156:399-439.
- [15] Juenker D, Van Swaay M, Birchenall C. On the use of palladium diffusion membranes for the purification of hydrogen. *Rev Sci Instrum.* 1955;26:888-.
- [16] Li J, Fan R, Hu H, Yao C. Hydrogen sensing performance of silica microfiber elaborated with Pd nanoparticles. *Mater Lett.* 2018;212:211-3.
- [17] Barton J, Lewis F, Woodward I. Hysteresis of the relationships between electrical resistance and the hydrogen content of palladium. *Transactions of the Faraday Society.* 1963;59:1201-7.
- [18] Flanagan TB, Oates W. The palladium-hydrogen system. *Annual Review of Materials Science.* 1991;21:269-304.
- [19] Manchester F, San-Martin A, Pitre J. The H-Pd (hydrogen-palladium) system. *Journal of phase equilibria.* 1994;15:62-83.
- [20] Paglieri S, Way J. Innovations in palladium membrane research. *Separation & Purification Reviews.* 2002;31:1-169.
- [21] Akiba H, Kobayashi H, Kitagawa H, Kofu M, Yamamuro O. Glass transition and positional ordering of hydrogen in bulk and nanocrystalline palladium. *Physical Review B.* 2015;92:064202.

- [22] Vlček M, Lukáč F, Vlach M, Procházka I, Wagner S, Uchida H, et al. Hydrogen-Induced Buckling of Pd Films Deposited on Various Substrates. *Defect and Diffusion Forum*. 2015;365:55-62.
- [23] Ohring M. *Materials science of thin films*: Academic press; 2001.
- [24] PunDT A. Hydrogen in Nano-sized Metals. *Advanced Engineering Materials*. 2004;6:11-21.
- [25] Yamauchi M, Ikeda R, Kitagawa H, Takata M. Nanosize effects on hydrogen storage in palladium. *The Journal of Physical Chemistry C*. 2008;112:3294-9.
- [26] Bardhan R, Hedges LO, Pint CL, Javey A, Whitlam S, Urban JJ. Uncovering the intrinsic size dependence of hydriding phase transformations in nanocrystals. *Nature materials*. 2013;12:905-12.
- [27] Baldi A, Narayan TC, Koh AL, Dionne JA. In situ detection of hydrogen-induced phase transitions in individual palladium nanocrystals. *Nature materials*. 2014;13.
- [28] Griessen R, Strohhfeldt N, Griessen H. Thermodynamics of the hybrid interaction of hydrogen with palladium nanoparticles. *Nature materials*. 2016;15:311-7.
- [29] Ulvestad A, Yau A. The self-healing of defects induced by the hydriding phase transformation in palladium nanoparticles. *Nature communications*. 2017;8:1-6.
- [30] Syrenova S, Wadell C, Nugroho FA, Gschneidtnr TA, Fernandez YAD, Nalin G, et al. Hydride formation thermodynamics and hysteresis in individual Pd nanocrystals with different size and shape. *Nature materials*. 2015;14:1236-44.
- [31] Narayan TC, Hayee F, Baldi A, Koh AL, Sinclair R, Dionne JA. Direct visualization of hydrogen absorption dynamics in individual palladium nanoparticles. *Nature communications*. 2017;8:14020.
- [32] Narehood D, Kishore S, Goto H, Adair J, Nelson J, Gutierrez H, et al. X-ray diffraction and H-storage in ultra-small palladium particles. *Int J Hydrogen Energ*. 2009;34:952-60.
- [33] Eastman J, Thompson L, Kestel B. Narrowing of the palladium-hydrogen miscibility gap in nanocrystalline palladium. *Physical Review B*. 1993;48:84.
- [34] Wolf RJ, Lee MW, Ray JR. Pressure-composition isotherms for nanocrystalline palladium hydride. *Physical review letters*. 1994;73:557.
- [35] Pivak Y, Schreuders H, Slaman M, Griessen R, Dam B. Thermodynamics, stress release and hysteresis behavior in highly adhesive Pd-H films. *Int J Hydrogen Energ*. 2011;36:4056-67.
- [36] Čížek J, Melikhova O, Vlček M, Lukáč F, Vlach M, Procházka I, et al. Hydrogen-induced microstructural changes of Pd films. *Int J Hydrogen Energ*. 2013;38:12115-25.
- [37] Amin-Ahmadi B, Connétable D, Fivel M, Tanguy D, Delmelle R, Turner S, et al. Dislocation/hydrogen interaction mechanisms in hydrided nanocrystalline palladium films. *Acta Materialia*. 2016;111:253-61.
- [38] Wagner S, Kramer T, Uchida H, Dobron P, Cizek J, PunDT A. Mechanical stress and stress release channels in 10–350 nm palladium hydrogen thin films with different microstructures. *Acta Materialia*. 2016;114:116-25.

2

Controlling morphology and texture of sputter-deposited Pd films by tuning the surface topography of the (Ti) adhesive layer¹

In this chapter, the effect of the deposition parameters of a magnetron sputtered Ti adhesive intermediate layer on the morphology and hydrogen absorption properties of Pd thin films of about 100 nm is investigated. The insertion of an adhesive layer between a Pd film and a rigid substrate usually suppresses or reduces hydrogen absorption. In this study, it is shown that by tuning the surface topography of the intermediate layer the morphology, crystallographic texture and hydrogen absorption properties of the Pd film can be controlled. The surface topography of the Ti layer was characterized using Atomic Force Microscopy. The surface topography strongly depends on the Ti deposition conditions and can vary from widely spread large islands to densely packed small-grained islands depending on thickness (between 1 and 6 nm) and sputter pressure (0.4 and 3 Pa). TEM and XRD analysis led to the conclusion that rough Ti intermediate layers result in Pd films with an open columnar structure with small voids, and a weak and broad {111} texture. Smooth Ti intermediate layers promote the formation of Pd films with a dense columnar structure with fewer voids, and a strong and sharp {111} texture. Changes in the Pd adatom surface diffusion and shadowing effects are the main cause of the observed differences. Pd films with an open columnar morphology and weaker texture show better hydrogen absorption properties with respect to absorption capacity and kinetics of the films with dense columnar morphology. By tuning the surface topography of the Ti adhesive layer, Pd films with controlled morphology and texture can be prepared such that no delamination from the substrate occurs, without compromising on absorption properties.

¹ This chapter has been published as:

N. Verma, G. Krishnamurthy, F.D. Tichelaar, A.J. Böttger, *Controlling morphology and texture of sputter-deposited Pd films by tuning the surface topography of the (Ti) adhesive layer*, Surface and Coatings Technology, vol. 359, pp. 24-34, 2019.

2.1. Introduction

The production of hydrogen from fossil fuels by water-gas shift (WGS) reaction can be energy efficiently achieved by means of membrane reactors [1, 2]. So far, a wide scale application is hindered by the limited lifetime of the membrane material and the related costs of downtime and replacement [3]. Paglieri and Way [1] highlighted various aspects of palladium membrane research and described Pd-based membrane material as the most promising because of the high hydrogen selectivity, relatively high hydrogen permeability, and usability in the temperature range of 200 °C to 600 °C [2]. Nevertheless, there are some limitations. Pure palladium undergoes a phase transformation ($\alpha \leftrightarrow \beta$) below the critical temperature (293 °C) in the presence of hydrogen [4]. This transition to β -hydride is accompanied by a large volume expansion of about 10%, resulting in plastic deformation and hydrogen embrittlement. Alloying palladium with for instance iron, nickel, copper, silver, etc. effectively lowers the critical temperature [5, 6] to below the WGS process conditions. Alloying affects other properties too, i.e. hydrogen permeability, surface segregation [7], the catalytic performance, and mechanical behaviour. In order to be mechanically and thermally stable in hydrogen atmosphere, self-supporting metal foils with a thickness of 25-100 μm are required [8, 9]. Li *et al.* [10] reviewed both the experimental and modelling studies done over decades on Pd-based membranes and concluded that conventional Pd metal tubes used in the field of ultra-pure hydrogen generation (99.999%) are expensive with relatively low permeance, and thus limited to small-scale applications. Therefore, research is going on worldwide to develop cost-effective materials to replace high-cost Pd-based membrane material [11].

One way to improve Pd-based membrane material is by using thin films of the order of several hundreds of nm and by nano-structuring [12, 13]. Under appropriate conditions, nano-crystalline Pd thin films have a hydrogen diffusivity of up to ten times greater than in polycrystalline Pd [14]. A thinner metal film, however, has lower mechanical strength and needs to be clamped on a substrate for support [10]. Very thin and nanostructured Pd films also are used as hydrogen sensor and commercialized in connection with the expanded use of hydrogen gas as an energy source [15]. Such films often suffer critical drawbacks in terms of structural deformation; hydrogen induced lattice expansion of Pd and delamination being the most common ones. Strong adhesion of Pd to the substrate hampers in-plane relaxation of mechanical stresses [16, 17] leading to reduced hydrogen absorption and sensing in thin film

sensors [18]. Alternatively, poor adhesion of the film causes severe stability problems related to crack formation and delamination [1, 2, 4] leading to a loss of selectivity.

Thin Pd films on various substrates showed partial transformation to hydride, buckling, and deformation after β -phase formation even at room temperature [19, 20]. In a previous study [21], we showed that Pd thin films on an oxidized silicon substrate, with an open columnar structure, could stabilize against embrittlement but delamination occurs when exposed to multiple $\alpha \leftrightarrow \beta$ transformation cycles. The delamination problem could be solved by adding adhesive intermediate layers between the Pd film and substrate [22]. Ti as an adhesive layer has proven to suppress the structural deformation in Pd film [18] mainly because the volume expansion of the Pd film is restricted and therefore the solubility of hydrogen is partly suppressed. To prevent changes in performance (permeability), the adhesion layer should be engineered such that the Pd film with desired performance and microstructure can be attained. The work in this chapter is intended to enhance long-term stability of the unalloyed Pd thin films without compromising its permeability by the suppression of hydrogen absorption.

It is essential to understand the influence of process parameters on the nano-/micro-structural characteristics of Pd thin films to further enhance their properties in applications. While so much work has been devoted to understanding the effect of deposition parameters on the morphology and structure of thin films [23-25], there have been fewer efforts to understand the influence of the underlying surface conditions of the substrate or an intermediate layer on the morphology of the Pd film. The surface topography of an adhesive intermediate layer could vary. For instance, the structure of a Ti layer could change from amorphous to crystalline depending on process conditions applied during DC magnetron sputtering [26]. Chawla *et al.* [27] reported Ti films of the surface topography of various surface roughness depending on sputtering conditions. Atomic Force Microscopy (AFM) analysis of the Ti films in their work revealed an increasing trend in surface roughness with sputtering pressure. The surface roughness then could influence the final morphology of the layer deposited on top of it [28, 29].

In the current work, the role of process parameters such as deposition pressure, deposition time and layer thickness on the surface topography of Ti layers are studied. A systematic investigation of the influence of Ti intermediate layer on growth morphology and absorption performance of Pd films was carried out. The following set of samples are used: Pd film without an adhesive layer (Pd-SiO₂/Si) and Pd with adhesive Ti layer (Pd-Ti-SiO₂/Si) deposited on an oxidized Si substrate (SiO₂/Si). Direct observation of the nanometric surface

topography of the Ti layer has been performed and analysed by means of AFM. The hydrogen absorption performance is assessed, by following the transformation to β -hydride by means of *in-situ* X-ray diffraction (XRD). The obtained absorption kinetics curves are used to determine the reaction mechanism of the hydrogen absorption process in Pd thin films.

2.2. Materials and methods

2.2.1. Thin film sputter deposition

Pd films with and without Ti intermediate layer (Pd and Pd on Ti layer) were deposited on thermally oxidized Si wafer (SiO_2/Si) substrate by DC magnetron sputtering (ATC 1500F AJA International). The sputter chamber was held under high vacuum (1×10^{-5} Pa base pressure) before performing the deposition. The target-to-substrate distance was maintained at 11 cm and the substrate stage was rotating at a rate of 20 rpm during all depositions. Pure Argon was used as sputtering gas. All Pd thin films of about 100 nm thickness were prepared by performing deposition for 900 s (rate 0.1 nm/s) with 100 W DC power at 3 Pa Ar pressure. A series of Ti layers with a range of thicknesses at two Ar pressures (0.4 Pa and 3 Pa) were sputter deposited on bare Si wafer (Si) and SiO_2/Si substrates. The deposition rate for Ti was calibrated by sputtering for 1 hr resulting in a thickness of ~ 280 nm at 0.4 Pa (0.077 nm/s) and ~ 60 nm at 3 Pa (0.016 nm/s). Ti layer thicknesses of 1, 3 and 6 nm were aimed by varying the deposition time accordingly (Table 3.1). Ti and Pd metal targets (50 mm dia.) used for deposition are with 99.999% purity from AJA international. Thermally oxidized Si wafer (diameter: 50.8 ± 0.3 mm, doping: B, orientation: {100}, oxide layer of ~ 188 nm, single flat, prime, single side polish) from SPS EUROPE-BV were used as received. Before deposition as received Si and SiO_2/Si wafers and metal targets were sputter cleaned to etch away any dirt present.

2.2.2. Scanning Transmission Electron Microscopy (STEM)

A Tecnai F20UT/STEM (200 kV) was used for imaging – Bright Field (BF), Dark Field (DF), and lattice imaging mode. Compositional analysis of the film-intermediate-substrate interface was done in STEM mode by elemental mapping on a cross-section using a FEI Cs-corrected cubed titan (300 kV), equipped with an Oxford Instruments X-Max^N 100TLE energy-dispersive X-ray (EDX) detector. The spatial resolution of the elemental maps is 1-2 nm.

Annular Dark Field (ADF) images were also obtained during elemental mapping. The samples were prepared by Argon ion milling from a cross-sectional cut protected by a glass plate glued on the film. The images of the film cross-sections were obtained with the film-substrate interface parallel to the electron beam.

2.2.3. Atomic Force Microscopy (AFM)

The surface characterizations of the Ti layers were performed in air and at room temperature with AFM (NT-MDT, Ntegra) operated in the tapping mode, with a Si tip cantilever of radius 10 nm nominal curvature and a resonance frequency of 296-358 kHz. The surface roughness was measured by a raster scan method over a small area of $1 \times 1 \mu\text{m}^2$, $3 \times 3 \mu\text{m}^2$ and $10 \times 10 \mu\text{m}^2$ of the sample. The resulting data were analysed using Gwyddion – Version 2.47 for calculating roughness parameters and generating line scans. The surface profile parameters include average roughness (R_a) and root mean square roughness (R_q), and line profile parameters include roughness mean spacing (S_m), skewness (R_{sk}), and kurtosis (R_{ku}) as summarized by De Oliveria *et al.* [30].

2.2.4. X-Ray Diffraction (XRD)

2.2.4.1. Ti layer thickness

The thickness of Ti layers was determined by means of X-Ray Reflectometry (XRR) measurements performed on Bruker-AXS D5005 diffractometer using $\text{CuK}\alpha$ radiation with X-ray tube operating at 45 kV, 30 mA. Reflectivity scans were obtained for the 2θ range 0.2° to 5.0° with 0.02° step size using 0.2 mm fixed slits. Thickness was determined using X'Pert Reflectivity PANalytical software.

2.2.4.2. Pd thin film texture

A Bruker-AXS D8 Discover diffractometer equipped with polycapillary optics (0.25°) and Eulerian cradle was used for texture measurement of the as-deposited films Pd and Pd on Ti layers. The size of the incident beam was adjusted according to the specimen dimension by the use of cross slit placed in front of a sealed X-ray tube ($\text{CoK}\alpha$; 45 kV, 25 mA). The diffracted beam passed a parallel soller slit of 0.35° and a graphite monochromator before

reaching the detector. Information regarding the overall preferred orientation (texture) of the crystallite relative to the film substrate was obtained using the Schulz reflection method [31].

Characterization of the fiber texture was based on the integrated intensities of the full Bragg peaks from θ - 2θ scans, including peak tails and background [32]. Data were obtained for the (hkl) reflection of the interest by Ψ -tilting the sample from 0° to 75° in steps of 5° at a fixed rotation angle φ . Diffraction patterns were evaluated by peak fitting (Bruker - EVA software). For each diffraction peak, a linear background was fitted. Measured intensities were corrected for absorption and instrumental intensity loss. Data were presented as fiber texture plot (FTP) which is peak area integrated intensity vs tilt angle Ψ .

2.2.4.3. *In-situ* XRD hydrogen absorption

Hydrogen loading/deloading cycles were performed in an *in-situ* XRD set-up: Bruker-AXS D5005 diffractometer in the Bragg-Brentano focusing geometry ($\text{CuK}\alpha$; 45 kV, 30 mA), equipped with MRI HT chamber. The chamber was connected with mass flow controller for N_2 gas and H_2/N_2 gas mixture. Hydrogen cycling was carried out in 5% H_2 and 95% N_2 gas mixture ($p_{\text{H}_2} = 5$ kPa) and N_2 (101.3 kPa) gas respectively. The measurements were performed at room temperature and atmospheric pressure. The $\alpha \leftrightarrow \beta$ Pd-phase transformations were monitored by collecting diffraction patterns of the $\{111\}$ -reflections every 2 min in 2θ range 37° to 42° .

The integrated intensities were determined using a pseudo-Voigt function fit. Correction was made for the small effect of scattering factor and Lorentz polarization factor [33] to obtain values proportional to the diffracting volume, V .

The β -phase volume fraction, $v\beta(t)$, was evaluated as a function of time and converted to the number of hydrogen atoms absorbed per atom of metal, H/Pd, to obtain an absorption curve. To estimate the H content based on the relative amounts of α - and β -Pd phase, we assumed that the α -phase contains no hydrogen and the β -phase has a H/Pd ratio of ~ 0.64 at room temperature [4]. Assuming that the transformed (reacted) fraction corresponds to the β -phase volume fraction, we estimated the amount of hydrogen, $c(t)$, in the material in terms of hydrogen concentration H/Pd: $c(t) = v\beta(t) * 0.64$

2.2.4.4. Kinetic equation

To study the kinetics various analytical rate expressions were fit to the time-dependent reacted fraction (ξ), through which reaction mechanism and kinetic parameters can be determined. The rate equation for the kinetics of solid-gas reactions is generally expressed Eq. (2.1) [34]:

$$d\xi/dt = k f(\xi) \quad (2.1)$$

where ξ is the reacted fraction at time t ; k is the rate constant, and $f(\xi)$ is a function describing the reaction mechanism. The integral form of $f(\xi)$ is $g(\xi)$ given by:

$$g(\xi) = \int d\xi / f(\xi) = kt \quad (2.2)$$

The functions $f(\xi)$ or $g(\xi)$ represent the reaction mechanism involved like a chemical reaction, diffusion, nucleation and nuclei growth. Based on the experimental data for hydrogen absorption starting from the α -phase, the reacted fraction ξ was calculated as:

$$\xi = v\beta_t / v\beta_{eq} \quad (2.3)$$

where $v\beta_t$ is β -phase volume fraction at time t ($v\beta_{t=0}=0$) and $v\beta_{eq}$ is β -phase volume fraction at equilibrium. The fraction $v\beta_{eq}$ corresponds to the maximum capacity of the material to absorb hydrogen (H/Pd_{max}). The data of t , ξ , and $(d\xi/dt)$ obtained from ξ - t curves were regressed linearly based on the integral from Eq. (2.2). Kumar *et al.* [35] present the detail procedure for investigating the absorption kinetics behaviour and reaction mechanism using solid-state kinetic models. The reacted fraction curves were fitted by the model equations listed by Khawam and Flanagan [34] and the fitting equations with the largest correlation coefficient (R^2) are considered rate determining reaction mechanisms to describe the hydrogen absorption process of Pd thin films [36].

2.3. Results and discussion

The approximate thicknesses of the Ti layer are listed in Table 2.1 as determined by XRR. The aimed Ti thickness of 1 nm at 0.4 Pa Ar pressure was not achieved, primarily because the deposition time was increased to 20 s in order to avoid the un-deposited area on the substrate. All the investigated films Pd and Pd on Ti layers were deposited with the same Pd deposition conditions, *i.e.*, at room temperature and using 3 Pa Ar pressure.

Table 2.1 – Approximate Ti layer thickness obtained by XRR for different sputter times at 0.4 Pa and 3 Pa Ar pressures, on bare Si wafer (Si) and oxidized Si wafer (SiO₂/Si) substrates. Next, to the sputter times used, the envisioned thickness is given between brackets.

Sputter time (s)	0.4 Pa		Sputter time (s)	3 Pa	
	Ti layer thickness (nm)			Ti layer thickness (nm)	
	Si	SiO ₂ /Si		Si	SiO ₂ /Si
20 (1 nm)	3.0	3.0	60 (1 nm)	0.6	1.0
38 (3 nm)	4.4	4.3	180 (3 nm)	4.0	3.8
70 (6 nm)	5.8	6.0	360 (6 nm)	6.5	6.4

2.3.1. Atomic Force Microscopy

2.3.1.1. Ti layer surface topography

To understand the effect of underlying surface conditions on the Pd film growth microstructure, AFM was used to investigate the surface topography of Ti layers and bare substrates. Figure 2.1 presents AFM images along with roughness parameters of SiO₂/Si substrate and representative Ti layers with a thickness of about 1 nm deposited at 3 Pa on Si and SiO₂/Si substrates. Bare silicon (Si) substrate displayed a smooth surface morphology compared to that of oxidized Si substrate (SiO₂/Si). Its RMS roughness could not be measured because the roughness was below the detection limit of the available AFM instrument. For the SiO₂/Si substrate, the presence of the oxide layer of 188 ± 2 nm increased the RMS roughness to 0.25 ± 0.02 nm. When Ti is deposited directly on a Si substrate, the surface roughness is higher than for Ti on a SiO₂/Si substrate, as clearly visible in the 3D AFM images in Figures 2.1(a&c).

The higher roughness of a Ti layer on a Si substrate can be understood in terms of the strong binding of Ti atoms to defects sites on the Si surface [37]. These sites serve as a nucleation site for island-type growth mode. By surface diffusion, large Ti islands grow according to a Stranski-Krastanov mechanism [38]. These islands are visible in the 2D AFM image shown in Figure 2.1(a), as the large white/lighter areas; the dark areas correspond to un-covered Si substrate. The negative Skewness also indicates a ridged surface with deep valleys between Ti islands; the resulting surface roughness is 0.52 ± 0.09 nm.

On SiO_2/Si surface a reaction of Ti and SiO_2 occurs even at room temperature [39]. This results in a very good bond between Ti and the SiO_2 layer [40] without the formation of Ti silicide, for deposition temperatures below 500 °C [41]. The resulting limited diffusion of Ti adatoms leads to a uniform spreading of the deposited Ti on the substrate surface Figure 2.1(c). Wallert *et al.* [41] suggested that Ti oxidation at Ti- SiO_2 interface is limited until deposition thickness of about 1 nm, further Ti deposition leads to the progressive formation of a pure Ti layer. Because Ti serves as a good adhesion layer between the Pd film and the oxidized Si substrate, for further analysis SiO_2/Si substrates were used.

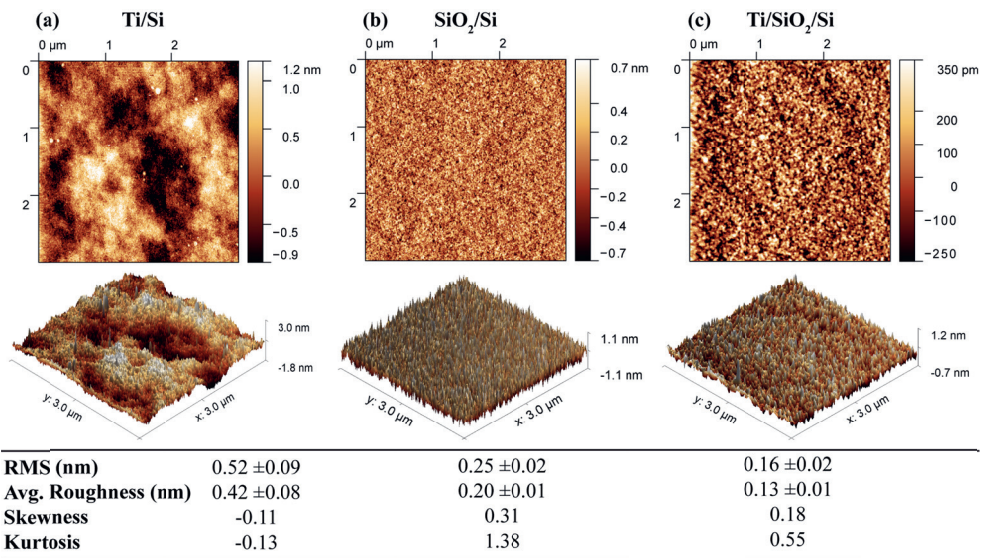


Figure 2.1 – AFM topography images of (a) 1 nm Ti deposited at 3 Pa on bare Si wafer (Ti-Si), (b) oxidized Si wafer (SiO_2/Si), and (c) 1 nm Ti deposited at 3 Pa on oxidized Si wafer (Ti- SiO_2/Si). The scanned area is $3 \mu\text{m} \times 3 \mu\text{m}$.

Figure 2.2 presents 2D and 3D AFM images along with the accompanying line profiles of Ti layers on a SiO_2/Si substrate. Figures 2.2(a-b) and (c-d) shows the influence of thickness on Ti layer surface morphology at deposition pressures of 0.4 Pa and 3 Pa, respectively. From the AFM images of the thinnest Ti layers in Figures 2.2(a&c) it is readily observed that there is a difference in the initial island formation at Ar pressures 0.4 Pa and 3 Pa. The line profiles, in Figures 2.2(a&c) illustrates that the formation of closely packed small islands occurred at 0.4 Pa, while, at 3 Pa widely spaced large islands are formed. The Ti coverage over the substrate

is relatively large for 6 nm thickness (Figures 2.2(b&d)) as compared to the ones with a thickness of 1 nm and 3 nm. This full coverage at 6 nm is due to the lateral growth of the initial small islands resulting in the formation of a continuous Ti layer (Figure 2.3 discussed in STEM section). Thicker Ti layers in Figures 2.2(b&d) show that a layer sputtered at 0.4 Pa exhibits fine granular morphology, while a layer sputtered at 3 Pa consists of patches separated by uncovered substrate areas. In order to complete the above discussion, we looked at other roughness parameters.

Table 2.2 – *Roughness parameters of Ti layers deposited on SiO₂/Si substrate from AFM image of 3 μ m x 3 μ m scan size area.*

	Ti layer deposition pressure (Pa)	Ti layer Thickness (nm)	R_q (nm)	R_a (nm)	S_m (nm)	R_q/R_a	R_{sk}	R_{ku}
SiO ₂ /Si			0.25	0.20	70	1.25	0.31	1.40
Ti-SiO ₂ /Si	0.4	3.0	0.24	0.20	55	1.20	0.06	0.03
		4.3	0.25	0.20	60	1.25	0.15	0.11
		6.0	0.26	0.21	90	1.24	0.10	0.09
	3.0	1.0	0.17	0.13	130	1.31	0.18	0.56
		3.8	0.21	0.16	110	1.31	0.12	0.33
		6.4	0.26	0.21	85	1.24	0.44	0.90

Table 2.2 illustrates that the variations in the average roughness (R_a) have the same trend as the variation in RMS roughness (R_q) values. The RMS roughness is nearly the same for all Ti layer thickness sputtered at 0.4 Pa, while RMS increases with increasing Ti thickness for layers sputtered at 3 Pa. The positive values of the skewness (R_{sk}) indicate that spikes are dominant over the scanned surface. The $R_{ku} < 3$ highlights the uneven distribution of Ti islands over the scanned area resulting in a bumpy surface. The spacing between Ti islands and the island size can be evaluated from the mean spacing parameter (S_m). The combination of low RMS surface roughness and large mean spacing of about 130 nm for 1 nm Ti layer (at 3 Pa) indicates the formation of widely spaced Ti islands as seen from the large white spots shown in Figure 2.2(c).

Differences in sputter pressure mainly cause the differences in morphology. For Ti layers deposited at high Ar pressure of 3 Pa (see Figures 2.2(c&d)), the increase in gas pressure favours an excess number of argon gas species with shorter mean-free-path [42]. Thus, Ti atoms undergo more collisions reducing their surface mobility on the substrate leading to widely spaced islands. A high Ar pressure also limits the average angle of incidence causing self-shadowing and island structures with widely spaced valleys [25]. The widely spread spiky island formation is reflected in the surface parameters in Table 2.2 (i.e., high R_{Ku} , positive skewness).

For Ti layer deposited at low Ar pressure of 0.4 Pa, the higher mobility of the sputtered Ti atoms resulted in the formation of smaller Ti islands leading to smoother surfaces as shown in Figures 2.2(a&c). The formation of the smaller Ti islands is reflected by the lower mean spacing (S_m) values at 0.4 Pa Ar pressure in Table 3.2, than for Ti layer deposited at 3 Pa. The nearly zero skewness value of 3 nm Ti layer deposited at 0.4 Pa indicates equally dominant peaks and valleys for the top surface profile (also demonstrated by 3D AFM images in Figures 2.2(a&b)).

For both Ar pressures, an increase in Ti layer thickness resulted in the formation of a continuous Ti layer by island coalescence [43, 44]. Ti layers deposited at 3 Pa have a rougher surface; the initial large and well-separated islands enhance the shadowing effect thereby promoting the formation of hillocks. The large difference in surface topography between the 1 and 6 nm Ti deposited at 3 Pa sputter pressure could be due to a difference in Ti structure as observed by STEM discussed in next section.

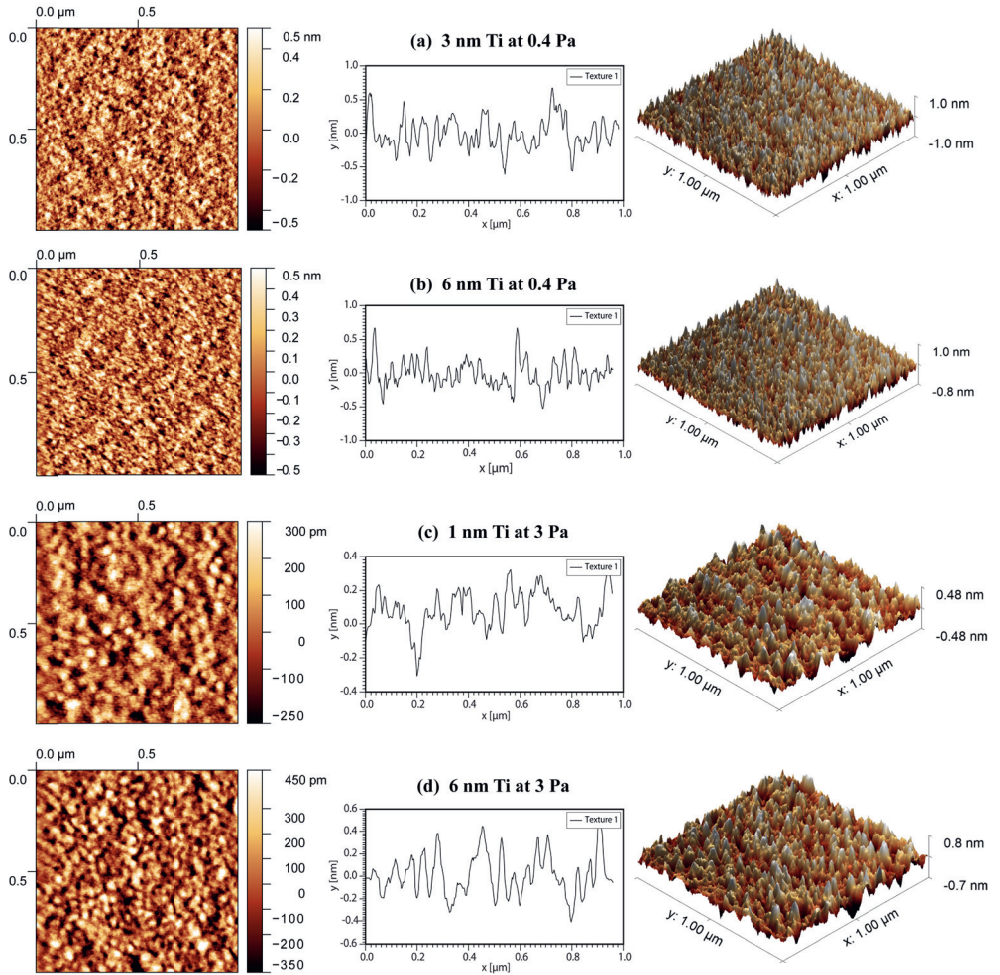


Figure 2.2 – AFM (2D and 3D) images $1\ \mu\text{m} \times 1\ \mu\text{m}$ and line profiles (in middle) of Ti layers deposited on SiO_2/Si substrate at different Ar pressures and with different layer thicknesses. (a) Ar pressure: 0.4 Pa; layer thickness: 3 nm, (b) Ar pressure: 0.4 Pa; layer thickness: 6 nm, (c) Ar pressure: 3 Pa; layer thickness: 1 nm, and (d) Ar pressure: 3 Pa; layer thickness: 6 nm. The white or lighter areas represent the peaks of Ti islands, whereas the dark regions indicate deep valleys between Ti islands.

2.3.2. Scanning Transmission Electron Microscopy

The morphological and compositional changes in the as-deposited films Pd and Pd on Ti layers were investigated by STEM in cross-section.

2.3.2.1. Ti intermediate layer characterization

STEM analysis of Pd film with 6 nm Ti intermediate layer deposited at 3 Pa Ar pressure is shown in Figure 2.3. The annular dark-field (ADF) image shows low-density areas due to an anisotropic columnar structure, consisting of tapered voids at part of the grain boundaries (GB) for Pd film in Figure 2.3(a). For the Pd on Ti layers, the Ti composition was investigated using a local probe in STEM mode to make an elemental map for Pd, Ti, Si, and O, respectively, shown in Figure 2.3(b). The Ti map demonstrates a relatively sharp transition from a Si-rich region to a Ti-rich region. The Pd map shows no sharp Pd-Ti interface but rather an extended mixed region. The first image (ADF) in Figure 2.3(b) also clearly displays spotty contrast in the Ti layer suggesting an uneven composition. Pd-rich islands are visible in the Ti layer indicating the formation of a discontinuous Ti layer. In Figure 2.3(c) EDX line-scans, showing the (horizontal) average obtained from the area indicated in the maps were used to illustrate compositional variations in the vertical directions. The line-scan confirms some overlap of Ti and Pd. The spatial resolution is 1-2 nm, so the overlap between Si and O on the one hand and Ti on the other hand, cannot be observed.

The high-resolution TEM (HRTEM) images of Pd-Ti interface show crystalline areas in the Ti layer for Ti deposited at 3 Pa (inset in Figure 2.3(a)), and lattice fringes detected only at a few locations for Ti layer deposited at 0.4 Pa (inset in Figure 2.4(b)). Detailed inspection of TEM data, shows that the Ti intermediate layer is mostly amorphous when deposited at 0.4 Pa, and partly amorphous and partly crystalline at 3 Pa Ar pressure. An amorphous to crystalline transition has been reported at 3-4 nm depending on the deposition conditions [26]. These observations corroborate the results obtained from AFM analysis of Ti layers deposited on SiO₂/Si substrate.

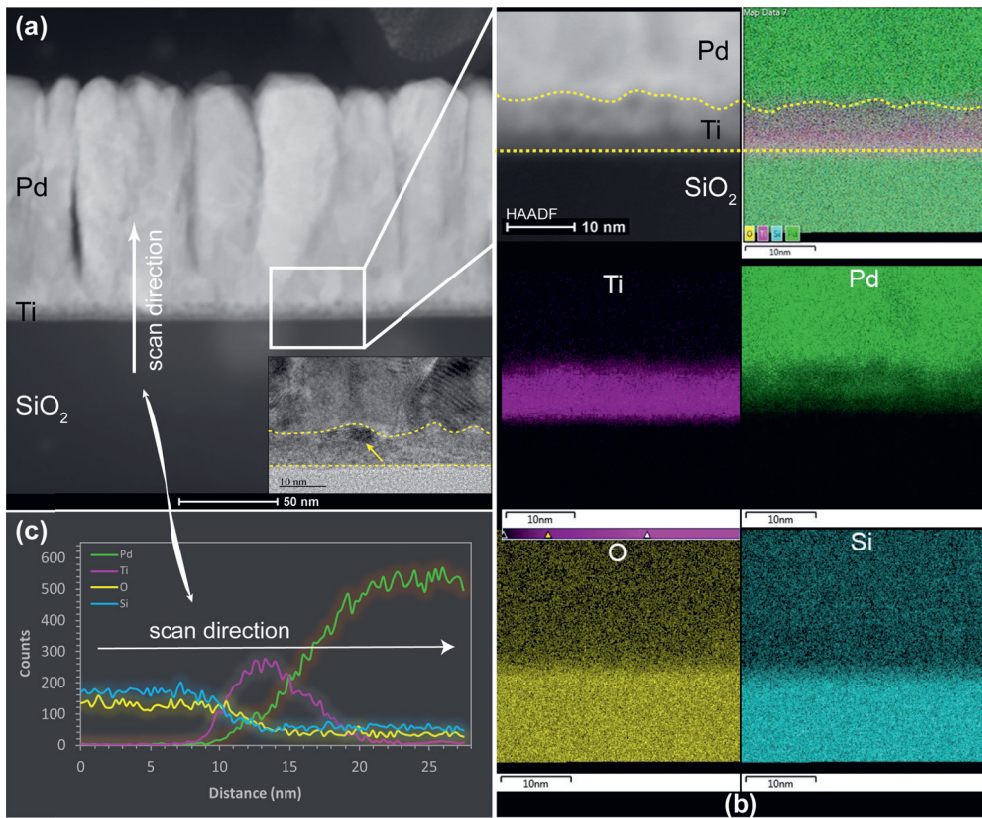


Figure 2.3 – STEM analysis of as-deposited film Pd on Ti-SiO₂/Si (6 nm Ti at 3 Pa). (a) Cross-sectional ADF STEM overview image (50 nm), showing low-density areas (voids) in between the Pd columnar grains as dark elongated areas. Inset HR-TEM image of the Ti-Pd interface showing the rough Ti layer. The yellow arrow indicates a small crystalline area with (2.3 ± 0.1) and (2.6 ± 0.1) Å spacings consistent with Ti lattice spacings. (b) The ADF image in the top-left corner indicates roughness and uneven contrast in the Ti layer. The individual Ti, Pd, O and Si layers can be clearly distinguished based on their elemental maps. Pd rich islands are visible in the middle of the Ti layer while Si-Ti and O-Si transitions are smooth. (c) EDX count line-scan profile (counts for each element) taken from the substrate (bottom) to the top from the maps, obtained by adding the spectra along ~25 nm in the horizontal direction perpendicular to the line scan. Quite some overlap of Ti and Pd is observed.

2.3.2.2. Pd thin film morphology

For Pd films deposited using 3 Pa Ar pressure at room temperature, a porous columnar structure is expected according to Thornton's structure zone model [44, 45]. The STEM image shows columnar structure, consisting of tapered voids at part of the grain boundaries for Pd film without intermediate layer (Pd-SiO₂/Si) (Figure 2.4(a)). To improve adhesion attempts were made to deposit Pd film with open columnar morphology on a Ti intermediate layer deposited onto SiO₂/Si substrate. This was indeed observed for Pd on Ti layer (6 nm at 3 Pa), see STEM image in Figure 2.3(a); a classic zone-1 morphology characterized by columnar structures with voids from nearly bottom to the top as achieved for Pd film without Ti layer. We observed, however, that the Pd on Ti layer morphologies depend on the underlying Ti intermediate layer's thicknesses and deposition pressure because of the resulting surface topography. Also at the early stage of deposition, near the substrate, the Pd grain structure is tightly packed due to the limited surface mobility attributed to adhesive nature of Ti intermediate layer [22]. Although the existing structure zone model [45] does not account for the influence of the underlying substrate surface condition. But Okolo et al., [29] in their work demonstrated that it is possible to obtain Cu thin film microstructures of varying morphology as a function of the substrate surface condition.

Concerning Pd on Ti layer, the development in Pd film growth morphology with underlying substrate (Ti-SiO₂/Si) surface condition shows a similar effect. For Pd films deposited on a thinner Ti intermediate layer at 3 Pa with a thickness of 1 nm, an open columnar structure was formed only for the top 2/3 part of the Pd film, the bottom part near the Pd-Ti interface consists mostly of densely packed columns as shown in Figure 2.4(b). Apparently, at the early stage of deposition, the morphology of Pd film is affected by the surface topography of the Ti intermediate layer, but as the Pd layer thickness increases, this effect of the substrate is expected to weaken. In the case of the 1 nm deposited at 3 Pa, the Ti layer surface is continuous and smooth in Figure 2.4(b) inset as compared to the Ti layer of 6 nm, see Figure 2.3(a) inset.

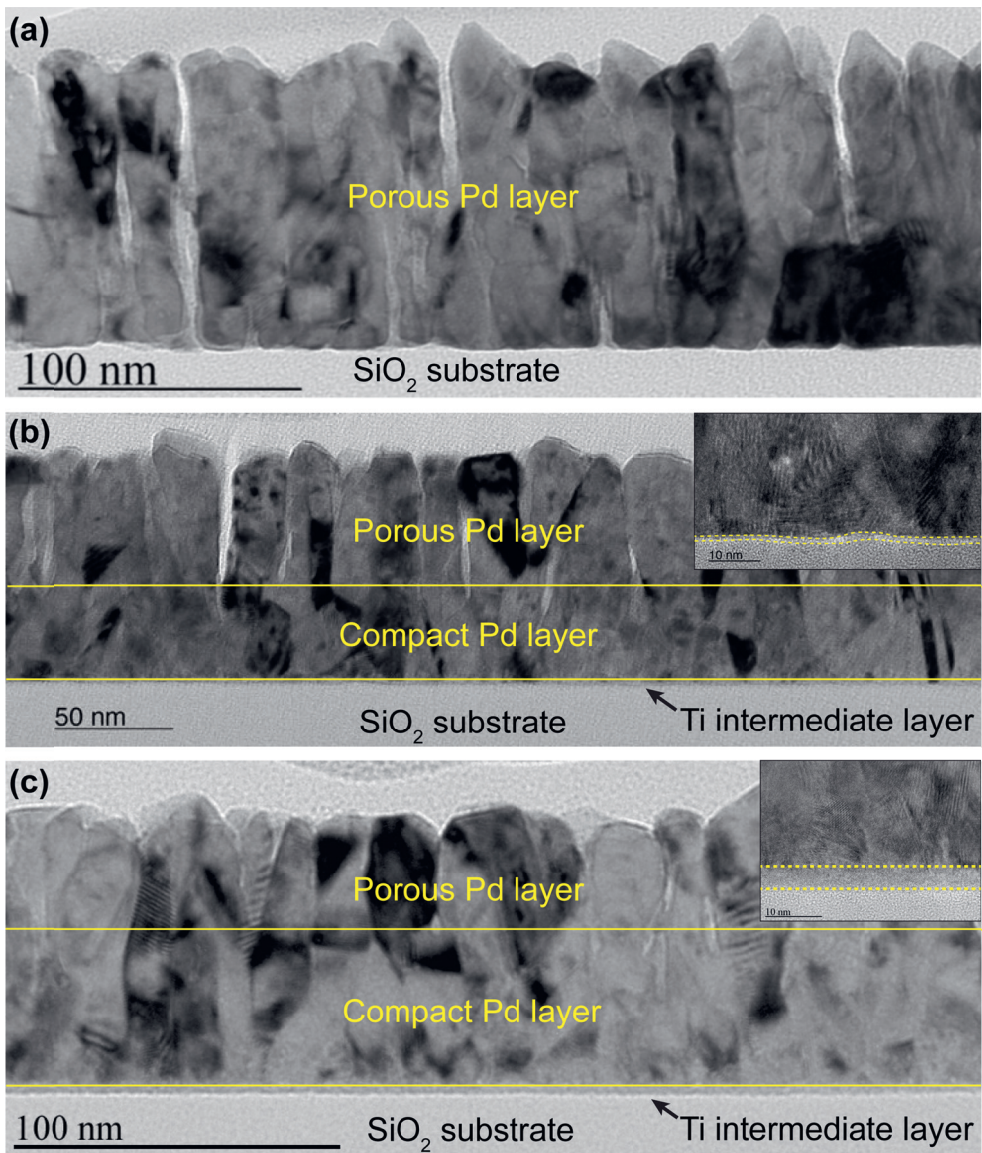


Figure 2.4 – Cross-section bright field images of as-deposited Pd films. (a) Pd on SiO₂/Si substrate without Ti intermediate layer showing vertical voids between Pd columnar structures extending from bottom to the top of the film. Pd on Ti-SiO₂/Si films: (b) Pd on Ti layer (1 nm at 3 Pa), showing porous columnar morphology for the top 2/3 part and compact structure at the Ti-Pd interface, inset is a HR-TEM image. (c) Pd on Ti layer (6 nm at 0.4 Pa), showing porous columnar morphology only at the top of the film and the rest of the film is relatively compact. The inset is a HR-TEM images showing the Ti layer. There is no evidence of a reaction at the interface between Pd layer and Ti intermediate layer for both films.

For Pd deposited under the same conditions (3 Pa) on the smoother Ti layers, deposited at 0.4 Pa, a more compact columnar structure was observed similar to that deposited on the 1 nm Ti layer at 3 Pa, as shown in Figure 2.4(b). The HR-TEM image in Figure 2.4(c) inset shows the smooth surface of Ti layer with uniform thickness deposited at 0.4 Pa. Due to the difference in Ti layer growth mechanism at 3 Pa and 0.4 Pa, irrespective of Pd deposition conditions, a Pd film with increasingly compact columnar structure developed, as shown in Figure 2.4(c). With the increase in thickness, during Pd sputtering the adatom surface mobility increases [44] as the free surface moves away from the Ti layer and the Pd deposition conditions dominate. Eventually, an open columnar structure develops only for the top 1/3 thicknesses of 100 nm Pd thin film.

The formation of small Ti islands at 0.4 Pa reflected by the lower mean spacing (S_m) values (Table 2.2) resulted in a smooth topography. While at 3 Pa, Ti layer rough surface; due to the effect of the large well-separated islands as reflected in the higher kurtosis value (Table 2.2) promotes the formation of increased hillocks. These observations indicate that the intermediate layer roughness is an important parameter in determining the overlayer film morphology. A similar influence of substrate surface conditions determining the initial stage of the film growth morphology has been reported for Cu thin films [46]. This morphological development in the Pd thin films is related to the texture evolution and has also been reported for Nickel thin film [24]. In next section, the effect of Ti intermediate layer surface topography on the crystallographic texture of Pd films (Pd and Pd on Ti layer) is addressed.

2.3.3. X-Ray Diffraction

2.3.3.1. Pd films: Texture strength and sharpness

All Pd films, Pd and Pd on Ti layers show a (111) fiber texture (no dependence on the rotation angle ϕ occurred). Figure 2.5 shows the fiber texture plots (FTP) from the {111}-Pd reflection. Overall the Pd on Ti layers have the highest texture strength and sharpness. The peak at $\psi = 0^\circ$ and at $\psi = 70.5^\circ$, belong to the {111} fiber texture component. The intensities at other tilt angles are from randomly oriented grains. The Pd film deposited directly on SiO₂/Si substrate develops a weak and broad (1.4x random) texture, as presented in the inset plot Figure 2.5. A comparison of the texture plots indicates that grains of this Pd film are much more randomly oriented than in $\langle 111 \rangle$ preferred direction. In addition, the half-width at

half-maximum (HWHM) of the (111) pole at $\psi = 0^\circ$ represents texture strength evolution from a very broad texture for Pd film to a very sharp texture for films Pd on Ti layers.

The strong and sharp (111) fiber texture developed for Pd on Ti layers (3 nm and 6 nm) deposited at 0.4 Pa Ar pressure can be ascribed to the larger adatom diffusion length on the smooth surface of the Ti layer [29]. On top of such smooth surface Pd (111) planes grow to form the densely packed planes growing mainly parallel to the surface. While on a rough surface, the diffusion length of the adatoms decreases [23] and the average angle of incidence is limited [28], both these factors limit the formation of (111) oriented grains parallel to the surface. Therefore, the diffusion of Pd adatoms is not sufficient to overcome the surface roughness of SiO₂ substrate; hence, the deposited Pd film shows a weak texture and large random oriented fraction. Similarly, the observation of the weak and broad texture (inset plot in Figure 2.5) of the Pd on Ti layer (6 nm at 3 Pa) with rough Ti surface topography can be explained. AFM and TEM analysis in above sections support the presence of smooth surface for Ti layer deposited at 0.4 Pa and rough surface for Ti layer deposited at 3 Pa.

Furthermore, it was found that at 3 Pa Ar pressure increasing Ti intermediate layer thickness from 1 nm to 6 nm had a drastic effect on the Pd texture strength and sharpness. While weak texture is obtained for Pd on Ti layer (6 nm at 3 Pa), but Pd film with 1 nm of Ti layer at 3 Pa has a strong texture similar to Pd on Ti layers (3 nm and 6 nm at 0.4 Pa). This difference in texture can be related to increase surface roughness when further Ti deposition leads to the progressive formation of a pure Ti film [41]. In addition, the amorphous and crystalline structure of Ti intermediate layer is altered at 3-4 nm depending on the deposition conditions [26]. From the present results, it is not possible to say if the change in Pd texture is caused by the amorphous Ti to crystalline Ti transition when the Ti layer thickness increases from 1 nm to 6 nm. This, however, could explain the observations and could be a means to tune Ti surface features without altering the Pd film microstructure.

Adapting the Ti layer surface topography can be used to control the Pd film growth microstructure. The surface roughness affects both the morphology and the texture such that Pd films with open columnar morphology have a weak and broad (111) texture and with increasing Pd layer compactness the 111 texture strength and sharpness increases. A similar effect has been reported for Cu thin films [46] when Cu microstructure changed from porous columnar morphology on the rough Al₂O₃ substrate to dense morphology on the smooth Al₂O₃ substrate.

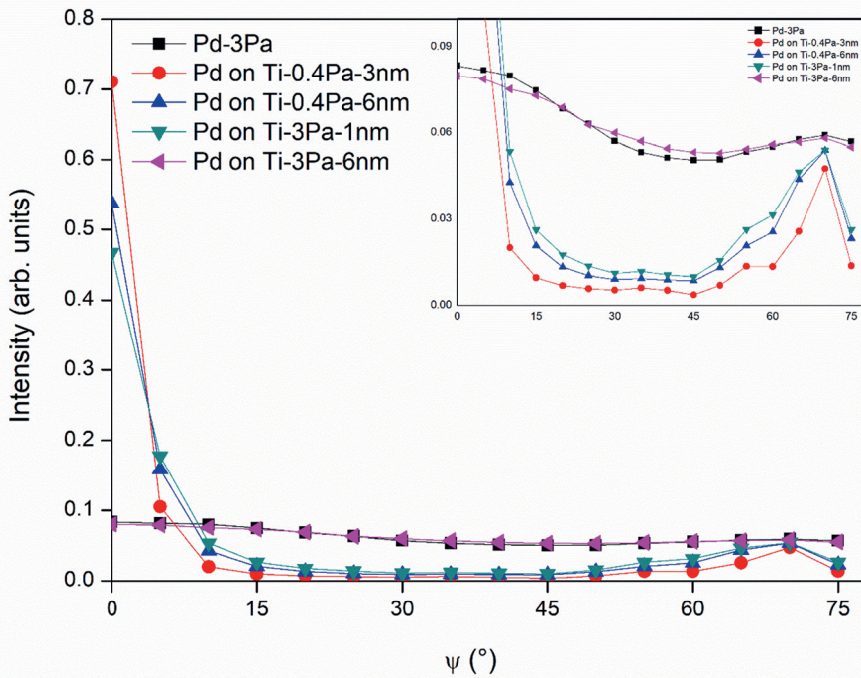


Figure 2.5 – (111) fiber texture plot (FTP) of as-deposited films: Pd-SiO₂/Si and Pd-Ti-SiO₂/Si (all Pd films are deposited at 3 Pa Ar pressure). Ti layer deposition parameters are provided in Table 2.1. The FTPs show that strength and sharpness of texture depend on deposition conditions of the Ti layer. Pd films on a Ti intermediate layer exhibit a distinctly stronger and sharper texture than the one without Ti layer, except for Pd on Ti layer (6 nm at 3 Pa). The inset details the broad and weak fiber texture.

2.3.3.2. Pd films: Hydrogen absorption kinetics

The effect of the Pd film microstructure on its performance during hydrogen loading was tracked by *in-situ* XRD experiments during phase transformation from α -Pd to β -PdH_{0.64}. A complete $\alpha \rightarrow \beta$ phase transformation was observed for Pd film on a SiO₂/Si substrate. Phase transformation was incomplete for Pd on Ti layers: a small fraction of α -Pd phase remained untransformed in equilibrium with β -hydride.

The plots of the amount of absorbed hydrogen as a function of time are presented in Figure 2.6(a). For the Pd film without Ti intermediate layer, a complete phase transition to the β -phase occurred in less than 4 min. While for Pd on Ti layers, a complete transformation to the β -phase was never attained. None of the Pd on Ti layers studied in this work showed complete suppression of transformation to β , as was reported earlier to occur due to substrate clamping by Kim *et al.* [18].

For the films Pd on Ti layer with the strongest/sharpest texture, it took about 90 min to reach the maximum capacity of loading. The partial phase transformation and slower kinetics are ascribed to the adhesive nature of Ti intermediate layer combined with the relatively less open columnar morphology of Pd film. Both hinder expansion of the lattice needed for the formation of β -hydride (a relative volume expansion of about 10% occurs upon transformation). In our previous work [21], hydrogen loading/deloading cycling experiments on similar specimens showed indeed that in Pd films on SiO_2/Si substrate clamped with Ti adhesive layer a twice as high compressive stress develops upon hydrogen loading than for unclamped Pd films.

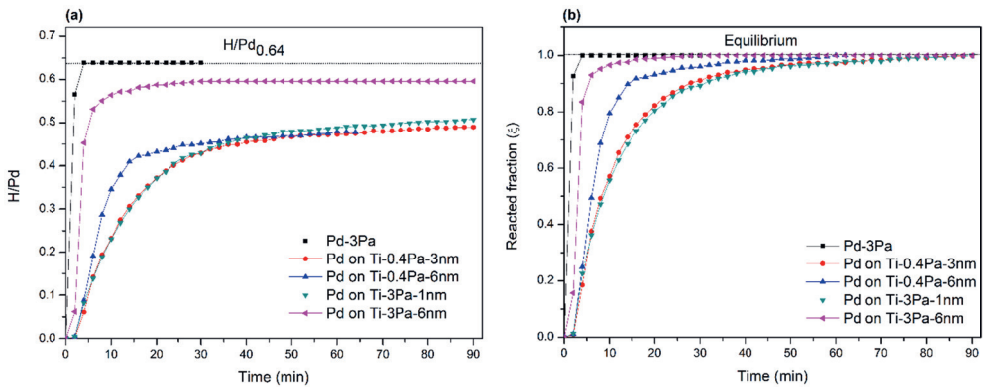


Figure 2.6 – (a) Absorbed hydrogen content vs. time and (b) the reacted fraction, ξ vs. time for the first hydrogen loading/deloading cycle for Pd thin films: Pd (Pd- SiO_2/Si) and Pd on Ti layers (Pd-Ti- SiO_2/Si).

To establish the rate-determining mechanism of hydrogen absorption, the experimental results were interpreted by fitting various rate equations [34] to the time-dependent hydrogen absorption curves. Figure 2.6(b) shows the curves of the calculated reacted fraction, ξ vs time for different films, illustrating that films Pd and Pd on Ti layer (6 nm at 3 Pa) took the least time to reach equilibrium. For Pd on Ti layers, improvement in hydrogen absorption kinetics

is observed as texture strength and sharpness decreases. As explained in above sections weak and broad texture corresponds to Pd with open columnar structure on Ti layer.

The ξ - t curves in Figure 2.6(b) consist of several segments (stages) over the entire reaction range. This is in line with the fact that hydride formation involves a sequence of elementary steps, as classified by Bloch and Mintz [47]. The variation in hydrogen absorption rate $d\xi/dt$ with time was used to find the respective stages of the reaction [35]. In $d\xi/dt$ vs time curve, every abrupt change corresponds to a new reaction mechanism function (new stage). The reaction mechanisms for each stage of hydrogen absorption as observed are listed in Table 2.3. In Figure 2.7 plots of $g(\xi)$ as a function of time are given for the rate-determining reaction mechanism for the various stages of transformation and their linear fits; see also (Table 2.3). Each line segment represented a different stage in which a different reaction mechanism is a determinant.

The hydrogen absorption process for Pd films on Ti layer consists of three stages: an incubation period (stage-I) followed by a fast hydrogen absorption stage (stage-II) during which about 90% of the equilibrium is reached and a final hydrogen absorption stage (stage-III).

For the Pd film without Ti layer, there is no observable incubation time, and about 95% of the $\alpha \rightarrow \beta$ phase transformation occurs in the first 2 minutes. Complete transformation to the β -phase was finished within 4 min in stage-II. The rate-determining hydrogen absorption process in stage II is 2-dimensional (radial) diffusion ($kt = (1 - (1 - \xi)^{1/2})^2$).

For Pd on Ti layer with strong and sharp $\{111\}$ texture, a short incubation period exists (stage-I). The incubation stage is dominated by the inward growth of the β -phase after rapid nucleation at the surface of cylindrical shaped particles, i.e., geometric contraction ($kt = 1 - (1 - \xi)^{1/2}$). In stage-II the first-order transformation reaction, $kt = -\ln(1 - \xi)$, is rate-determining. In the last stage, stage-III, diffusion-controlled transformation of spherical/cubic-like particles ($kt = (1 - (1 - \xi)^{1/3})^2$; 3-dimensional diffusion determines the absorption. This stage is absent for the Pd film without an intermediate layer. Therefore, this stage is most probably associated with the transformation of the compact layer of small grains near the Ti layer (see Figures 2.4(b&c)).

For the broad and weak textured film Pd on Ti layer (6 nm at 3 Pa), the incubation stage is absent, and hydrogen absorption process in stage II is dominated by 2-dimensional diffusion

reaction, similar to the Pd film without Ti layer. Stage-III is again dominated by 3-dimensional diffusion ($kt = (1 - (1 - \xi)^{1/3})^2$).

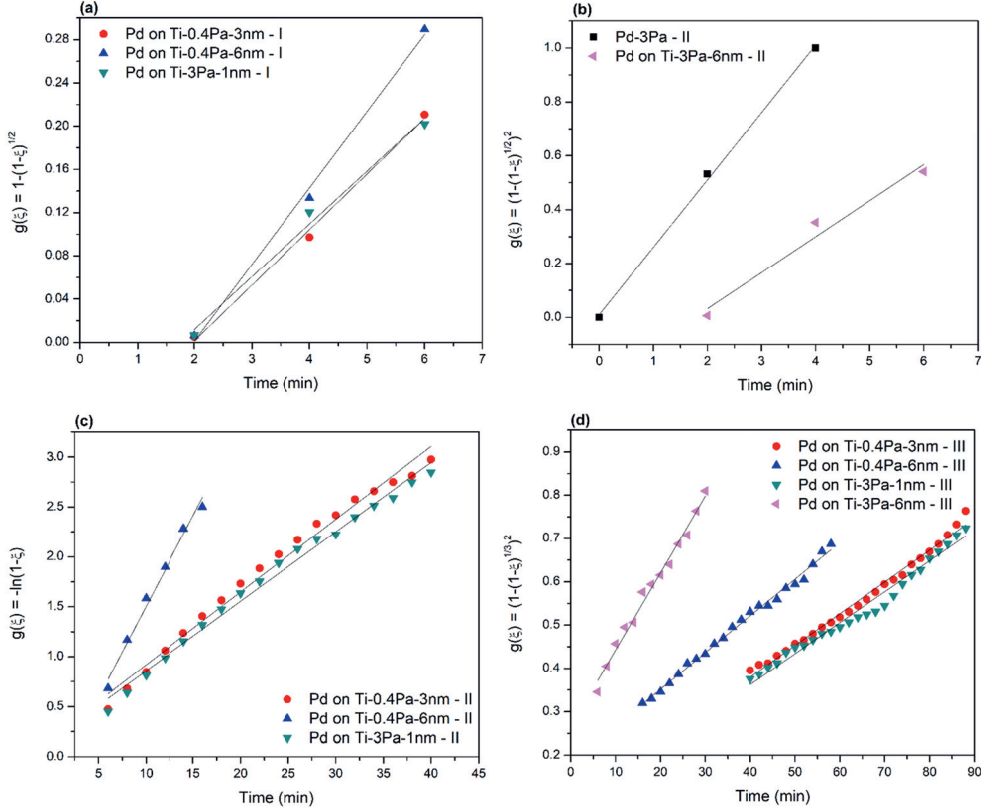


Figure 2.7 – The most suitable reaction mechanism at the different hydrogen absorption stages (I, II, III) for thin films Pd (Pd-SiO₂/Si) and Pd on Ti layers (Pd-Ti-SiO₂/Si): $g(\xi)$ as a function of time. Reaction stages for each film with best fit rate equations $g(\xi)$ are listed in Table 2.3.

Table 2.3 reports the reaction rate constants obtained from the slopes of $g(\xi)$ vs. time from Figure 2.7. The value of the rate constant followed the relation k -(stage-I) < k -(stage-II) > k -(stage-III). The absorption processes and the rate constants for Pd on Ti layer (6 nm at 3 Pa) in stage-II are close to those of a Pd film without Ti intermediate layer. This indicates that by changing the Ti layer deposition conditions, it is possible to tune the Pd film morphology in such a way that both fast hydrogen absorption kinetics and good adhesion to the substrate are attained. This work shows how engineering the surface topography of the adhesive

intermediate layer allows controlling morphology and texture of the thin film deposited on top of it.

Table 2.3 reports the reaction rate constants obtained from the slopes of $g(\xi)$ vs. time from Figure 2.7. The value of the rate constant followed the relation $k\text{-(stage-I)} < k\text{-(stage-II)} > k\text{-(stage-III)}$. The absorption processes and the rate constants for Pd on Ti layer (6 nm at 3 Pa) in stage-II are close to those of a Pd film without Ti intermediate layer. This indicates that by changing the Ti layer deposition conditions, it is possible to tune the Pd film morphology in such a way that both fast hydrogen absorption kinetics and good adhesion to the substrate are attained. This work shows how engineering the surface topography of the adhesive intermediate layer allows controlling morphology and texture of the thin film deposited on top of it.

Table 2.3 – Reaction mechanism stages and rate constants of hydrogen absorption for thin films Pd and Pd on Ti layers. All correlation coefficients are between 0.98 and 1.0.

<i>Pd film</i>	<i>Ti layer deposition pressure (Pa)</i>	<i>Ti layer thickness (nm)</i>	<i>Reaction stage</i>	<i>Best fitting equation $g(\xi)$</i>	<i>Rate constant k (min^{-1})</i>
Pd-SiO₂/Si	-	-	II	$(1 - (1 - \xi)^{1/2})^2$	0.250 ± 0.016
			I	$1 - (1 - \xi)^{1/2}$	0.051 ± 0.005
			II	$-\ln(1 - \xi)$	0.073 ± 0.014
			III	$(1 - (1 - \xi)^{1/3})^2$	0.007 ± 0.001
	0.4	3.0	I	$1 - (1 - \xi)^{1/2}$	0.071 ± 0.002
			II	$-\ln(1 - \xi)$	0.106 ± 0.016
			III	$(1 - (1 - \xi)^{1/3})^2$	0.008 ± 0.003
			I	$1 - (1 - \xi)^{1/2}$	0.049 ± 0.008
Pd-Ti-SiO₂/Si	3.0	1.0	II	$-\ln(1 - \xi)$	0.070 ± 0.015
			III	$(1 - (1 - \xi)^{1/3})^2$	0.007 ± 0.003
			I	$1 - (1 - \xi)^{1/2}$	0.133 ± 0.025
	6.4	6.4	II	$(1 - (1 - \xi)^{1/2})^2$	0.133 ± 0.025
			III	$(1 - (1 - \xi)^{1/3})^2$	0.018 ± 0.004
			I	$1 - (1 - \xi)^{1/2}$	0.049 ± 0.008

2.4. Conclusion

The microstructure of sputter-deposited ~ 100 nm Pd thin film on Ti-SiO₂/Si substrate depends strongly on the surface topography of the Ti adhesive intermediate layer. AFM surface topographic analysis of the sputter deposited Ti intermediate layer showed that the limited surface mobility of adatoms and shadowing at high deposition pressure (3 Pa) resulted in a rough surface of large well-separated Ti islands. At low sputter pressure (0.4 Pa) densely packed small Ti islands form by fast diffusion to surface defects, resulting in a smooth layer.

The surface effect of the underlying intermediate layer with respect to the Pd film morphology and texture was investigated using TEM and XRD techniques. The smooth surface topography of the intermediate layer led to a strong and sharp (111) fiber texture and a compact columnar morphology of the Pd film. A rough intermediate layer surface topography results in a weak and broad (111) texture, and a more open columnar morphology with voids. This can be understood in terms of the intermediate layer's roughness and, the resulting Pd adatom diffusion and shadowing effects during the magnetron sputtering process. Pd on Ti layer (6 nm at 3 Pa) has a weak and broad {111} texture similar to Pd film deposited directly on SiO₂/Si substrate.

Combined with *in-situ* X-ray diffraction hydrogenation study, the results were used to optimize Ti intermediate layer deposition parameters for improved Pd thin film adhesion and mechanical stability on a rigid substrate. The hydrogen absorption behaviour of Pd on Ti layers depends on their morphology. The more open columnar structure allows faster absorption and results in higher hydrogen absorption capacity than for the compact morphology. In all Pd on Ti layer, a small amount of Pd remains un-transformed in contrast to the Pd film without an adhesive layer that fully transforms. The Pd film deposited on a Ti layer (6 nm at 3 Pa) that has an open morphology and a weak and broad {111} texture showed similar absorption behaviour as the Pd film without Ti adhesive layer.

This study provides a comprehensive understanding of how surface topography of the adhesive intermediate layer influences the morphology and texture of overlying thin films. This enables to tailor Pd films with good adherence to a substrate, with morphological and absorption properties suited for specific applications like H₂ gas purification or sensing.

2.5. References

- [1] Paglieri S, Way J. Innovations in palladium membrane research. *Separation & Purification Reviews*. 2002;31:1-169.
- [2] Mendes D, Mendes A, Madeira L, Iulianelli A, Sousa J, Basile A. The water-gas shift reaction: from conventional catalytic systems to Pd-based membrane reactors—a review. *Asia-Pacific Journal of Chemical Engineering*. 2010;5:111-37.
- [3] Rostrup-Nielsen JR, Rostrup-Nielsen T. Large-scale hydrogen production. *Cattech*. 2002;6:150-9.
- [4] Flanagan TB, Oates W. The palladium-hydrogen system. *Annual Review of Materials Science*. 1991;21:269-304.
- [5] Burkhanov GS, Gorina NB, Kolchugina NB, Roshan NR, Slovetsky DI, Chistov EM. Palladium-based alloy membranes for separation of high purity hydrogen from hydrogen-containing gas mixtures. *Platinum Metals Review*. 2011;55:3-12.
- [6] Nanu D, Böttger A. Phase stabilities of Pd-based alloys for membranes for hydrogen gas separation: A statistical thermodynamics approach. *J Alloy Compd*. 2007;446:571-4.
- [7] Zeng G, Jia H, Goldbach A, Zhao L, Miao S, Shi L, et al. Hydrogen-induced high-temperature segregation in palladium silver membranes. *Phys Chem Chem Phys*. 2014;16:25330-6.
- [8] Checchetto R, Bazzanella N, Patton B, Miotello A. Palladium membranes prepared by rf magnetron sputtering for hydrogen purification. *Surface and Coatings Technology*. 2004;177:73-9.
- [9] Bientinesi M, Petarca L. Preparation of thin film Pd membranes for H₂ separation from synthesis gas and detailed design of a permeability testing unit. New York: Nova Science Publishers; 2010.
- [10] Li H, Caravella A, Xu H. Recent progress in Pd-based composite membranes. *Journal of Materials Chemistry A*. 2016;4:14069-94.
- [11] Kumar S, Singh A, Jain U, Dey GK. Development of tantalum–zirconium alloy for hydrogen purification. *Fusion Engineering and Design*. 2016;109:1487-90.
- [12] Bryden KJ, Ying JY. Nanostructured palladium membrane synthesis by magnetron sputtering. *Materials Science and Engineering: A*. 1995;204:140-5.
- [13] Baldi A, Narayan TC, Koh AL, Dionne JA. In situ detection of hydrogen-induced phase transitions in individual palladium nanocrystals. *Nature materials*. 2014;13.
- [14] Natter H, Wettmann B, Heisel B, Hempelmann R. Hydrogen in nanocrystalline palladium. *J Alloy Compd*. 1997;253:84-6.
- [15] Greco F, Ventrelli L, Dario P, Mazzolai B, Mattoli V. Micro-wrinkled palladium surface for hydrogen sensing and switched detection of lower flammability limit. *Int J Hydrogen Energ*. 2012;37:17529-39.
- [16] Wagner S, Pundt A. Quasi-thermodynamic model on hydride formation in palladium–hydrogen thin films: Impact of elastic and microstructural constraints. *Int J Hydrogen Energ*. 2016;41:2727-38.
- [17] Harumoto T, Ohnishi Y, Nishio K, Ishiguro T, Shi J, Nakamura Y. In-situ X-ray diffraction study of hydrogen absorption and desorption processes in Pd thin films: Hydrogen composition dependent anisotropic expansion and its quantitative description. *AIP Advances*. 2017;7:065108.
- [18] Kim KR, Noh J-S, Lee JM, Kim YJ, Lee W. Suppression of phase transitions in Pd thin films by insertion of a Ti buffer layer. *J Mater Sci*. 2010;46:1597-601 DOI: 10.1007/s10853-010-4970-x.

- [19] Vlček M, Lukáč F, Vlach M, Procházka I, Wagner S, Uchida H, et al. Hydrogen-Induced Buckling of Pd Films Deposited on Various Substrates. *Defect and Diffusion Forum*. 2015;365:55-62.
- [20] Čížek J, Melikhova O, Vlček M, Lukáč F, Vlach M, Procházka I, et al. Hydrogen-induced microstructural changes of Pd films. *Int J Hydrogen Energ*. 2013;38:12115-25.
- [21] Verma N, Böttger AJ. Stress development and adhesion in hydrogenated nano-columnar Pd and Pd/Ti ultra-thin films. *Advanced Materials Research*. 2014;996.
- [22] Pivak Y, Schreuders H, Slaman M, Griessen R, Dam B. Thermodynamics, stress release and hysteresis behavior in highly adhesive Pd-H films. *Int J Hydrogen Energ*. 2011;36:4056-67.
- [23] Harpera J, Rodbell K. Microstructure control in semiconductor metallization. *J Vac Sci Technol B*. 1997;15.
- [24] Priyadarshini BG, Aich S, Chakraborty M. Structural and morphological investigations on DC-magnetron-sputtered nickel films deposited on Si (100). *J Mater Sci*. 2011;46:2860-73.
- [25] Chan K-Y, Teo B-S. Sputtering power and deposition pressure effects on the electrical and structural properties of copper thin films. *J Mater Sci*. 2005;40:5971-81.
- [26] Jeyachandran Y, Karunagaran B, Narayandass SK, Mangalaraj D, Jenkins T, Martin P. Properties of titanium thin films deposited by dc magnetron sputtering. *Materials Science and Engineering: A*. 2006;431:277-84.
- [27] Chawla V, Jayaganthan R, Chawla A, Chandra R. Microstructural characterizations of magnetron sputtered Ti films on glass substrate. *journal of materials processing technology*. 2009;209:3444-51.
- [28] Whitacre J, Rek Z, Bilello J, Yalisove S. Surface roughness and in-plane texturing in sputtered thin films. *Journal of applied physics*. 1998;84:1346-53.
- [29] Okolo B, Lamparter P, Welzel U, Wagner T, Mittemeijer E. The effect of deposition parameters and substrate surface condition on texture, morphology and stress in magnetron-sputter-deposited Cu thin films. *Thin Solid Films*. 2005;474:50-63.
- [30] De Oliveira R, Albuquerque D, Cruz T, Yamaji F, Leite F. Measurement of the nanoscale roughness by atomic force microscopy: basic principles and applications. *Atomic Force Microscopy-Imaging, Measuring and Manipulating Surfaces at the Atomic Scale: InTech*; 2012.
- [31] Chateigner D, Germin P, Pernet M. Texture analysis by the Schulz reflection method: defocalization corrections for thin films. *Journal of applied crystallography*. 1992;25:766-9.
- [32] Scardi P, Leoni M, Dong Y. Texture determination in highly stressed PVD thin films. *Advances in X-ray Analysis*. 2000;42:492-501.
- [33] Cullity BD, Stock SR. *Elements of X-ray Diffraction*: Pearson Education; 2014.
- [34] Khawam A, Flanagan DR. Solid-state kinetic models: basics and mathematical fundamentals. *The journal of physical chemistry B*. 2006;110:17315-28.
- [35] Kumar S, Taxak M, Krishnamurthy N. Hydrogen absorption kinetics of V4Cr4Ti alloy prepared by aluminothermy. *Int J Hydrogen Energ*. 2012;37:3283-91.
- [36] Kumar S, Singh A, Tiwari GP, Kojima Y, Kain V. Thermodynamics and kinetics of nano-engineered Mg-MgH₂ system for reversible hydrogen storage application. *Thermochimica Acta*. 2017;652:103-8.
- [37] Ishiyama K, Taga Y, Ichimiya A. Reactive adsorption and diffusion of Ti on Si (001) by scanning tunneling microscopy. *Physical Review B*. 1995;51:2380.
- [38] Arranz A, Palacio C. The room temperature growth of Ti on sputter-cleaned Si (100): Composition and nanostructure of the interface. *Surf Sci*. 2005;588:92-100.
- [39] Iida S, Abe S. Ti thin-film reaction on SiO₂/Si. *Appl Surf Sci*. 1994;78:141-6.
- [40] Butz R, Wagner H. Reactions at the Ti/SiO₂ Interface Studied by EELS. *physica status solidi (a)*. 1986;94:71-6.

- [41] Wallart X, Zeng H, Nys J, Dalmai G, Friedel P. An Auger and electron energy-loss study of reactions at the Ti-SiO₂ interface. *Journal of applied physics*. 1991;69:8168-76.
- [42] Mahan JE. Physical vapor deposition of thin films. *Physical Vapor Deposition of Thin Films*, by John E Mahan, pp 336 ISBN 0-471-33001-9 Wiley-VCH, January 2000. 2000:336.
- [43] Ohring M. *Materials science of thin films*: Academic press; 2001.
- [44] Petrov I, Barna P, Hultman L, Greene J. Microstructural evolution during film growth. *J Vac Sci Technol A*. 2003;21:S117-S28.
- [45] Thornton JA. Influence of apparatus geometry and deposition conditions on the structure and topography of thick sputtered coatings. *Journal of Vacuum Science & Technology*. 1974;11:666-70.
- [46] Bai P, McDonald JF, Lu TM, Costa MJ. Effect of substrate surface roughness on the columnar growth of Cu films. *J Vac Sci Technol A*. 1991;9:2113-7.
- [47] Bloch J, Mintz MH. Kinetics and mechanisms of metal hydrides formation—a review. *J Alloy Compd*. 1997;253:529-41.

3

The role of the substrate on the mechanical and thermal stability of Pd thin films during hydrogen (de)sorption²

In this chapter, we studied the mechanical and thermal stability of ~100 nm Pd thin films magnetron sputter deposited on a bare oxidized Si(100) wafer, a sputtered Titanium (Ti) intermediate layer, and a spin-coated Polyimide (PI) intermediate layer. The dependence of the film stability on the film morphology and the film-substrate interaction was investigated. It is shown that a columnar morphology with elongated voids at part of the grain boundaries is resistant to embrittlement induced by the hydride formation ($\alpha \leftrightarrow \beta$ phase transitions). For compact film morphology, depending on the rigidity of the intermediate layer and the adherence to the substrate, complete transformation (Pd-PI-SiO₂/Si) or partial suppression (Pd-Ti-SiO₂/Si) of the α to β -phase transition was observed. In the case of Pd without intermediate layer (Pd-SiO₂/Si), buckling delamination occurred. The damage and deformation mechanisms could be understood by the analysis of the stresses and dislocation (defects) behavior near grain boundaries and the film-substrate interface. From diffraction line-broadening combined with microscopy analysis, we show that in Pd thin films, stresses relax at critical stress values via different relaxation pathways depending on film-microstructure and film-substrate interaction. On the basis of the in-situ hydriding experiments, it was concluded that a Pd film on a flexible PI intermediate layer exhibits free-standing film-like behavior besides being strongly clamped on a stiff SiO₂/Si substrate.

² This chapter has been published as:

N. Verma, R. Delhez, N.M. van der Pers, F.D. Tichelaar, A.J. Böttger, *The role of the substrate on the mechanical and thermal stability of Pd thin films during hydrogen (de) sorption*, International Journal of Hydrogen Energy, vol. 46, pp. 4137-4153, 2020.

3.1. Introduction

In recent years, substantial amounts of research were performed on Palladium (Pd) in view of a future hydrogen economy [1-5]. Since Pd readily absorbs hydrogen even at low pressure and room temperature [6, 7], Pd and its alloys [8] are suitable for hydrogen purification [9], hydrogen storage [10], hydrogen gas sensors [11], and fuel cell catalysts [12]. However, primary requirements for the application are not always satisfied, such as usability under operation conditions (temperature and pressure), minimum investment cost, and sustain hydrogen embrittlement [13-17].

Hydrogen absorption properties in metals depend on the microstructure and have been studied from this point of view for several metal-hydrogen (M-H)-systems [18]. The various microstructures offer different types of hydrogen trapping sites, in bulk and as well as in nanostructured thin films. Nanostructured Pd has shown high hydrogen diffusivity due to grain boundaries that act as a network of fast diffusion pathways [19, 20]. Nanosizing also dramatically alters material properties, which are strongly affected by the presence of crystallographic defects. Ulvestad *et al.* [21] and Narayan *et al.* [22] demonstrated that the ability of the defective Pd nanoparticle to remove crystallographic imperfections is the reason for nano-sized system's durability under the stresses resulting from large volume changes during hydrogen absorption and desorption. They also showed that these microstructural defects act as additional barriers to the phase transformation. Similar observations were made in nanocrystalline Pd films [23].

In thin films, large mechanical stresses are induced when loaded with hydrogen as caused by an elastic constrain from the substrate [24, 25], known as substrate clamping. When the in-plane expansion is suppressed by adhesion to the substrate, high compressive in-plane stresses are built [26, 27]. These high internal stresses are the cause of buckling [28] and local or complete detachment of the film from the substrate at a certain critical concentration of absorbed hydrogen [29, 30]. Larger hysteresis occurred upon hydrogen loading/deloading cycles in clamped than in free-standing films [28, 31]. The buckling of the hydrogen-loaded thin film itself significantly increases the dislocation activity (plastic deformations) [32]. Considering the state of the literature described, we compared differences in the microstructural behavior as induced by hydrogen (de)sorption of various Pd thin films with and without an adhesive intermediate layer. Direct observation of stresses and dislocation mediated deformations were estimated using X-ray diffractometry (XRD) during *in-situ* hydriding experiments.

A study based on positron annihilation spectroscopy showed that plastic deformation leads to an increase of the defect density upon hydrogenation in various Pd films [33]. Amin-Ahmadi *et al.* [23] discussed the dislocation/hydrogen interaction mechanisms in hydrided nanocrystalline Pd films and showed that local plasticity in β -phase could be controlled by dislocation activity. Similar to the stress, the defects (dislocations) in thin films also led to a slower hydrogen uptake [34]. At a given deformation level, dislocations propagate and interact with pre-existing structures and also with each other, thus, makes up the final microstructure of the deformed state [18]. Stress relaxation in Pd thin film after phase transitions can be explained by the process in which change in dislocation structure plays a dominant role.

Pd thin films have limited structural stability when exposed to hydrogen gas even at room temperature, owing to the $\alpha \leftrightarrow \beta$ phase transitions [33, 35, 36]. The nature of the substrate, the adhesion to the substrate and the microstructure of the film are all of importance for stability [37]. It was shown that tuning the microstructure through magnetron sputtering [38], and adapting the adhesion [39] and state of stress adjusted by the nature of the underlying substrate [40] enables improvement of the film stability.

In this paper, a comprehensive *in-situ* X-ray diffraction (XRD) experimental study is presented to demonstrate the role of the film microstructure and intermediate layer material on the mechanical stability of Pd thin films exposed to hydrogen. The influence of film-substrate adhesion and deposition parameters of the film is found to have a profound effect both on the response of hydrogen uptake and mode of damage. It is shown that annealing significantly impacts Pd thin film performance and stability. These findings were further supported by the observation that stress relaxation mechanisms are different for Pd films with a comparable microstructure but deposited with different adhesive intermediate layer on a stiff substrate. The films have been characterized by XRD to obtain macro-stress, texture and defect parameters through line-broadening analysis using integral breadth [41, 42]. Transmission and scanning electron microscopy (TEM and SEM) are applied to investigate morphological changes.

3.2. Experimental

3.2.1. Pd thin film preparation

Two series of Palladium thin films were dc magnetron sputter deposited in an ATC 1500F sputter deposition system from AJA International. Series-1 films were deposited for 480 s at low Ar pressure of 0.4 Pa, with an average deposition rate of 0.2 nm/s. Series-2 films were deposited for 900 s at high Ar pressure of 3 Pa, with an average deposition rate of 0.1 nm/s. The base pressure of the deposition chamber was 1.3×10^{-5} Pa and argon was used as a sputtering gas. As a substrate, thermally oxidized (~ 188 nm) 2-inch single-crystal Si(100) wafers (SiO_2/Si) were used with and without an intermediate layer. Two different adhesive intermediate layers were laid between Pd film and SiO_2/Si substrate: (i) a sputter-deposited 6 nm Titanium (Ti) layer ($\text{Ti-SiO}_2/\text{Si}$), or (ii) a spin-coated 5 μm thick polyimide (PI) layer ($\text{PI-SiO}_2/\text{Si}$). All depositions were performed with a substrate temperature of 293 K.

The Ti layer deposition on the SiO_2/Si wafer was performed at two working Ar pressures, 0.4 Pa (for series-1) and 3 Pa (for series-2) for 70 s and 360 s, respectively. Polyimide spin-coating on the SiO_2/Si wafer was performed at Else Kooi Lab (EKL), TU Delft. Before PI spin coating, the wafers were primer coated with VM652 primer at 3500 rpm for 10 s, to promote adhesion of PI to the wafers, followed by a 5 μm thick layer of PI Duramide 115A spin-coated at 4000 rpm. The PI layer was soft-baked at 388 K for 15 s and subsequently cured at 673 K for 2 h.

3.2.2 TEM and SEM: morphology analysis

The cross-sectional morphology of the Pd thin film was characterized using CM30T and CM300UT-FEG Philips Transmission Electron Microscopy (TEM), type Tecnai F20ST/STEM (FEI Electron Microscopes) with energy dispersive spectroscopy (EDS). The investigated TEM foils were prepared by Argon-ion milling of a cross-sectional cut protected by a glass plate glued to the film. The surface morphology of the Pd thin films was examined using Scanning Electron Microscopy (SEM) - JEOL JSM 6500F, equipped with a Thermo Fisher Ultradry detector with Noran system 7 data-acquisition and data-analysis software.

3.2.3. X-ray diffraction (XRD)

In-situ X-ray diffraction (XRD) measurements were used to investigate hydrogen-induced changes in texture, stress and microstructure of Pd thin films during hydrogen loading/deloading (absorption and desorption). Two different diffractometers, one with parallel-beam geometry (CoK α) and one with focusing geometry (CuK α), were used.

3.2.3.1. Texture and stress measurements

The simultaneous stress/texture measurements were performed on a Bruker-AXS D8 Discover diffractometer equipped with polycapillary optics (0.25°) and Eulerian cradle in parallel beam geometry (CoK α ; 45 kV, 25 mA). Data were collected over 2θ ranges that cover the whole diffraction peak at different sample orientations (ψ tilting the sample at fixed rotation angle ϕ). The rotational symmetry of the texture was confirmed by additional pole figures measurement. The integrated intensities of the {111} reflection were presented as a fiber texture plot (FTP) displaying the distribution of the texture components about the fiber axis from the center ($\psi = 0^\circ$) to the outer edge ($\psi = 75^\circ$). The integrated intensities after a linear background fitting were obtained using the Bruker - EVA software [43]. Measured intensities were corrected for thin layer and instrumental intensity loss [44].

The same measured scans were used to determine the in-plane stresses and data evaluation was done with the PANalytical X'Pert Stress Plus [45]. Stress states were determined using the conventional $\sin^2\psi$ method [46]. From the Pd-{311} reflection, the lattice plane spacing, d_ψ , was determined. In this work, the Neerfeld-Hill average values [46] for the X-ray elastic constants (XECs), $S_1(311)$ and $\frac{1}{2}S_2(311)$ were taken, -3.25 and 11.49 TPa^{-1} for Pd; and -3.28 and 11.60 TPa^{-1} for PdH_{0.66}, respectively at 300 K, as calculated from Pd single-crystal elastic constants [47]. It should be noted that, in addition to crystallographic texture, the sputter-deposited columnar grain structure is responsible for the macroscopic anisotropy [48]. Therefore, we estimated the stress in Pd thin films based on a single-crystal type analysis [49] using only the crystallites with {111} planes parallel to the film surface. Those crystallites contribute to the {311} FTP with maxima at 29.5° and $58.5^\circ \psi$ -tilt angles.

For series-1 films, the data from the maxima at 29.5° and $58.5^\circ \psi$ -tilt angles were used. Since series-2 films used in this study have weak and broad {111} fiber texture, at least three ψ tilt angles were used around 29.5° and $58.5^\circ \psi$ -tilt angles for the stress measurements. The stress parallel to the surface $\sigma_{//}$ was calculated from the slope of the straight line fitted to the data in the plot of d_ψ^{hkl} versus $\sin^2\psi$.

3.2.3.2. XRD line-broadening: microstructure characterization

The deformation mechanisms in terms of defect parameters such as crystallite sizes and lattice strain due to dislocations were obtained by line-broadening analysis of X-ray diffraction profiles using the integral breadth [42]. These were determined by profile fitting to the measured line profiles after $K\alpha_2$ -stripping using the least-squares multi-peak fitting implemented in Igor Pro [50], assuming a linear background and a Voigt function line shape. This profile fitting was found to be necessary because most of the line profiles used showed a small but distinct overlap with neighboring reflections.

For line-broadening analysis, Pd- $\{111\}$, $\{311\}$ and $\{222\}$ hkl reflections were selected from "long scans" made on the Bruker D5005 (section 3.2.4.2). The $\{220\}$ reflection was not measured because of interfering Si(400) reflection from SiO_2/Si wafer substrate. Further, the $\{200\}$ reflection was not used for analysis because the overlap with the $\{111\}$ reflection was found to affect fitting results. The instrumental profile was determined by measuring, under analogous conditions, a reference specimen of NIST/NBS LaB_6 powder (SRM660a) [51] on a (510) Si single-crystal substrate. Standard deviations for the integral breadth (β) were estimated by measuring ten times the four HKL reflections of a Pd- SiO_2/Si specimen, then used as an estimate of the standard deviations of all measurements. This seems justified because only small differences between the β_{hkl} values for the various specimens and treatments are observed. Similarly, for the instrumental profile, seven identical scans were performed and from the integral breadth values of each reflection, the average and standard deviation were calculated.

The measured XRD peak profile or measured broadening is the result of the convolution of the instrumental broadening of the diffractometer and the broadening introduced by microstructural imperfections in the sample called micro-structural broadening [41]. The instrument-corrected broadening β_{hkl} corresponding to the diffracted peak of Pd thin film was estimated using:

$$\beta_{hkl} = [(\beta_{hkl})^2_{\text{measured}} - (\beta_{hkl})^2_{\text{instrumental}}]^{1/2} \quad (3.1)$$

because the shape of all line profiles involved was close to Gaussian as found from profile fitting.

In the rest of this study β^*_{hkl} , the integral breadth in reciprocal space is used instead of β_{hkl} :

$$\beta_{hkl}^* = \beta_{hkl} \cos \theta / \lambda \quad (3.2)$$

It is assumed here that the microstructural broadening was caused by macrostrain induced broadening arising from crystal imperfections and small crystallite size, and that the effects of broadening by these two components are additive of the total integral breadth of a Bragg peak.

There was no effect found of stacking and twin faults in the measured lattice constants [52]. Therefore the line breadths were assigned to dislocations and evaluated by the modified Williamson-Hall (mod-WH) method [53, 54]. The method accounts for the anisotropic strain fields of dislocations by introducing the Contrast Factor C_{hkl} . C_{hkl} depends on the types, densities, and arrangements of the dislocations present, as well as on the orientation distribution of the dislocations with respect to the diffraction vector g_{hkl} .

$$\beta_{hkl}^* = \frac{K}{\langle D \rangle} + \left(\frac{\pi M^2 b^2}{2} \right)^{\frac{1}{2}} \left[\frac{h^2 + k^2 + l^2}{a^2} \right]^{\frac{1}{2}} \rho^{\frac{1}{2}} C_{hkl}^{\frac{1}{2}} \quad (3.3)$$

where K is a constant (here taken = 1), $\langle D \rangle$ (nm) is the average crystallite size (here perpendicular to the Pd layers), M is a constant describing the dislocation arrangement [55] (here taken = 1), ρ is the dislocation density (m^{-2}), b is the Burgers vector, and a is the lattice constant. The contrast factors C_{hkl} are tabulated in the Appendix A (see Table A1). The contrast factors C_{hkl} were calculated (see Appendix A1) for untextured material containing randomly oriented screw and edge dislocations of the $\{111\}$, $a/2\langle 110 \rangle$ slip system and of other slip systems, using the anisotropic elastic constants for Palladium (the values used of the elastic compliances s_{11} , s_{12} and s_{44} are 13.7444, -5.99504 and 14.0351 TPa^{-1} , respectively [46].

3.2.4. Experimental set-up for *in-situ* hydriding

The hydrogen absorption and desorption in Pd thin film were observed by collecting diffraction patterns during hydrogen loading/deloading experiments performed on two different *in-situ* XRD.

3.2.4.1. Room-temperature

For direct visualization of the topographic changes on Pd film surface, one hydrogen loading/deloading cycle at room-temperature (RT) was performed in a custom-made sample holder on the Bruker D8 Discover (see 3.2.3.1) using $\text{CoK}\alpha$ radiations. The sample holder consists of a cavity covered by a transparent foil (4 μm Chemplex Propylene) that enables to capture (via eyes and camera) pictures of the surface (Figures 3.4(a-i)) during *in-situ* measurement under continuous gas flow. Diffraction patterns were collected over a “short-scan” in the range $43\text{--}49^\circ 2\theta$ (including the Pd- $\{111\}$ α and β phase), under the following conditions: (i) as-deposited specimen in air, (ii) during hydrogen loading in H_2/N_2 gas ($p(\text{H}_2) = 0.05$ atm) at 2 minutes interval up to complete α to β phase transition; and (iii) during hydrogen deloading in air, every 2 minutes until complete transition back to Pd metallic state containing “no” hydrogen.

3.2.4.2. Above room-temperature

Several loading/deloading conditions were investigated *in-situ* above room-temperature using a Bruker D5005 diffractometer in Bragg-Brentano focusing geometry ($\text{CuK}\alpha$; 40 kV, 30 mA), equipped with MRI HT chamber. The chamber is equipped with a mass flow controller for N_2 (1 atm) gas and H_2/N_2 ($p(\text{H}_2) = 0.05$ atm). The chamber is at atmospheric pressure. The specimen was mounted on a Pt-Rh heater strip with a fixed S-type thermocouple. Another thermocouple K-type was placed on the specimen surface to measure the actual specimen temperature.

3.2.4.2.1. Phase transitions: 303 K – 353 K (PT-only)

For the detection of hydrogen-induced transformations in Pd film, diffraction patterns were recorded in the H_2/N_2 gas mixture in 10 K steps from 303 K–353 K. Phase transitions (PT) were tracked by measuring the Pd- $\{111\}$ reflections of the α - and β -phase. Diffraction patterns for monitoring PT were collected over a “short scan” in the range $36\text{--}43^\circ 2\theta$ with a step size of 0.04° , using a fixed slit. The net peak area was used as a measure for the phase amounts. For the analysis of the microstructure (through line-broadening), XRD patterns of the film before (as-dept.) and after phase transitions (after-PT) were collected in N_2 gas atmosphere using a “long scan” over three ranges: $35\text{--}43^\circ 2\theta$ (including the Pd- $\{111\}$), $43\text{--}50^\circ 2\theta$ (including the Pd- $\{200\}$) and $77\text{--}90^\circ 2\theta$ (including the Pd- $\{311\}$ and $\{222\}$ reflections). The long scans were recorded using a variable divergence slit to achieve data with a constant irradiated length for the whole 2θ range.

3.2.4.2.2. High-temperature annealing prior to phase transitions (HT+PT)

For high-temperature (HT) stability assessment, the Pd thin film was annealed in H_2/N_2 gas mixture up to 625 K before conducting the phase transitions (PT). Diffraction patterns were recorded under the following conditions: (i) as-deposited long scan in N_2 gas (as-dept.); (ii) heating in N_2 gas until 373 K, followed by increasing the temperature in 10 K steps in the H_2/N_2 gas mixture to 473 K or 623 K, and annealing for 18 h; (iii) after annealing and cooling down to RT, a long scan in N_2 gas (after-HT); (iv) after HT step the $\alpha \leftrightarrow \beta$ phase transitions in the H_2/N_2 gas was examined between 303 K–353 K as explained above for PT-only; and finally (v) H_2/N_2 gas in the chamber was replaced by N_2 gas during desorption and long scan was collected (after-HT+PT).

3.3. Results and discussion

3.3.1. As-prepared Pd thin film microstructure

Pd thin films deposited at two sputter pressure conditions, 0.4 Pa (series-1) and 3 Pa (series-2), and three underlying substrate conditions, *i.e.*, with an intermediate layer (Ti or PI) and without an intermediate layer (bare SiO_2/Si), were investigated to examine microstructure, adhesion conditions to the substrate and consequently the film stability when exposed to hydrogen.

3.3.1.1. Morphology

Figures 3.1(a&b) shows TEM cross-sectional view of as-deposited series-1 Pd-Ti- SiO_2/Si and Pd-PI- SiO_2/Si films with compact morphology. SEM plane view in Figure 3.2(a) shows the smooth surface topography of series-1 film Pd on Ti layer. The smoothness of the surface and the higher packing density of the columns is because of energetic particle bombardment at low deposition pressure [56]. When the surface mobility of the sputtered Pd atoms is high, the islands formed merge while still very thin, thereby forming a continuous film without voids. For series-1 irrespective of underlying surface conditions, the Pd deposition conditions dominate to produce high density closed morphology. Thus, TEM and SEM micrographs in Figures 3.1(a&b) and 3.2(a) are representative of the as-deposited morphology of all series-1 films.

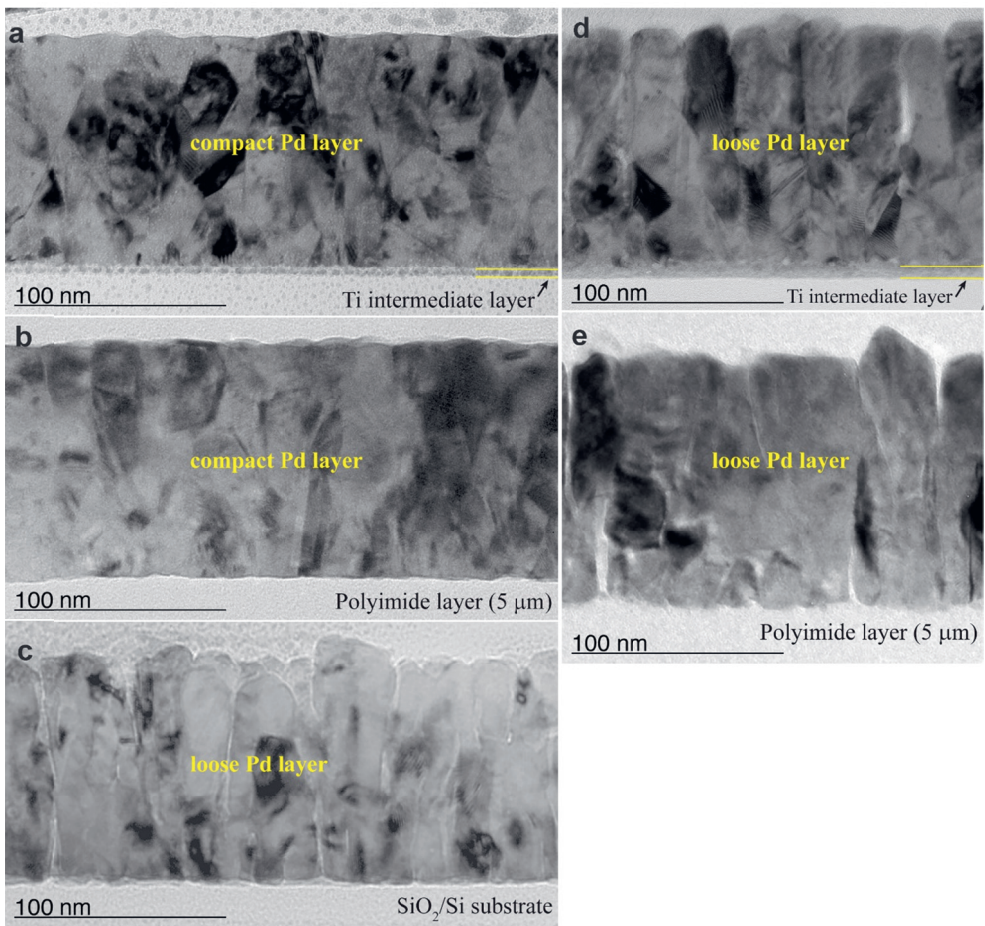


Figure 3.1 – A cross-sectional view of TEM bright-field (BF) images (100 nm scale) illustrating the growth morphology of as-deposited Pd thin films. Series-1 films morphology showing non-voided compact columnar nanostructures: (a) Pd-Ti-SiO₂/Si and (b) Pd-PI-SiO₂/Si. Series-2 films with and without intermediate layer: (c) Pd-SiO₂/Si, (d) Pd-Ti-SiO₂/Si and (e) Pd-PI-SiO₂/Si. All series-2 films have open columnar nanostructures with (nano)voids along the grain boundaries.

Pd films with relatively open morphology were obtained at high deposition pressure (series-2). Figures 3.1(c–e) shows TEM images of as-deposited series-2 films. For Pd-SiO₂/Si film in Figure 3.1(c), most of the vertical columnar structures are extending from the bottom to the top of the film; some, however, develop from clusters of small grains at the film-substrate interface. Adjacent columns are separated by voided-boundaries. SEM topography images in Figures 3.2(b–d) confirmed a low-density open morphology for series-2 films. SEM

micrographs clearly show a network of diffuse black lines indicating voids of different density and structure at the grain boundaries along with a microcrack network. These voided-boundaries stem from the decrease in the surface mobility of the adatoms after a series of collisions with the sputter gas under high deposition pressure, and as well as shadowing effects [57].

The columnar microstructure of Pd films is consistent with the predictions of Thornton's structure zone model (SZM) [57]. The Pd films were deposited at a substrate temperature of 293 K, and the homologous temperature ~ 0.2 (Pd melting temperature 1828 K taken from [58]). Along these lines, series-1 morphology with compact columnar structures belonging to Zone T and series-2 deposited at 3 Pa Ar pressure, with open columnar structures belong to Zone 1. In previous work [40], chapter 2, we have shown that underlying intermediate layer roughness is also a determining factor for obtaining Pd film with an open columnar morphology. Here for series-2 film Pd on Ti layer, we used optimized Ti intermediate layer deposition parameters (thickness and deposition pressure). Pd on Ti layer in Figure 3.1(d) shows a structure similar to Pd on bare SiO₂/Si substrate (Figure 3.1(c)) but with less/small voids along columnar boundaries due to the relatively smooth underlying Ti-SiO₂/Si substrate.

For Pd on PI layer, Figure 3.1(e) shows a rough Pd bottom, and less elongated grains are present; the columnar structure is composed of 2 or 3 grains over the thickness. The PI intermediate layer resulted in tilted Pd columns with irregularly voided-boundaries. The slow surface diffusion of adatoms and atomic shadowing results in adatom pile up on existing grains, thus favoring the formation of voided-boundaries [59]. By comparing the series-2 SEM images in Figures 3.2(b–d), it can be concluded that the Pd films deposited on SiO₂/Si and PI-SiO₂/Si substrates with a relatively rough surface have a more open columnar structure than Pd film on the smoother Ti-SiO₂/Si substrate. Here the small irregularities on the substrate act as extra nucleation sites enhancing the formation of an open columnar structure [60].

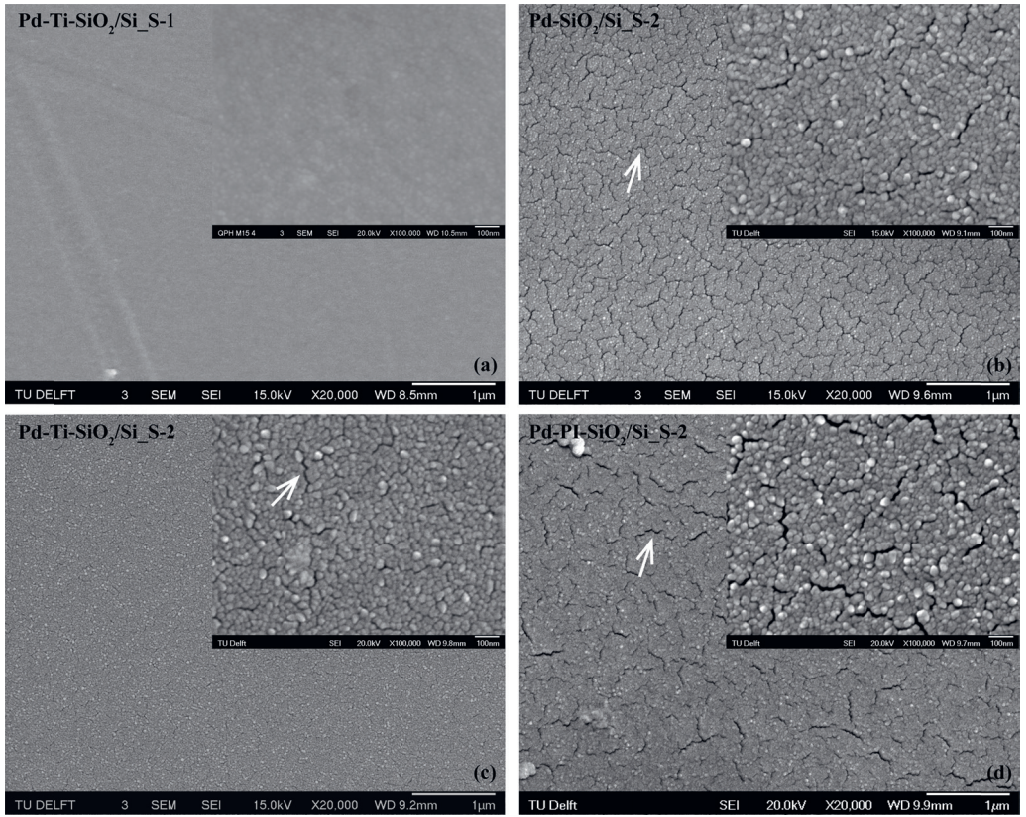


Figure 3.2 – SEM images illustrating surface morphology of as-deposited Pd thin films. (a) Series-1 (S-1) film surface is showing a high-density smooth topography for Pd-Ti-SiO₂/Si. All series-2 (S-2) films showing loose/open topography: (b) Pd-SiO₂/Si, (c) Pd-Ti-SiO₂/Si and (d) Pd-Pt-SiO₂/Si. The white arrows highlight the initial network of primary microcracks, which are associated with intercolumnar voids. The insets are high-magnification (100 nm) images of the Pd films.

3.3.1.2. Crystallographic texture

Figure 3.3 presents fiber texture plots (FTP) of the Pd-{111} reflection for both series-1&2 as-deposited films. The strength and sharpness of the {111} fiber texture is more pronounced for series-1 as compared to series-2 films. From the series-1 films, the Pd-SiO₂/Si and Pd-Ti-SiO₂/Si, show the strongest textured. FTP of all series-2 films indicates that (111) fiber texture is weak and broad. The fraction of randomly oriented grains is much larger for series-

2 films than series-1, as presented in the inset Figure 3.3. The deposition pressure is clearly the cause of the substantial difference in texture strength and sharpness. All in all, the low sputter pressure (series-1) leads to a closed columnar morphology with a strong and sharp fiber textured film, and the high sputter pressure (series-2) leads to a weak and broad fiber textured film with an open columnar morphology.

The sharpness of the texture is given in Table 3.1 by the half-width at half maximum, w , for the peak in the FTP at $\psi=0^\circ$. For Pd on PI layer, the $\{111\}$ fiber texture is somewhat broader for both series-1&2 films as compared to those of Pd on SiO_2/Si and Pd on $\text{Ti-SiO}_2/\text{Si}$. This texture evolution could be assigned to the rougher surface of the PI- SiO_2/Si substrate. On a rough surface, shadowing effects and anisotropic diffusion of the adatoms lowers the degree of texture [61]

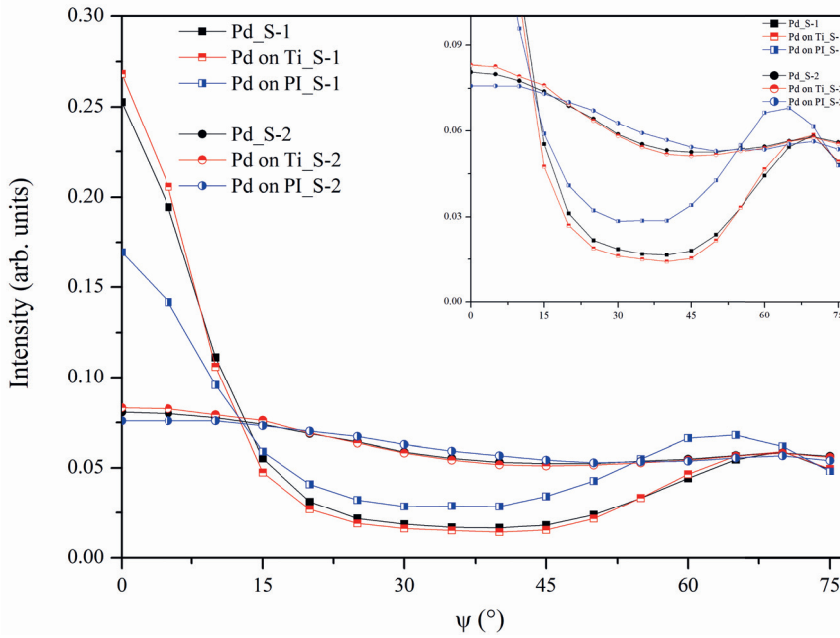


Figure 3.3 – Pd-(111) fiber texture plot (FTP) of as-deposited series-1 and series-2 films deposited on SiO_2/Si , $\text{Ti-SiO}_2/\text{Si}$ and $\text{PI-SiO}_2/\text{Si}$ substrates. Series-1 (S-1) films show clearly peaks at $\psi = 0^\circ$ and $\psi = 70.5^\circ$ for $\{111\}$ texture components. The inset shows series-2 (S-2) films with broad and weak fiber texture as compared to strong and sharp fiber texture for the series-1 films.

Table 3.1 – The half-width at half maximum (w) from Pd-(111) fiber texture plot in Figure 3.3 at $\psi=0^\circ$ for Pd films on SiO_2/Si substrate with and without intermediate layer deposited at 0.4 Pa Ar pressure (series-1) and 3 Pa Ar pressure (series-2).

<i>As-deposited Pd films</i>	<i>SiO_2/Si</i>	<i>$\text{Ti-SiO}_2/\text{Si}$</i>	<i>$\text{PI-SiO}_2/\text{Si}$</i>
Series-1, w (°)	9.6	9.2	13.6
Series-2, w (°)	22.7	22.3	28.4

3.3.1.3. Stress

In Table 3.2, comparing the growth stress in the as-deposited series-1 and series-2 films, it was found that – for series-1 (dense films), the in-plane stress ($\sigma_{//}$) is compressive, while for series-2 (open films) $\sigma_{//}$ is tensile.

For series-1, the values of the compressive growth stress are nearly the same for all Pd films (Table 3.2). This indicates that an intermediate layer has no major influence on growth stress when Pd is sputtered at low Ar pressure. In general, the intrinsic compressive stress observed in Zone T, dense film, is assigned to atomic peening during sputter deposition [62].

For series-2 films, the growth stress is tensile, and its magnitude depends on the type of intermediate layer (Table 3.2). Tensile stress observed in Zone 1, open (void-rich) film, is explained in terms of the grain boundary relaxation mechanism [38, 62] and island coalescence [50]. The tensile stress is higher for Pd on Ti layer with a relatively less open columnar structure. However, when during deposition, more voided morphology forms, the tensile stresses generated are not sustained, and stress relaxation occurs. This is the case for Pd on PI layer and for Pd on a bare SiO_2/Si . The nature of the growth morphology and the magnitude of the stresses in the film are sensitive to the deposition conditions [62] and influence the mechanical strength of thin films [63].

Table 3.2. In-plane stress, $\sigma_{//}$, for Pd films on SiO₂/Si substrate with and without intermediate layer during a single cycle of hydrogen loading/deloading at room-temperature. Pd film deposited at 0.4 Pa Ar pressure (series-1) and 3 Pa Ar pressure (series-2).

$\sigma_{//}$ (MPa)	Series-1			Series-2		
	SiO ₂ /Si	Ti-SiO ₂ /Si	PI-SiO ₂ /Si	SiO ₂ /Si	Ti-SiO ₂ /Si	PI-SiO ₂ /Si
As-deposited	-21 ± 9	-17 ± 34	-18 ± 10	43 ± 13	117 ± 13	95 ± 18
Loading	23 ± 8	-462 ± 28	-471 ± 23	17 ± 18	-88 ± 16	-50 ± 14
Deloading	200 ± 8	563 ± 20	655 ± 14	61 ± 19	380 ± 3	305 ± 8

3.3.2. Phase transformations: mechanical and thermal stability

When a Pd thin film is exposed to hydrogen, the α to β phase transition causes a volume increase of about 10.4 vol% [6]. Both the α -PdH_x phase and the β -PdH_x phase are of fcc structure [18]. The present study uses microscopic observations (TEM and SEM), measurements of the macro-stress, and the lattice defect densities to find out how hydrogen absorption and desorption of nanocrystalline Pd thin films might be influenced by their sputter deposition conditions and the underlying intermediate layer when deposited on a stiff substrate.

3.3.2.1. Room temperature

Visual observations of the Pd film topographic changes caused by hydrogen absorption were made through the transparent foil of the custom-made holder of *in-situ* XRD set-up (section 3.2.4.1). Series-1 Pd film on bare SiO₂/Si substrate subjected to hydrogen loading at RT showed buckle formation. In Figures 3.4(a–c) photographs made with 2 minutes interval displayed a gradual buckling (shiny silver areas) of the Pd film surface starting from edges and growing towards the center, Figure 3.4(b). The entire film specimen was found buckle-delaminated after completion of the $\alpha \rightarrow \beta$ phase transformation within 10 minutes, Figure 3.4(c). After hydrogen deloading, some buckles flattened, but still, features of the buckled patterns are visible in Figure 3.4(d). The *ex-situ* SEM analysis showed buckled and delaminated areas randomly scattered over the film surface in Figure 3.4(j). In the compact

series-1 films, the lack of voids to accommodate the expansion due to β -PdH_x phase formation during hydrogen uptake causes the building-up of compressive stress (Table 3.2). Only the Pd film on SiO₂/Si substrate β -phase showed buckling and delamination that causes the release of stress, see Table 3.2. The strong adhesion by the intermediate layers of Ti and PI prevents delamination (Figures 3.4(e–f)) and these films show a strong increase in the compressive stress (Table 3.2).

The more voided series-2 film on a bare SiO₂/Si substrate did not show any hydride-related topographical changes, and the surface remained flat during and after hydrogen is cycled, Figures 3.4(g–i). In Appendix A (Figures A1(a–d)) the diffraction patterns of series-1 and 2 for Pd on SiO₂/Si confirm the effect of buckling in the series-1 film and the integrity of the series-2 film. SEM image in Figure 3.4(k) shows the flat surface topography of series-2 film. The presence of space in the form of tapered voids along grain boundaries (Figure 3.1(c)) allows the relaxation of strains (Table 3.2).

The magnitude of structural deformation in compact films (series-1) was controlled by adding an adhesive intermediate layer between the film and the substrate. Figure 3.5(a) shows a schematic representation of series-1 films deposited with and without an intermediate layer: SiO₂/Si, Ti-SiO₂/Si and PI-SiO₂/Si. Here and in earlier work [40], we found that for Pd on Ti layer, the $\alpha \rightarrow \beta$ phase transformation was very slow and incomplete (a fraction of α -phase was not transformed). A similar observation was made in this work for Pd on PI layer; it took about 18 h to complete transformation into the β -phase. The slow hydride formation in these films is attributed to the compact morphology and the effect of clamping by the underlying adhesive intermediate layer that hinders lateral film expansion [26].

In series-2 films, the open columnar morphology is the dominating factor that surpasses the strong adhesion energy of the clamped film to the substrate, thus allowing free expansion of the film during loading and also channel stress release in Pd layer (Table 3.2). Series-2 films with an intermediate layer showed relatively fast $\alpha \rightarrow \beta$ phase transformation, and it took about 15–20 min to complete the transformation. These films showed no traces of buckling or film detachment as have been reported in the literature [29, 35, 36]. The thermal stability of series-2 films is discussed in the next section.

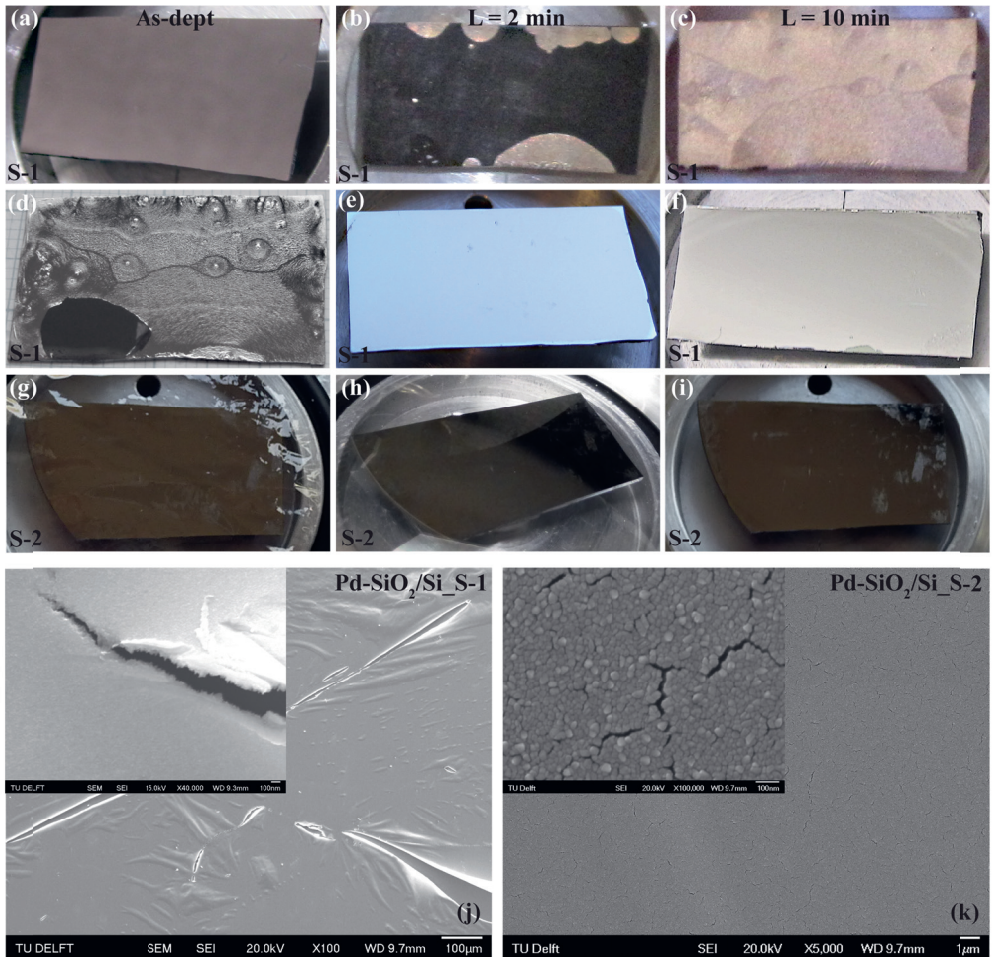


Figure 3.4 – Room-temperature single cycle of hydrogen loading/deloading. For visualization of the topography changes, specimen pictures were made through the XRD radiation box: (a–f) Series-1 (S-1) films: Pd-SiO₂/Si (a) as-deposited, b) during H-loading within 2 min interval shows gradual blistering (color contrast) of the Pd layer from the substrate, (c) complete H-loading in 10 min shows blistered pattern throughout the film surface. (d–f) after H-L/D cycle: (d) Pd-SiO₂/Si still shows features of the blistered pattern, (e) Pd-Ti-SiO₂/Si and (f) Pd-PI-SiO₂/Si shows smooth surface as in the as-deposited state. (g–i) Series-2 (S-2) film Pd-SiO₂/Si: (g) in as-deposited condition, (h) during H-loading and (i) after H-L/D cycle. (j–k) Ex-situ SEM images of Pd-SiO₂/Si films after loading/deloading cycle: (j) series-1 (S-1) showing buckled and cracked surface in a large image (100 mm scale) and delaminated area in inset image (100 nm) and (k) series-2 (S-2) showing the flat surface in a large image (1 mm scale) and film morphology like in the as-deposited condition (Figure 3.2(b)) in inset image (100 nm scale).

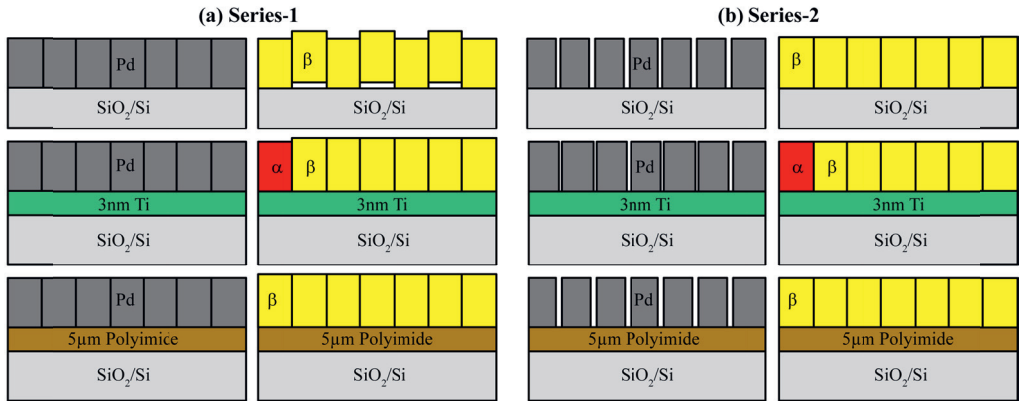


Figure 3.5 – A pictorial description of Pd films on SiO₂/Si, Ti-SiO₂/Si, and PI-SiO₂/Si substrates (top to bottom). (a) Series-1: left-side are as-deposited Pd films (grey: metallic, no H) with compact columnar morphology, and right-side are hydrogen-loaded Pd(H) films (yellow: high-H β -phase; red: low-H α -Phase) in the H₂/N₂ gas mixture for 10 min leading to buckling formation (Pd on bare SiO₂/Si), 420 min (Pd on Ti) and 1100 min (Pd on PI) respectively. Pd films with Ti and PI intermediate layer remained smooth as in the as-deposited state. (b) Series-2: left-side are as-deposited films with open columnar morphology and the right-side are hydrogen-loaded Pd films in the H₂/N₂ gas mixture. All series-2 films remained flat during loading without buckle formation.

3.3.2.2. Above room-temperature

3.3.2.2.1. Phase transitions: 303 K – 353 K (PT-only)

The film morphology and intermediate layer have a profound effect both on the hydrogen uptake response and mode of deformation in the Pd thin film system at room temperature. Here phase transitions were studied up to the critical temperature [6, 7] in series-2 films. Films were heated from 303 K to 353 K (in steps of 10 K) and subsequently cooled down to 303 K in the H₂/N₂ gas mixture. When the gas atmosphere was changed from N₂ gas to H₂/N₂ gas mixture at the starting temperature, 303 K, the diffraction patterns revealed an immediate α - to β -phase transition. Upon step-wise heating, in H₂/N₂ gas, the critical temperature was reached, and the β - to α -phase transition occurred at 333 K. While cooling down from 353 K, the α - to β -phase transition occurred at a lower temperature 313 K. At 303 K, the gas atmosphere was changed to N₂ gas, and the β - to α -phase transition occurred. Thus, in a PT-

only experiment (303 K \rightarrow 353 K \rightarrow 303 K), two cycles of hydrogen loading/deloading were covered, *i.e.*, $\alpha \rightarrow \beta$, $\beta \rightarrow \alpha$, $\alpha \rightarrow \beta$, $\beta \rightarrow \alpha$ (Figure 3.6(a)).

For all series-2 films, the material was fully transformed (from α to β and vice versa). The $\alpha \rightarrow \beta$ phase transition in Pd films without intermediate layer and with PI intermediate layer was completed in about 12 min. Phase transformation was incomplete for Pd film strongly clamped on Ti-SiO₂/Si substrate and took about 30 mins to reach the maximum amount of β -PdH_x hydride phase. This is in agreement with a previous observation that a Ti intermediate layer slows down the kinetics of hydrogen absorption/desorption significantly [40]. This slow kinetics is attributed both to the substrate clamping and Pd film morphology. For Pd on Ti layer with the dense bottom half (30 - 40 nm) and porous top half morphology [40], the formation of the β -PdH_x phase took approx. 120 min and a large fraction of α -PdH_x phase remained despite the fact that the film was kept for several hours in the H₂/N₂ gas atmosphere. This means open columnar structures largely contributes to improved response time and allows formable expansion during hydrogenation [6] when between α and β phases, a lattice mismatch of 3.5% generates large compressive stresses. These observations highlight that hydrogen uptake is strongly correlated to the film morphology.

The TEM (Figure 3.7(a)) and SEM (Figures 3.8(a-c)) results showed that all Pd films remained morphologically unperturbed after the PT-only experiment, irrespective of the presence of an intermediate layer. For temperatures up to 353 K, neither coalescence nor growth of the grains occurred. We noticed, however, an increase in the primary microcrack spacing after-PT (Figures 3.8(a&c) inset) as compared to as-deposited primary microcracks visible in Figures 3.2(b&d). In particular, the crack density is higher for Pd-SiO₂/Si film than for Pd-PI-SiO₂/Si film, while no such crack formation was observed for Pd-Ti-SiO₂/Si film. The microcracks proliferate at pre-existing defects and propagate along grain or grain boundaries, indicating intergranular fracture [64]. The intergranular cracks are often interconnected, forming a network of microcrack that can be detrimental to the mechanical strength of the film. But stress relaxation by microcrack propagation in these films prevents subsequent crack networks from developing unless they are sufficiently far away for the strain energy to build to a critical level. In the case that no microcrack widening is observed for Pd with Ti intermediate layer (Figure 3.8(b)), no stress release is observed (Table 3.3). The persistent increase of tensile stress most probably is also the cause of the slower hydrogen absorption in Pd on Ti layer.

It is expected that on mechanically soft PI-SiO₂/Si substrate, crack propagation [65] is more likely than on a mechanically hard Ti-SiO₂/Si substrate. For Pd on PI layer, the large compliance of the polyimide layer can increase microcrack spacing rearrangements and distance over which stresses are relaxed in the neighborhood of a crack [66]. The ease of propagation of a crack channeling in a film also depends on underlying substrate mechanical properties besides the stresses generated.

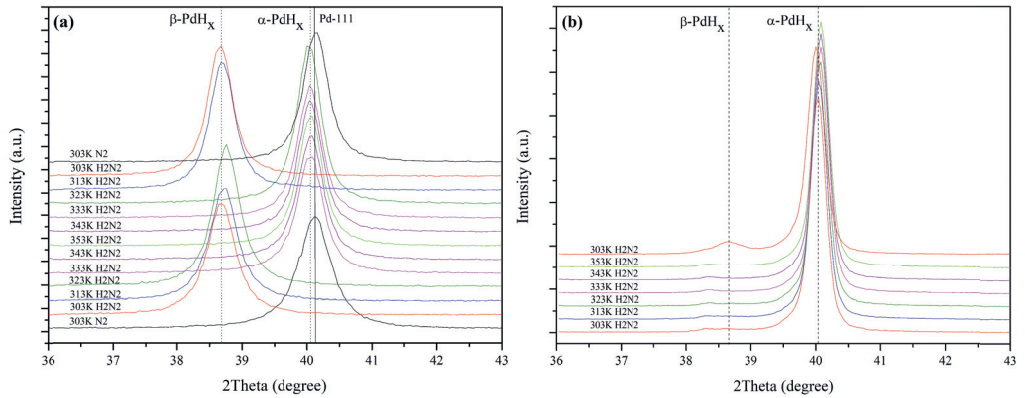


Figure 3.6 – XRD scans showing the $\{111\}$ reflections of the α - and β -phase for series-2 films: (a) complete $\alpha \leftrightarrow \beta$ phase transitions are observed for Pd-SiO₂/Si and Pd-PI-SiO₂/Si films both for PT-only and HT+PT, and (b) for Pd-Ti-SiO₂/Si film $\alpha \leftrightarrow \beta$ phase transitions are suppressed after annealing film at 623 K for 18 h followed by PT (HT+PT).

Table 3.3 – Measured stresses in series-2 films in as-deposited condition, after phase transitions (after-PT) from PT-only experiment and after phase transitions on annealed films (after-HT+PT) from HT+PT experiment. Note that different specimens were used for PT-only and HT+PT (taken from the same wafer).

Series-2 films	SiO ₂ /Si	Ti-SiO ₂ /Si	PI-SiO ₂ /Si
as-deposited, $\sigma_{//}$ (MPa)	147 ± 5	210 ± 5	82 ± 7
after-PT, $\sigma_{//}$ (MPa)	332 ± 5	451 ± 17	344 ± 20
after-HT+PT, $\sigma_{//}$ (MPa)	5 ± 5	430 ± 13	408 ± 21

3.3.2.2.2. High-temperature annealing prior to phase transitions (HT+PT)

Thermal treatment at 473 K and 623 K reduced the number of as-deposited intercolumnar voids and more closed structures developed. In the annealed films, globular pores of various shapes and sizes unevenly scattered within the compact columnar structures are formed, Figure 3.7(b). These pores are remnants of the voids present in the as-deposited film that coalesce as a result of annealing-induced grain growth. From SEM analysis, it was found that the initial grain boundary voids started disappearing within 2 hr of annealing at 473 K.

From the cross-sectional view of TEM image in Figure 3.7(b), one can see that annealing at 623 K led to significant grain growth (50–200 nm wide), closing the voids in the Pd film on a bare SiO₂/Si. The red arrows in the figure point to spherical nanopores sized in the range 1–15 nm. In contrast, no such spherical nanopores can be observed within the compact morphology of Figure 3.7(c) for Pd-Ti-SiO₂/Si film after-HT+PT, and the average lateral grain size measured from BF-TEM images is in the range 25–65 nm. In Figures 3.8(d–i), SEM images show that dewetting or agglomeration starts at 473 K. Small holes are indicated by the white arrows in Figures 3.8(d–f), that develops further at 623 K temperature as shown in Figures 3.8(g–i). Pd on Ti layer showed the smallest holes size with quite a uniform size distribution. The differences in the number and shapes of the holes reflect the differences in film-substrate interaction [67]. In particular, the strong adhesion of the film to the Ti intermediate layer limits dewetting.

The evolved morphology of the Pd thin film after annealing strongly influenced phase transitions and the film stability during hydrogen uptake in addition to the effect of the intermediate layer. HT+PT experiments were conducted by annealing Pd films at 473 K or 632 K followed by subsequent phase transitions (PT). For Pd on a bare SiO₂/Si after annealing, phase transitions remained unaffected, but Pd layer was found buckle-delaminated at the end of HT+PT (lower right corner inset image Figure 3.8(j)). This behavior is similar to what was observed for series-1 Pd on a bare SiO₂/Si (Figure 3.5(e)) with compact morphology after a single hydrogen loading/deloading cycle at RT (section 4.3.2.1).

For Pd on Ti layer when annealed at 632 K, the XRD patterns in Figure 3.6(b) show that phase transition is completely suppressed, as seen in Figure 3.7(c), the film shows a compact morphology. In contrast, only partial suppression of phase transition occurred when annealed at 423 K. Similar observations were made earlier by Kim *et al.* [35] for Pd films with Ti intermediate layer, but the suppression of phase transition then occurred in as-deposited film

at RT. At the same time, Pd on PI layer after annealing at 473 K exhibits complete phase transitions without buckle-induced delamination.

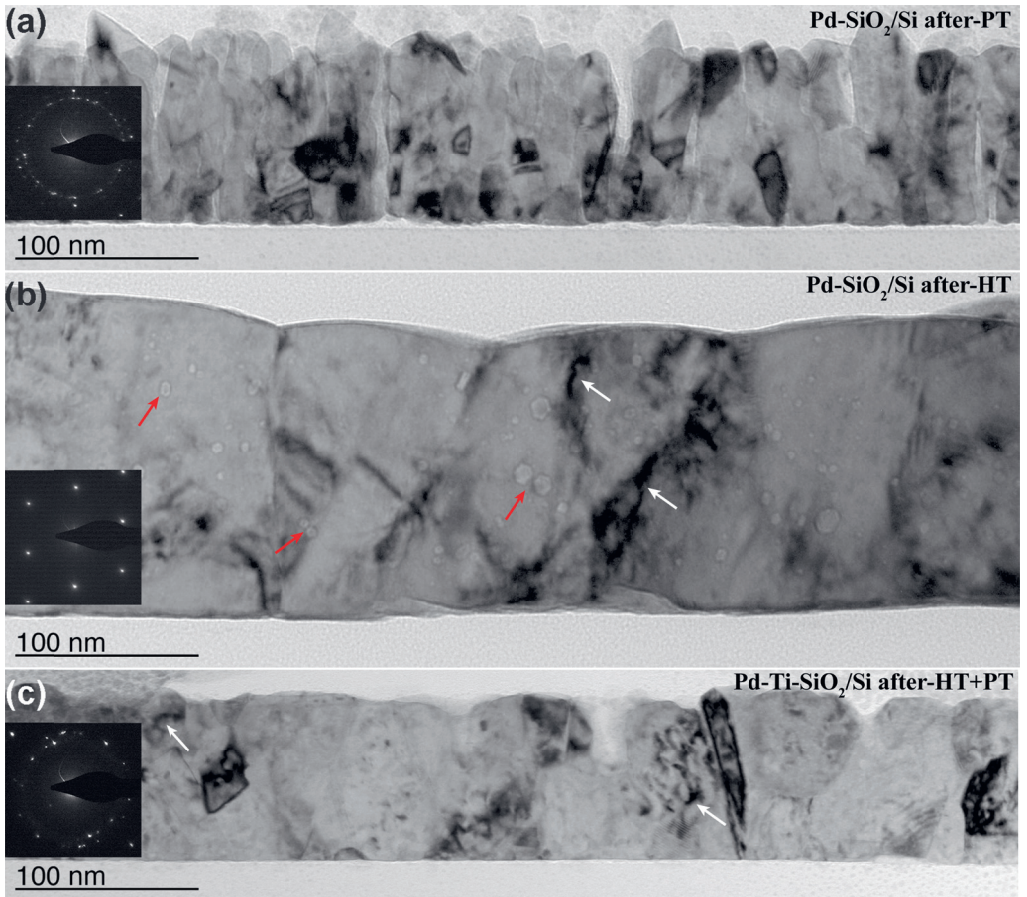


Figure 3.7 – The cross-sectional view of TEM bright-field images of series-2 Pd films. Pd-only expt.: (a) Pd-SiO₂/Si film after phase transitions (after-PT): film morphology and grain size remains unchanged. HT+PT expt.: (b) Pd-SiO₂/Si film after annealing at 623 K for 18 hr (after-HT): grain coalescence, loss of open columnar morphology and formation of spherical nanopores highlighted by red arrows, and (c) Pd-Ti-SiO₂/Si film after phase transitions on annealed (623 K for 18 h.) film (after-HT+PT): formation of compact morphology like as-deposited series-1 film, in such morphology $\alpha \leftrightarrow \beta$ phase transitions, are suppressed. White arrows are pointing to dislocation segments.

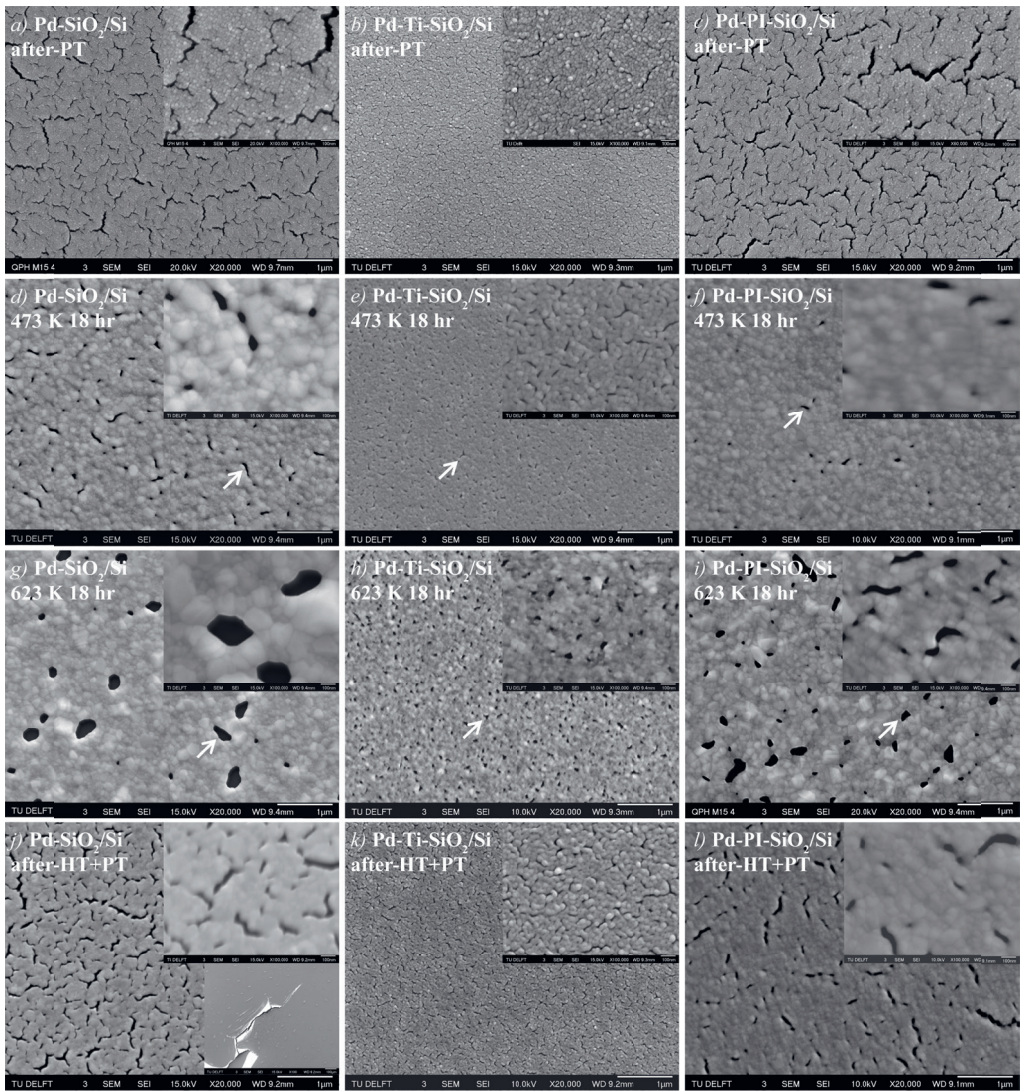


Figure 3.8 – SEM surface morphologies of series-2 Pd films. The large images (1 μm scale) and the insets (100 nm scale) exemplify the morphological evolution in Pd films. From left to right: Pd-SiO₂/Si, Pd-Ti-SiO₂/Si and Pd-PI-SiO₂/Si films. From top to bottom: after phase transitions (after-PT), after annealing film at 473 K for 18 h., after annealing film at 623 K for 18 h., and after phase transitions on annealed (473 K for 18 h.) film (after-HT+PT). The white arrows are showing annealing induced holes developed due to dewetting phenomena.

For Pd-SiO₂/Si and Pd-PI-SiO₂/Si films after-HT+PT (Figures 3.8(j&l)), the tapered voids and microcracks that during annealing disappeared and formed large globular pores, re-appeared as wide microcracks. These cracks indicate an effective mechanism for stress reduction locally. However, due to poor adhesion of Pd film on a SiO₂/Si substrate, a crack and buckle network propagates, leading to eventual film delamination. For Pd on PI layer (Figure 3.8(l)), however, no buckling occurs. Since we did not observe delamination after phase transitions even for compact morphology, we argue that the presence of the intermediate polymer layer helps in delocalizing the hydrogen-induced strain in the Pd film. Hence, a Pd film with a flexible PI intermediate layer exhibits free-standing film-like behavior besides being strongly clamped on a stiff SiO₂/Si substrate.

3.3.3. Microstructure from XRD line-broadening

The microstructural investigation was performed for the series-2 films only because the delamination occurring in series-1 films prevents practical application. Modified Williamson-Hall (Mod-WH) plots for the PT-only and HT+PT experiments were prepared by analyzing the line widths and applying formula (3.3) (see section 3.2.3.2) for all possible types of dislocations. On the basis of weighted least-square fitted straight lines using the estimated standard deviations in the breadth, it was concluded that randomly oriented pure screw dislocations of the {111}, $a/2\langle 110 \rangle$ slip system led to the best fits for all series-2 films studied.

The mod-WH plots in (Figure 3.9) show the analogies and differences in the microstructural behavior of the three film systems. In Figure 3.10(a) and Table 3.4, the values of crystallite size $\langle D \rangle$ and dislocation density ρ obtained from Figure 3.9 by a weighted least-square fitting of straight lines are shown. To visualize changes, in Figure 3.10(b), the $\langle D \rangle$ and ρ values are given relative to the average $\langle D \rangle$ and ρ values of the as-deposited state of the PT and HT+PT samples (taken from the same wafer).

The as-deposited films (as-dept.) of Pd-Ti-SiO₂/Si and Pd-PI-SiO₂/Si exhibit almost identical $\langle D \rangle$ and ρ , whereas for Pd-SiO₂/Si, the $\langle D \rangle$ is smaller and ρ is larger (Figure 3.10(a)). This implies that the intermediate layers reduce the formation of dislocations during deposition. This agrees with the idea that without clamping by an intermediate layer, free space around the columns can be used to generate dislocations and allow some crystallite growth (reduction of (e.g., mosaic) boundaries). And this agrees with the differences of the stresses (see Table

3.3). After PT (PT-only), an overall decrease of the slope is observed in Figure 3.9, for Pd-SiO₂/Si and Pd-PI-SiO₂/Si, implying a decrease in dislocation densities, whereas the slope increases for Pd-Ti-SiO₂/Si. This agrees with the idea that the clamping is more rigid for Ti so that the phase transition to the β -phase is accommodated by dislocations. For all series-2 films $\langle D \rangle$ hardly changes (Figures 3.10(a&b)).

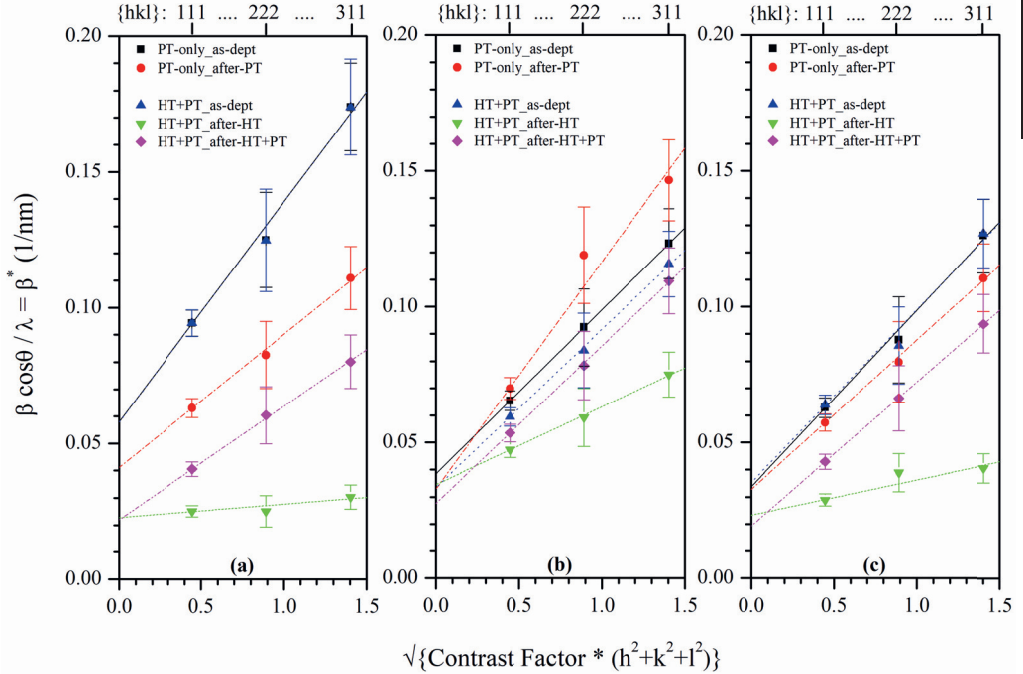


Figure 3.9 – The mod-WH plots for the series-2 films: (a) Pd-SiO₂/Si, (b) Pd-Ti-SiO₂/Si and (c) Pd-PI-SiO₂/Si showing β^*_{hkl} , versus C_{hkl} for randomly oriented screw dislocations with Burgers vector $a/2\langle 110 \rangle$ and glide plane $\{111\}$. Note that different specimens were used for PT-only and HT+PT experiments. The error bars shown are +3 and -3 times the standard deviation (see Eq. 3.3).

The trends observed in the mod-WH for the HT+PT experiments are similar for all specimens. The heat treatment reduces the slope and intercept, and the subsequent PT results in an increase in the slope. The high-temperature annealing (after-HT) induced grain growth leads to a considerable increase in $\langle D \rangle$, and reduction of dislocation densities. The subsequent PT slightly increase $\langle D \rangle$. The deformation due to the phase transition causes the dislocation density to increase (Figure 3.10(b))

Comparing the overall effects of both experiments, the $\langle D \rangle$ and ρ values for Pd-PI-SiO₂/Si are always between the results for Pd film without an intermediate layer and with a Ti intermediate layer (Figure 3.10(b)).

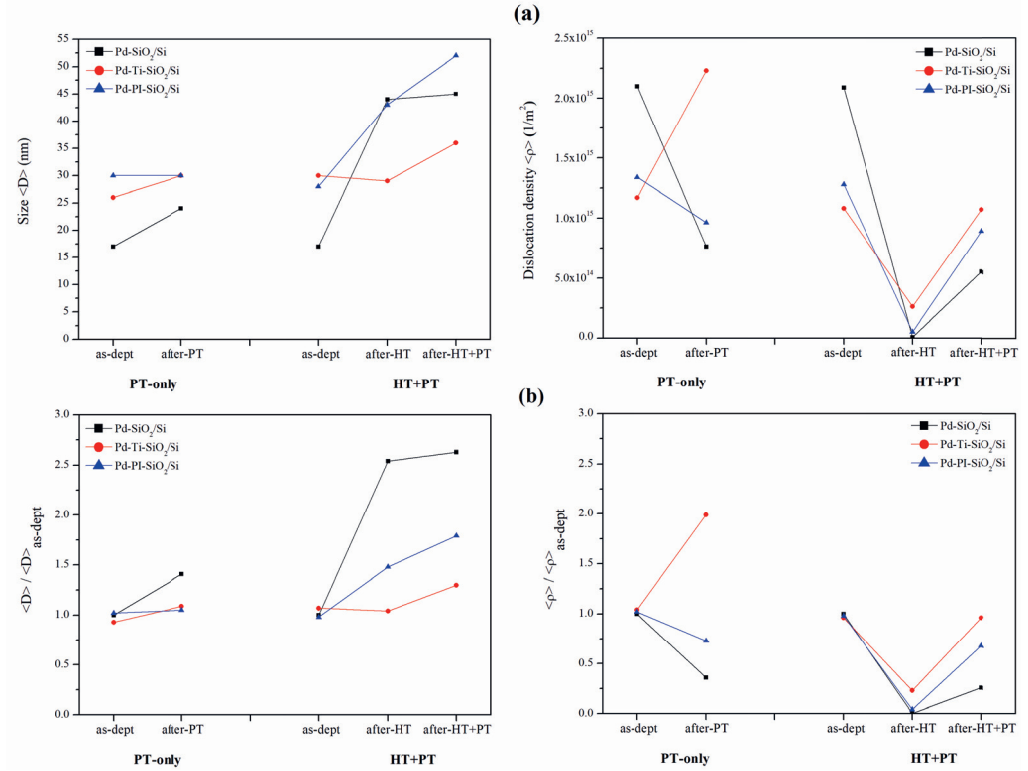


Figure 3.10 – (a) Plots with the absolute values of the crystallite size $\langle D \rangle$ (left) and the dislocation density ρ (right) for each of the three Pd film systems during PT-only and HT+PT experiments. Error bars that follow from the error bar shown in Figure 3.9 are not shown, but are 20 - 50% of the values shown and can be found in Appendix A, Table A2. (b) Plots with the $\langle D \rangle$ (left) and ρ (right) values relative to the average value obtained from the combination of as-deposited specimens used in PT-only and HT+PT experiments for each Pd film system.

3.3.4. Deformation mechanism

Whereas much of the mechanical behavior (i.e., buckling, delamination, and macro-stresses) of the three Pd film systems are explained on a μm scale as related to the TEM and SEM observations of series-2 (Figures 3.1(c–e) & Figure 3.7 and Figures 3.2(b–d) & Figure 3.8), the above section endorses microstructural interpretation ($\langle D \rangle$ and ρ) on a nm scale. The modified-WH plots indicate that in Pd films, microstrain is caused by the presence of dislocations. Colla *et al.* [68], using time-resolved HRTEM, demonstrated that the dislocation-mediated mechanism dictates the mechanical stability both during hydrogen loading (deformation) and deloading (relaxation) in textured Pd thin films.

3.3.4.1. Deformation during phase transitions (PT-only)

The dislocation densities obtained show a decrease after-PT for the Pd film on a bare SiO_2/Si and for Pd on PI layer as compared to the as-deposited state, whereas a Pd on Ti layer shows an increase in dislocation density, Figure 3.10(b). This shows that the decrease in microstrain (dislocation density) for Pd- SiO_2/Si could be caused by the added free surface generated by microcracks (see Figure 3.8(a)) propagating through voided grain boundaries.

The Pd on PI layer shows a small decrease in dislocation density after-PT (Figure 3.10(b)). Almost no microcracks were observed (Figure 3.8(c)), suggesting that the initial as-deposited defects would be confined at the interface of grain boundaries, hindering, relaxation and cracking, which suggests that a PI layer allows some of the strain relaxation inside the Pd crystallites by its flexibility. For Pd on Ti layer, an increase in strain and dislocation density after-PT is found (Table 3.3, Figure 3.9(b)). The loose columnar morphology of Pd film allowed phase transitions even on a rigid $\text{Ti-SiO}_2/\text{Si}$ substrate. Due to strong film to substrate bonding, cracks are not generated to relax hydrogen-induced stresses. The dislocations generated during loading (deformation) are blocked by the rigid substrate and dislocations pile-up against the film-substrate interface.

Thus, it appears possible that the increase of the bonding to the substrate by an intermediate layer of Ti or PI in our series-2 thin film systems, a microstructural stabilization mechanism occurs that implies some freedom to expand/contract during hydrogen loading/deloading so that some stress relaxation occurs along open grain boundaries. In this way, Pd films with an open morphology successfully restrict stresses from amplifying, and no noticeable structural deformation occurred.

3.3.3.2. Deformation in annealed Pd thin films (HT+PT)

Besides microstructural strengthening, the interaction at the film-substrate interface is also critical in attaining a stable metal thin film system [30]. For all series-2 films after annealing, the XRD profiles exhibit a reduction in line breadth (Figure 3.9); this change is associated with an increase in crystallite size and dislocation density decrease (Figure 3.10). This reduction is particularly substantial for Pd films on a bare SiO_2/Si and, to some extent, also for Pd on PI layer. In both cases, it is a reasonable assumption that the loss of defects occurs rapidly because of the added free surfaces along disconnected microcracks or nanopores, as seen in Figures 3.8(d&f) formed by grain agglomeration [69]. However, the lattice strain (Table 3.3) remained relatively high for Pd on Ti layer. In this case, the film-substrate interface plays a key role in the dislocation evolution. According to Freund [70] and Nix [71], the motion of threading dislocations is confined in the metallic film by a stiff substrate. A hard and strongly adhering Ti- SiO_2/Si substrate provided higher repulsion for dislocations at the interface than for film attached on a soft and flexible surface (PI) or a substrate with poor adherence (SiO_2/Si).

The densities of pre-existing dislocations that decreased during annealing were strongly increased upon subsequent phase transitions (after-HT+PT) for all series-2 films. The pre-annealed Pd film on a bare SiO_2/Si , release stress and defects by local film detachment due to low adhesion. Thus, here the increase in dislocation density cannot be explained as stated earlier by the dislocation escape theory at the buckle-delaminated free surface. The increase in dislocation density can be explained in terms of dislocation nucleation at the grain boundaries. For annealed Pd on Ti layer, partial suppression of phase transitions causes limited dislocation activity, resulting in the slight increase of the lattice strain reaching the initial value as observed in the as-deposited film (Figure 3.10(b)). In loaded Pd on PI layer, movement of dislocations at the Pd-film and PI-layer interface is the dominating stress relaxation pathway. Here, the interface plays a dominating role as the polyimide layer does not provide an obstacle for dislocations to escape the Pd film. The PI layer allowed Pd films to “breathe” during hydrogen absorption and desorption along with providing sufficient adhesion to the substrate. Here, the softer interface corresponds to the stronger thin film system.

3.4. Conclusion

In-situ X-ray diffraction study combined with SEM and TEM analysis on Pd thin films exposed to hydrogen showed that the interplay between film-microstructure and film-substrate interaction has a profound effect both on the response of hydrogen uptake and mode of damage. Stabilization against buckle-formation in compact morphology Pd film was achieved by adding an adhesive intermediate layer. It leads, however, to slow down (in the case of an intermediate layer) or partial suppression (in the case of a rigid layer) of phase transitions. The absence of buckle-delamination during Pd lattice expansion suggested that compressive stress-induced structural deformations are inhibited due to open columnar morphology of Pd film on a stiff SiO₂/Si substrate. But such Pd film under the influence of concurrent buckling and cracking delaminates above critical stress during high-temperature (623 K) H-loading due to weak adhesion. Inserting a flexible adhesive polyimide layer, maintained adhesion, and absorption/desorption properties at elevated temperatures.

X-ray line-broadening analysis, used for defect studies, indicated that all Pd films contain similar kinds of defects (dislocations) but differ by defect density concentration. The differences are mainly caused by differences in adherence to the substrate. A strongly adhering Ti-SiO₂/Si substrate provided higher repulsion for dislocations at the interface than for film attached on a flexible substrate (PI-SiO₂/Si) or on to a substrate with poor adherence (SiO₂/Si). Furthermore, the lowest concentration of the defects was found in the Pd-PI-SiO₂/Si film because the polymer substrate does not provide a strong obstacle for dislocations to escape the Pd film at the film-substrate interface. The Pd-PI interface acted as a perfect free surface for Pd film. Thus, a good combination of film microstructure and choice of intermediate layer allows upgrading Pd thin film systems mechanical strength.

3.5. References

- [1] Ball M, Weeda M. The hydrogen economy—vision or reality? *Int J Hydrogen Energy*. 2015;40:7903-19 DOI: <https://doi.org/10.1016/j.ijhydene.2015.04.032>.
- [2] Adams BD, Chen A. The role of palladium in a hydrogen economy. *Materials today*. 2011;14:282-9 DOI: [https://doi.org/10.1016/S1369-7021\(11\)70143-2](https://doi.org/10.1016/S1369-7021(11)70143-2).
- [3] Abe J, Popoola A, Ajenifuja E, Popoola O. Hydrogen energy, economy and storage: review and recommendation. *Int J Hydrogen Energy*. 2019;44:15072-86 DOI: [https://doi.org/10.1016/S1369-7021\(11\)70143-2](https://doi.org/10.1016/S1369-7021(11)70143-2).
- [4] Lischka M, Groß A. Hydrogen on palladium: A model system for the interaction of atoms and molecules with metal surfaces. *Recent Developments in Vacuum Science and Technology: Research Signpost*; 2003. p. 111-32.

- [5] Jewell LL, Davis BH. Review of absorption and adsorption in the hydrogen–palladium system. *Applied Catalysis A: General*. 2006;310:1-15 DOI: <https://doi.org/10.1016/j.apcata.2006.05.012>.
- [6] Manchester F, San-Martin A, Pitre J. The H-Pd (hydrogen-palladium) system. *Journal of phase equilibria*. 1994;15:62-83 DOI: <https://doi.org/10.1007/BF02667685>.
- [7] Flanagan TB, Oates W. The palladium-hydrogen system. *Annual Review of Materials Science*. 1991;21:269-304 DOI: <https://doi.org/10.1146/annurev.ms.21.080191.001413>.
- [8] Zhao M, Sloof WG, Böttger AJ. Modelling of surface segregation for palladium alloys in vacuum and gas environments. *Int J Hydrogen Energy*. 2018;43:2212-23 DOI: <https://doi.org/10.1016/j.ijhydene.2017.12.039>.
- [9] Burkhanov GS, Gorina NB, Kolchugina NB, Roshan NR, Slovetsky DI, Chistov EM. Palladium-based alloy membranes for separation of high purity hydrogen from hydrogen-containing gas mixtures. *Platinum Metals Review*. 2011;55:3-12 DOI: <https://doi.org/10.1595/147106711X540346>.
- [10] Baldi A, Dam B. Thin film metal hydrides for hydrogen storage applications. *Journal of Materials Chemistry*. 2011;21:4021-6 DOI: <https://doi.org/10.1039/C0JM03249B>.
- [11] Jang B, Cho S, Park C, Lee H, Song M-J, Lee W. Palladium nanogap-based H₂ sensors on a patterned elastomeric substrate using nanoimprint lithography. *Sensors and Actuators B: Chemical*. 2015;221:593-8 DOI: <https://doi.org/10.1016/j.snb.2015.06.142>.
- [12] Edwards PP, Kuznetsov VL, David WI, Brandon NP. Hydrogen and fuel cells: towards a sustainable energy future. *Energy policy*. 2008;36:4356-62 DOI: <https://doi.org/10.1016/j.enpol.2008.09.036>.
- [13] Okazaki J, Ikeda T, Tanaka DAP, Sato K, Suzuki TM, Mizukami F. An investigation of thermal stability of thin palladium–silver alloy membranes for high temperature hydrogen separation. *Journal of membrane science*. 2011;366:212-9 DOI: <https://doi.org/10.1016/j.memsci.2010.10.011>.
- [14] Al-Mufachi N, Rees N, Steinberger-Wilkens R. Hydrogen selective membranes: a review of palladium-based dense metal membranes. *Renewable and Sustainable Energy Reviews*. 2015;47:540-51 DOI: <https://doi.org/10.1016/j.rser.2015.03.026>.
- [15] Rusman N, Dahari M. A review on the current progress of metal hydrides material for solid-state hydrogen storage applications. *Int J Hydrogen Energy*. 2016;41:12108-26 DOI: <https://doi.org/10.1016/j.ijhydene.2016.05.244>.
- [16] Rahimpour M, Samimi F, Babapoor A, Tohidian T, Mohebi S. Palladium membranes applications in reaction systems for hydrogen separation and purification: A review. *Chemical Engineering and Processing: Process Intensification*. 2017;121:24-49 DOI: <https://doi.org/10.1016/j.ccep.2017.07.021>.
- [17] Fernandez E, Helmi A, Medrano J, Coenen K, Arratibel A, Melendez J, et al. Palladium based membranes and membrane reactors for hydrogen production and purification: An overview of research activities at Tecnalia and TU/e. *Int J Hydrogen Energy*. 2017;42:13763-76 DOI: <https://doi.org/10.1016/j.ijhydene.2017.03.067>.
- [18] Pundt A, Kirchheim R. Hydrogen in metals: microstructural aspects. *Annu Rev Mater Res*. 2006;36:555-608 DOI: <https://doi.org/10.1146/annurev.matsci.36.090804.094451>.
- [19] Kirchheim R, Mütschele T, Kieninger W, Gleiter H, Birringer R, Koble T. Hydrogen in amorphous and nanocrystalline metals. *Materials science and engineering*. 1988;99:457-62 DOI: [https://doi.org/10.1016/0025-5416\(88\)90377-1](https://doi.org/10.1016/0025-5416(88)90377-1).
- [20] Iwaoka H, Arita M, Horita Z. Hydrogen diffusion in ultrafine-grained palladium: Roles of dislocations and grain boundaries. *Acta Materialia*. 2016;107:168-77 DOI: <https://doi.org/10.1016/j.actamat.2016.01.069>.
- [21] Ulvestad A, Yau A. The self-healing of defects induced by the hydriding phase transformation in palladium nanoparticles. *Nature communications*. 2017;8:1-6 DOI: <https://doi.org/10.1038/s41467-017-01548-7>.

- [22] Narayan TC, Hayee F, Baldi A, Koh AL, Sinclair R, Dionne JA. Direct visualization of hydrogen absorption dynamics in individual palladium nanoparticles. *Nature communications*. 2017;8:14020 DOI: <https://doi.org/10.1038/ncomms14020>.
- [23] Amin-Ahmadi B, Connétable D, Fivel M, Tanguy D, Delmelle R, Turner S, et al. Dislocation/hydrogen interaction mechanisms in hydrided nanocrystalline palladium films. *Acta Materialia*. 2016;111:253-61 DOI: <https://doi.org/10.1016/j.actamat.2016.03.054>.
- [24] Hamm M, Burlaka V, Wagner S, Pundt A. Achieving reversibility of ultra-high mechanical stress by hydrogen loading of thin films. *Applied Physics Letters*. 2015;106:243108 DOI: <https://doi.org/10.1063/1.4922285>.
- [25] Pedersen TL, Liesch C, Salanga C, Eleftheriadis T, Weis H, Wuttig M. Hydrogen-induced changes of mechanical stress and optical transmission in thin Pd films. *Thin Solid Films*. 2004;458:299-303 DOI: <https://doi.org/10.1016/j.tsf.2003.12.040>.
- [26] Wagner S, Pundt A. Quasi-thermodynamic model on hydride formation in palladium-hydrogen thin films: Impact of elastic and microstructural constraints. *Int J Hydrogen Energy*. 2016;41:2727-38 DOI: <https://doi.org/10.1016/j.ijhydene.2015.11.063>.
- [27] Wagner S, Kramer T, Uchida H, Dobron P, Cizek J, Pundt A. Mechanical stress and stress release channels in 10–350 nm palladium hydrogen thin films with different microstructures. *Acta Materialia*. 2016;114:116-25 DOI: <https://doi.org/10.1016/j.actamat.2016.05.023>.
- [28] Pivak Y, Schreuders H, Slaman M, Griessen R, Dam B. Thermodynamics, stress release and hysteresis behavior in highly adhesive Pd–H films. *Int J Hydrogen Energy*. 2011;36:4056-67 DOI: <https://doi.org/10.1016/j.ijhydene.2010.12.063>.
- [29] Pundt A, Nikitin E, Pekarski P, Kirchheim R. Adhesion energy between metal films and polymers obtained by studying buckling induced by hydrogen. *Acta materialia*. 2004;52:1579-87 DOI: <https://doi.org/10.1016/j.actamat.2003.12.003>.
- [30] Wong M-f, Duan G, Wan K-t. Adhesion–delamination mechanics of a prestressed circular film adhered onto a rigid substrate. *The Journal of Adhesion*. 2007;83:67-83 DOI: <https://doi.org/10.1080/00218460601102878>.
- [31] Gremaud R, Gonzalez-Silveira M, Pivak Y, De Man S, Slaman M, Schreuders H, et al. Hydrogenography of PdHx thin films: Influence of H-induced stress relaxation processes. *Acta Materialia*. 2009;57:1209-19 DOI: <https://doi.org/10.1016/j.actamat.2008.11.016>.
- [32] Harumoto T, Shi J, Nakamura Y. Effects of stress and defects on hydrogenation and magnetic properties in (111) fiber-textured palladium cobalt alloy films. *Int J Hydrogen Energy*. 2020 DOI: <https://doi.org/10.1016/j.ijhydene.2020.02.118>.
- [33] Čížek J, Melikhova O, Vlček M, Lukáč F, Vlach M, Procházka I, et al. Hydrogen-induced microstructural changes of Pd films. *Int J Hydrogen Energy*. 2013;38:12115-25 DOI: <http://dx.doi.org/10.1016/j.ijhydene.2013.03.096>.
- [34] Delmelle R, Amin-Ahmadi B, Sinnaeve M, Idrissi H, Pardoën T, Schryvers D, et al. Effect of structural defects on the hydriding kinetics of nanocrystalline Pd thin films. *Int J Hydrogen Energy*. 2015;40:7335-47 DOI: <https://doi.org/10.1016/j.ijhydene.2015.04.017>.
- [35] Kim KR, Noh J-S, Lee JM, Kim YJ, Lee W. Suppression of phase transitions in Pd thin films by insertion of a Ti buffer layer. *Journal of Materials Science*. 2010;46:1597-601 DOI: <https://doi.org/10.1007/s10853-010-4970-x>.
- [36] Matsumoto I, Sakaki K, Nakamura Y, Akiba E. In situ atomic force microscopy observation of hydrogen absorption/desorption by Palladium thin film. *Appl Surf Sci*. 2011;258:1456-9 DOI: DOI 10.1016/j.apsusc.2011.09.103.
- [37] Vlček M, Lukáč F, Vlach M, Wagner S, Uchida H, Baecht C, et al. Influence of microstructure and mechanical stress on behavior of hydrogen in 500nm Pd films. *Journal of Alloys and Compounds*. 2015;645:S446-S9 DOI: <https://doi.org/10.1016/j.jallcom.2014.12.086>.

- [38] Windischmann H. Intrinsic stress in sputter-deposited thin films. *Critical Reviews in Solid State and Material Sciences*. 1992;17:547-96 DOI: <https://doi.org/10.1080/10408439208244586>.
- [39] Verma N, Böttger AJ. Stress development and adhesion in hydrogenated nano-columnar Pd and Pd/Ti ultra-thin films. *Advanced Materials Research*. 2014;996 DOI: <https://doi.org/10.4028/www.scientific.net/AMR.996.872>.
- [40] Verma N, Krishnamurthy G, Tichelaar FD, Böttger AJ. Controlling morphology and texture of sputter-deposited Pd films by tuning the surface topography of the (Ti) adhesive layer. *Surface and Coatings Technology*. 2019;359:24-34 DOI: <https://doi.org/10.1016/j.surfcoat.2018.12.053>.
- [41] Delhez R, De Keijser TH, Mittemeijer E. Determination of crystallite size and lattice distortions through X-ray diffraction line profile analysis. *Fresenius' Zeitschrift für analytische Chemie*. 1982;312:1-16 DOI: <https://doi.org/10.1007/BF00482725>.
- [42] Scardi P, Leoni M, Delhez R. Line broadening analysis using integral breadth methods: a critical review. *Journal of Applied Crystallography*. 2004;37:381-90 DOI: <https://doi.org/10.1107/S0021889804004583>.
- [43] DIFFRAC.EVA. Bruker AXS Software, Karlsruhe, Germany; 2001 DOI: <https://www.bruker.com/>.
- [44] Welzel U, Leoni M. Use of polycapillary X-ray lenses in the X-ray diffraction measurement of texture. *Journal of applied crystallography*. 2002;35:196-206 DOI: <https://doi.org/10.1107/S0021889802000481>.
- [45] Fouet J, Richard MI, Mocuta C, Guichet C, Thomas O. In situ combined synchrotron X-ray diffraction and wafer curvature measurements during formation of thin palladium suicide film on Si(001) and Si (111). *Nucl Instrum Meth B*. 2012;284:74-7 DOI: DOI 10.1016/j.nimb.2011.07.019.
- [46] Hauk V. Structural and residual stress analysis by nondestructive methods: Evaluation-Application-Assessment: Elsevier; 1997.
- [47] Hsu D, Leisure R. Elastic constants of palladium and β -phase palladium hydride between 4 and 300 K. *Physical Review B*. 1979;20:1339-44 DOI: <https://doi.org/10.1103/PhysRevB.20.1339>.
- [48] Welzel U, Mittemeijer EJ. Diffraction stress analysis of macroscopically elastically anisotropic specimens: On the concepts of diffraction elastic constants and stress factors. *Journal of Applied Physics*. 2003;93:9001-11 DOI: <https://doi.org/10.1063/1.1569662>.
- [49] Welzel U, Mittemeijer EJ. Applicability of the crystallite group method to fibre textured specimens. *Materials Science Forum: Trans Tech Publ*; 2004. p. 131-6 DOI: <https://doi.org/10.4028/www.scientific.net/MSF.443-444.131>.
- [50] Igor Pro, WaveMetrics. Lake Oswego, Oregon, USA; 2011 DOI: <https://www.wavemetrics.com/>.
- [51] SRM660a; lanthanum hexaboride powder line position and line shape standard for powder diffraction. Certificate, National Institute of Standards and Technology, US Department of Commerce: Gaithersburg, MD, USA; 2000 DOI: <https://www.nist.gov/srm>.
- [52] Velterop L, Delhez R, Keijser THd, Mittemeijer E, Reefman D. X-ray diffraction analysis of stacking and twin faults in fcc metals: a revision and allowance for texture and non-uniform fault probabilities. *Journal of applied crystallography*. 2000;33:296-306 DOI: <https://doi.org/10.1107/S0021889800000133>.
- [53] Williamson G, Hall W. X-ray line broadening from fcc aluminium and wolfram. *Acta metallurgica*. 1953;1:22-31 DOI: [https://doi.org/10.1016/0001-6160\(53\)90006-6](https://doi.org/10.1016/0001-6160(53)90006-6).
- [54] Ungár T, Dragomir I, Révész Á, Borbély A. The contrast factors of dislocations in cubic crystals: the dislocation model of strain anisotropy in practice. *Journal of applied crystallography*. 1999;32:992-1002 DOI: <https://doi.org/10.1107/S0021889899009334>.

- [55] Gubicza J. X-ray line profile analysis in materials science. Hershey, Pennsylvania :: Engineering Science Reference; 2014 DOI: <http://doi:10.4018/978-1-4666-5852-3>.
- [56] Petrov I, Barna P, Hultman L, Greene J. Microstructural evolution during film growth. *Journal of Vacuum Science & Technology A*. 2003;21:S117-S28 DOI: <https://doi.org/10.1116/1.1601610>.
- [57] Thornton JA. Influence of apparatus geometry and deposition conditions on the structure and topography of thick sputtered coatings. *Journal of Vacuum Science & Technology*. 1974;11:666-70 DOI: <https://doi.org/10.1116/1.1312732>.
- [58] Jones T, Hall K. The melting point of palladium and its dependence on oxygen. *Metrologia*. 1979;15:161 DOI: <https://doi.org/10.1088/0026-1394/15/3/007>.
- [59] Smith DL. *Thin Film Deposition: Principles and Practice*. McGraw-Hill Inc. 1995 DOI: <https://doi.org/10.1063/1.2807590>.
- [60] Bai P, McDonald JF, Lu TM, Costa MJ. Effect of substrate surface roughness on the columnar growth of Cu films. *J Vac Sci Technol A*. 1991;9:2113-7 DOI: <http://dx.doi.org/10.1116/1.577235>.
- [61] Whitacre J, Rek Z, Bilello J, Yalisove S. Surface roughness and in-plane texturing in sputtered thin films. *Journal of applied physics*. 1998;84:1346-53 DOI: <https://doi.org/10.1063/1.368204>.
- [62] Thornton JA, Hoffman D. Stress-related effects in thin films. *Thin solid films*. 1989;171:5-31 DOI: [https://doi.org/10.1016/0040-6090\(89\)90030-8](https://doi.org/10.1016/0040-6090(89)90030-8).
- [63] Ohring M. *Mechanical Properties of Thin Films*. Materials science of thin films: Academic press; 2001. p. 403-49.
- [64] Lu N, Suo Z, Vlassak JJ. The effect of film thickness on the failure strain of polymer-supported metal films. *Acta Materialia*. 2010;58:1679-87 DOI: <https://doi.org/10.1016/j.actamat.2009.11.010>.
- [65] Leterrier Y, Medico L, Demarco F, Månson J-A, Betz U, Olsson MK, et al. Mechanical integrity of transparent conductive oxide films for flexible polymer-based displays. *Thin Solid Films*. 2004;460:156-66 DOI: <https://doi.org/10.1016/j.tsf.2004.01.052>.
- [66] Li T, Huang Z, Xi Z, Lacour SP, Wagner S, Suo Z. Delocalizing strain in a thin metal film on a polymer substrate. *Mechanics of Materials*. 2005;37:261-73 DOI: <https://doi.org/10.1016/j.mechmat.2004.02.002>.
- [67] Thompson CV. Solid-state dewetting of thin films. *Annual Review of Materials Research*. 2012;42:399-434.
- [68] Colla M-S, Amin-Ahmadi B, Idrissi H, Malet L, Godet S, Raskin J-P, et al. Dislocation-mediated relaxation in nanograin columnar palladium films revealed by on-chip time-resolved HRTEM testing. *Nature communications*. 2015;6 DOI: <https://doi.org/10.1038/ncomms6922>.
- [69] Freund L, Jonsdottir F. Instability of a biaxially stressed thin film on a substrate due to material diffusion over its free surface. *Journal of the Mechanics and Physics of Solids*. 1993;41:1245-64 DOI: [https://doi.org/10.1016/0022-5096\(93\)90092-T](https://doi.org/10.1016/0022-5096(93)90092-T).
- [70] Freund L. The stability of a dislocation threading a strained layer on a substrate. *Journal of Applied Mechanics*. 1987;54:553-7 DOI: <https://doi.org/10.1115/1.3173068>.
- [71] Nix WD. Mechanical properties of thin films. *Metallurgical transactions A*. 1989;20:2217-45 DOI: <https://doi.org/10.1007/BF02666659>.

4

Stress development in hydrogenated nano-columnar Pd and Pd on Ti thin films³

In this chapter, the stress development upon hydrogenation of about 100 nm thick palladium (Pd) films on thermally oxidized silicon wafers with and without an intermediate Ti layer is studied. Stress developed was investigated by *in-situ* XRD in H₂/N₂ (hydrogenation) and N₂ (dehydrogenation) gas at room temperature. The method adopted to measure residual stress involves specimen omega- (ω) and psi- (ψ) tilting on two different diffractometer geometries (focusing and parallel). For the stress analysis, the presence of intrinsic elastic anisotropy of the film was considered. Upon hydrogenation α -Pd transformation to β -PdH_{0.6} occurs and because of the constrained in-plane expansion a large compressive stress develops. Scanning electron microscopy shows that Pd film with a Ti intermediate layer adheres better to the substrate during hydrogen cycling, whereas, pure Pd film starts cracking and buckling.

³ This chapter is based on a scientific paper:

N. Verma, A.J. Böttger, *Stress development and adhesion in hydrogenated nano-columnar Pd and Pd/Ti ultra-thin films*, Advanced Materials Research, vol. 996, pp. 872-877, 2014.

4.1. Introduction

Thin Pd films are of interest as hydrogen separation membranes [1], but high mechanical stresses between a film and its substrate often lead to film detachment and subsequent failure in thin films [2]. By hydrogen loading of Pd thin film that is clamped to a substrate, high in-plane stresses up to several MPa develop due to volume change [3]. These stresses are high enough to detach films from their substrate, rendering such films of low industrial use. The exact knowledge of the magnitude of the residual stress state is of great technological importance because stresses can be detrimental for the performance of thin film. The technique commonly used for these measurements include X-ray diffraction (XRD) [4]. Particularly when using focusing geometry for the XRD stress analysis it is important to be aware of line broadening and line shift, as the method is sensitive to alignment errors, unlike parallel-beam geometry. Hence corrections are needed for reliable stress results [5]. For stress measurement, diffraction lines of different hkl reflections are recorded at various sample tilt angles and the components of the mechanical stresses are deduced using $\sin^2\psi$ method employing suitable X-ray elastic constants (XEC's) [4]. For thin films, which are (intrinsically) elastically anisotropic, the XECs differ for various hkl reflections and are dependent on single-crystal elastic constants, grain-interaction model and on the crystallographic texture [6-8]. In this chapter, *in-situ* and *ex-situ* (de)hydrogenation stress analysis of Pd thin films is performed in order to expand the application of nano-columnar Pd thin film to H₂ gas purification/separation and sensing.

4.2. Experimental

4.2.1. Pd thin film preparation

The nanostructured Pd thin films with and without Ti intermediate layer were prepared by magnetron sputtering. Films were sputtered on an oxidized Si single crystal wafer substrate rotating at a uniform rate during the deposition. Sputtering was performed at room temperature (RT) in Volmer-Weber growth mode to achieve loose columnar morphology. The thicknesses of the Pd layer were set to ~100 nm and ~3 nm for Ti layer as estimated by weighing and later confirmed by transmission electron microscopy (TEM) while examining film morphology.

4.2.2. X-ray diffraction measurement

X-ray diffraction (XRD) measurements were carried out using two types of XRD systems (i) Bruker-AXS D5005 diffractometer in Bragg-Brentano focusing geometry ($\text{CuK}\alpha$), equipped with closed MRI High Temperature chamber; further called HT-XRD system for *in-situ* measurements, and (ii) Bruker D8 diffractometer in parallel beam geometry ($\text{CoK}\alpha$), equipped with Huber $\frac{1}{4}$ circle Eulerian Cradle and a graphite monochromator in the diffracted beam; further called PSI-XRD system for *ex-situ* measurements.

Hydrogen cycling of Pd ($\text{Pd-SiO}_2/\text{Si}$) and Pd on Ti ($\text{Pd-Ti-SiO}_2/\text{Si}$) thin films was done during slow 20 hydrogen loading/deloading cycles (20-L/D) in closed MRI HT chamber, at RT in 1 atm of H_2N_2 (loading) and N_2 (deloading) gas atmosphere respectively. Continuous short 2 min scans were made until complete L/D was achieved at each cycle. Change in Pd thin film surface morphology after cycling was characterized using scanning electron microscopy (SEM).

4.2.2.1. *In-situ* ω -tilt stress measurement during Pd phase transformation

In-situ stress measurement was done on HT-XRD system, for loaded and deloaded film specimens. During 20-L/D cycles; stress developed in Pd and Pd on Ti layer films was measured after 1st, 5th, 10th, 15th and 20th loading and deloading cycles on a single specimen. In-plane (de)-hydrogenation stresses in Pd thin films, were measured by applying ω -tilt for the Pd- α and Pd- β - {3314 and {420} reflections. The chosen high angle reflections for *in-situ* stress gives low intensity, broad and overlapped peaks, but were preferred over low-angle reflections because shift in diffraction lines due to imposed stress is more prominent at higher diffraction angles. Positive ω -tilt was applied in the range of 0°- 45° in step mode ($\sin^2\psi$ 0 - 0.5). The defocusing correction was determined using stress-free Palladium powder, for which the stress-free state has been confirmed on the PSI-XRD system. Due to the alignment errors in the focusing geometry pseudo-stresses were observed even in stress-free Palladium powder (AlFa-D24F20), for which the stress-free state was checked with ψ -tilting on PSI-XRD system. For collecting reliable XRD data, the peak profile statistical accuracy was improved by using adequate irradiated specimen volume and increasing counting time. The total measurement time for each stress scan ranged from 22 to 24 hours for weak Pd {331} & {420} reflections.

4.2.2.2. *Ex-situ* ψ -tilt stress measurement after hydrogen cycling experiment

Pd and Pd on Ti layer specimens after hydrogen L/D cycling experiments on HT-XRD system were scanned for *ex-situ* stress measurement on the PSI-XRD system. PSI-XRD system with parallel beam optics show no sensitivity for alignment errors and therefore, is preferred over TT-XRD system for residual stress measurement. Step scans were performed over a 2θ -range of 96° - 104° for the Pd- $\{311\}$ reflection. Data was collected at six tilt angles for a fixed sample orientation (at $\phi = 90^\circ$). The tilt angle, ψ , is the angle between the normal of the specimen and the normal of the diffracted planes and ranged from 0° to 45° ($\sin^2\psi$ 0 - 0.50, steps of 0.10).

4.2.3. Stress analysis

Stress analysis was performed using the $\sin^2\psi$ technique. All the data evaluation was done with the programs Bruker EVA and PANalytical X'Pert Stress Plus [9]. Diffraction patterns from ω -tilt measurements were evaluated by fitting with different peak fitting methods: Parabola, Profile shape function, Centered Center of gravity and mix fit, in order to obtain accurate peak positions from low intensity, asymmetry and poor profiles. Absorption/transparency correction, background subtraction and $K\alpha_2$ -stripping, as intensity corrections were applied to the measured data. The possible alignment corrections were made using stress-free Pd powder, on the raw diffraction data of ω -tilt and ψ -tilt measurements for the stress analysis of (de)-hydrogenated Pd thin films. The lattice spacing d_ψ was then calculated and plotted as a function of $\sin^2\psi$ to deduce in-plane stress in Pd thin films.

4.3. Results and Discussion

Based on the Pd thin film deposition parameters and from TEM bright field image (Figure 4.1(a)), Pd thin films show a classic zone-3 morphology characterized by loosely held columnar grains, which extend through the film thickness. XRD patterns revealed that films have Pd- $\{111\}$ preferred orientation. After 20 hydrogen L/D cycles, Pd-SiO₂/Si film was found buckled delaminated, starting from edges and growing towards the center (Figure 4.1(b)), whereas, Pd-Ti-SiO₂/Si film remained intact as in as-sputtered condition (Figure 4.1(c))

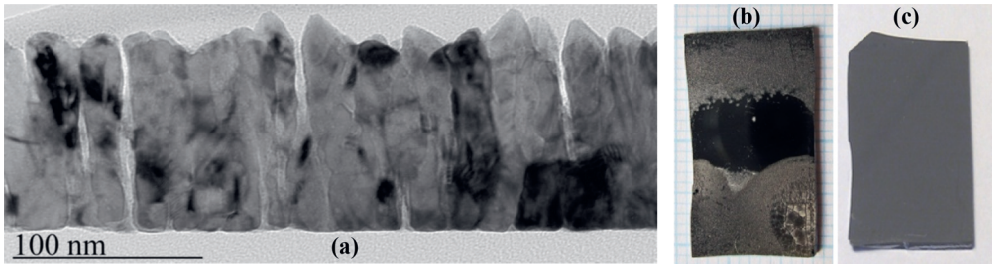


Figure 4.1 – (a) TEM bright field image of as-sputtered Pd-SiO₂/Si film. Camera picture of specimens (b) Pd-SiO₂/Si and (c) Pd-Ti-SiO₂/Si after 20 hydrogen L/D cycles. Pd film has buckle delaminated edges with a small flat cracked area in the center and Pd on Ti film remained in as-sputtered condition even after 20 H-L/D cycles.

4.3.1. Stress analysis: Sin²ψ method

The determination of compressive and tensile stresses during loading and deloading cycles and strain-free lattice parameters (d_0 and $\sin^2\psi_0$) has been carried out using the traditional $\sin^2\psi$ -method [10]. This method in principle allows the full assessment of the mechanical stress state of a sample from the spacing of one or more families of lattice hkl planes measured. In-plane stress for the case of planar, rotationally symmetric biaxial state of stress ($\sigma_{11} = \sigma_{22} = \sigma$), was calculated from Eq. 4.1 [4, 7].

$$\varepsilon_{\psi}^{hkl} = d_{\psi}^{hkl} - d_0^{hkl} / d_0^{hkl}, \quad \varepsilon_{\psi}^{hkl} = \left(2S_1^{hkl} + \frac{1}{2S_2^{hkl} \sin^2\psi} \right) \sigma \quad (4.1)$$

S_1^{hkl} and $\frac{1}{2}S_2^{hkl}$ are the so-called X-ray elastic constants (XECs). For the stress analysis involving particular hkl reflections, the measured lattice strain is not a direct measure of the average mechanical strain of all crystallites, therefore, x-ray diffraction data are highly susceptible to the elastic anisotropy. This can be taken into account by using the grain-interaction models that describe the distribution of stresses and strains over the crystallographically differently oriented crystallites in the specimen [7, 11]. The most widely applied traditional grain-interaction models: Voigt [12], Reuss [13] and Hill-weighted average [14], , can be used to calculate XECs from single-crystal (known) elastic constants. Elastic constants of Pd change with H content in the lattice, which also results in change of XECs of Pd loaded with hydrogen. In the Table 4.1 are XECs of Pd and PdH_{0.6}, derived from PANalytical X'Pert Stress Plus software, as calculated according to three different grain-

interaction models, from single-crystal elastic constants of Pd and PdH_{0.6} at 300 K [15]. For the Pd polycrystalline film lattice strain has been calculated in Figure 4.2 for planar, rotationally symmetric state of 100 MPa tensile stress ($\sigma_1 \equiv \langle \sigma_{11} \rangle = \langle \sigma_{22} \rangle$) and presented as function of $\sin^2 \psi$ for various reflections, applying above three grain-interaction models.

Table 4.1 – *X-ray elastic constants (XECs) for grain-interaction models derived from X'Pert Stress program, using Pd and PdH_{0.6} single-crystal elastic constants taken from the reference [15].*

Pd reflections { <i>hkl</i> }	Voigt		Reuss		Hill-weighted	
	S_1^{hkl}	$\frac{1}{2}S_2^{hkl}$	S_1^{hkl}	$\frac{1}{2}S_2^{hkl}$	S_1^{hkl}	$\frac{1}{2}S_2^{hkl}$
{111}/{222}	−2.57	9.46	−1.75	7.02	8.24	−2.16
{200}/{400}	−2.57	9.46	−6.00	19.74	14.60	−4.28
{311}	−2.57	9.46	−4.00	13.75	11.60	−3.28
{331}	−2.57	9.46	−2.51	9.27	9.36	−2.54
{420}	−2.57	9.46	−3.96	13.63	11.54	−3.26

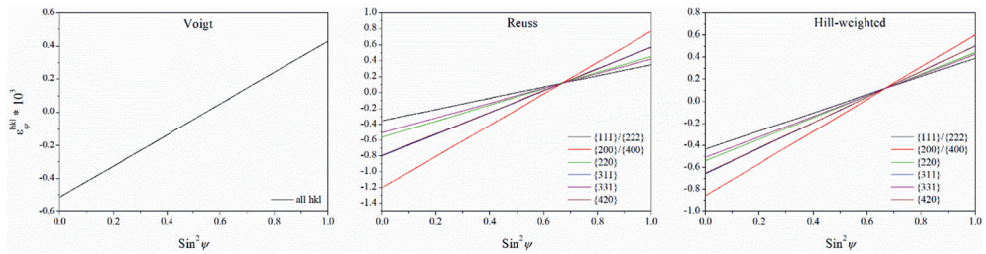


Figure 4.2 – *Calculated lattice strain presented as function of $\sin^2 \psi$ for various reflections of Pd thin film subjected to a plane, rotationally symmetric state of stress (100 MPa) for three grain-interaction models: i) Voigt, ii) Reuss and Hill-weighted average.*

To describe the physical reality the average of two extreme grain interaction contribute to the effective grain interaction, which can be expressed by the interaction parameters, $\langle w \rangle$. The effective grain interaction can be expressed by the interaction parameters for the two principal directions; $w_{\parallel}=0$ for the Reuss, $w_{\parallel}=1$ for the Voigt, $w_{\perp}=0$ for the Reuss, and $w_{\perp}=1$ for the Voigt [16]. The average values $\langle w_{\parallel} \rangle$ and $\langle w_{\perp} \rangle$ equal to 0.5 describing the effective grain interaction in the two principal directions. For a Pd thin film clamped onto a substrate, only in-plane grain interactions are expected, as compressive forces due to the hydrogenation

results in a biaxial state of stress exerted by the substrate. The surface of the film is free, so there is no stress built-up in the perpendicular direction. Hence, the (de)-hydrogenation stresses in these Pd thin films were estimated by using Hill's weighted average grain-interaction model ($w = 0.5$), which is the arithmetic average of x-ray and macroscopic elastic constants as calculated with the Reuss and the Voigt grain-interaction model. The observed pseudo-stress in a stress-free reference Pd powder, as a result of the tilt-dependent peak shifts originating from defocusing and specimen displacement errors, from ω -tilt measurements, are listed in Table 4.2.

Table 4.2 – Pseudo-stress measured in stress-free Pd powder by ω -tilt and ψ -tilt stress methods. For Pd- {311}, {331} and {420} reflections peak positions are deduced by four different peak fitting methods.

Pseudo-stress in stress-free Pd powder				
ω -tilt Stress (MPa)	Centered Center of Gravity	Parabola	Profile shape function	Mixed
Pd-{331}	-31.9 ± 5.7	-36.2 ± 4.6	-30.9 ± 5.0	-33.3 ± 2.7
Pd-{420}	-13.8 ± 4.9	-19.2 ± 4.3	-14.6 ± 2.0	-13.9 ± 4.7
ψ -tilt Stress (MPa)				
Pd-{311}	-0.9 ± 0.9	-0.1 ± 1.5	-1.2 ± 0.9	-1.3 ± 0.7

For reliable stress results it is very important that systematic errors are absent. But with TT-XRD system, single axis goniometer, the chances of systematic errors like specimen displacement and incident beam misalignment are quite high, especially while providing virtual tilt to the specimen during ω -tilt stress measurement. Various hydrogen L/D experiments with similar setups were performed to test applicability of ω -tilt method for reliable *in-situ* stress results. *In-situ* deloading stresses measured during four experiments using every time different Pd thin film specimens are collected in Figure 4.3, showing 1, 5, 10, and 20 -L/D cycles performed at RT; for comparison peak positions were determined with the Centered Center of Gravity (Figure 4.3(a)) and the Parabola (Figure 4.3(b)) methods. For both fitting methods only a fraction of the upper portion of the peak was included, so as to avoid the region of overlap between the Pd {331} and {420} peaks. However, the peak

position will vary as a result of defocusing since the tilt-angle is changing during the course of stress measurement. After subtracting the pseudo-stress (Table 4.2) from the measured stress, the possible defocusing error was corrected and the calculated stress for different L/D experiments lies within the error limits (corresponding to the counting-statistical error resulting from peak fitting) (Figure 4.3). For a satisfactory conclusion about the measured ω -stress results, *ex-situ* residual stress measurements were performed using the PSI-XRD with parallel beam geometry. Results from both the methods are compared and discussed further.

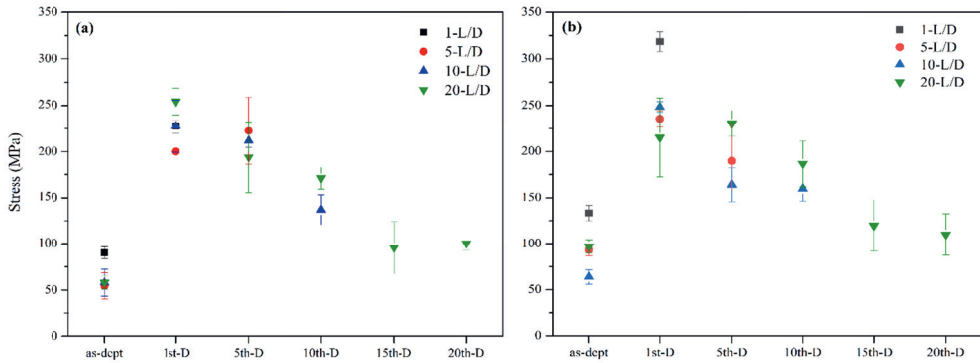


Figure 4.3 – Residual stress vs number of deloading cycles. Peak positions are evaluated by fitting using (a) Centered Center of Gravity and (b) Parabola method for ω -stress analysis. A legend indicating four hydrogen L/D experiments performed on different Pd thin film specimens under similar setup and conditions.

In Pd thin films adhered to the substrate the $\alpha \leftrightarrow \beta$ phase transition induces in-plane compressive forces during (de)-hydrogenation [3]. *In-situ* stress measured during hydrogen L/D cycles for Pd and Pd on Ti layer films are plotted in Figure 4.4. The difference of compressive stress developed in Pd and Pd on Ti layer films upon H loading is almost of factor 2. For Pd-SiO₂/Si film the deloading-stress kept declining as more and more L/D cycles were performed; this stress relaxation is due to film cracking/buckling (Figure 4.5(b)). The buckles start spreading from the free end of the film, growing toward the center (Figure 4.1(b)). For Pd-Ti-SiO₂/Si film the deloading tensile stress was found increasing with increase in H-L/D cycles, because the Ti intermediate layer constrain free expansion during hydrogenation. Figure 4.6 shows the evolution of the deloading residual stress in Pd and Pd on Ti layer films for three reflections in both *in-situ* and *ex-situ* conditions. There is an

increase in the residual stress from the as-sputtered state to that after 1st H-L/D cycle and decrease further up to 20 cycles for Pd film (Figures 4.4(a) and 4.6(a)) occurs. For Pd on Ti layer the residual stress kept increasing after hydrogen cycling compared to the as-sputtered condition (Figures 4.4(b) and 4.6(b)). The stress followed by *in-situ* residual stress on Pd- $\{331\}$ and $\{420\}$ reflections is found to decrease for Pd film and increase for Pd on Ti layer with increasing cycles, and this is in agreement with the more reliable *ex-situ* stress measured for Pd- $\{311\}$ reflection in parallel-beam geometry.

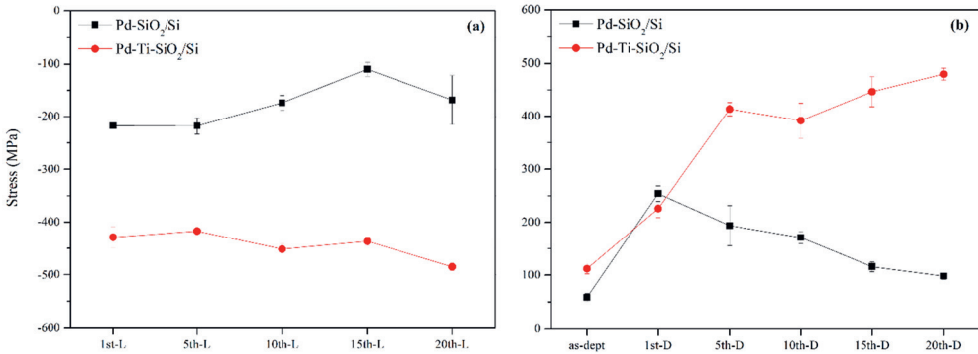


Figure 4.4 – *In-situ* stress measurements of Pd-SiO₂/Si and Pd-Ti-SiO₂/Si films for (a) 20 H-loading cycles and (b) 20 H-deloading cycles, *in-situ* stress performed at 1st, 5th, 10th, 15th and 20th L/D cycles. Peak fitting using Centered Center of Gravity method.

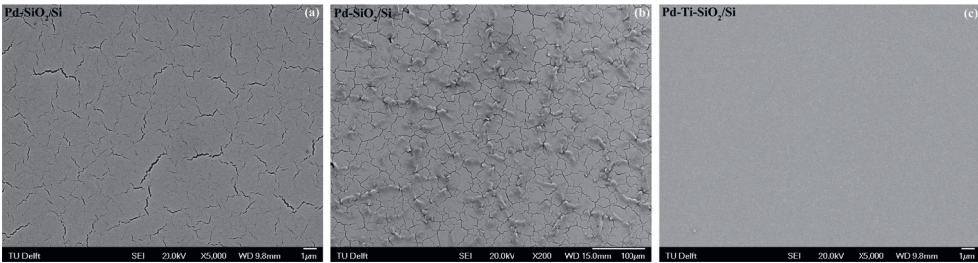


Figure 4.5 – SEM micrographs: (a) Pd-SiO₂/Si film after 5 L/D cycles, showing propagating microcracks, (b) Pd-SiO₂/Si film after 20 L/D cycles, showing both buckled and microcracked area, (c) Pd-Ti-SiO₂/Si film without any microcracks or buckles even after 20 L/D cycles, remained in as-sputtered condition.

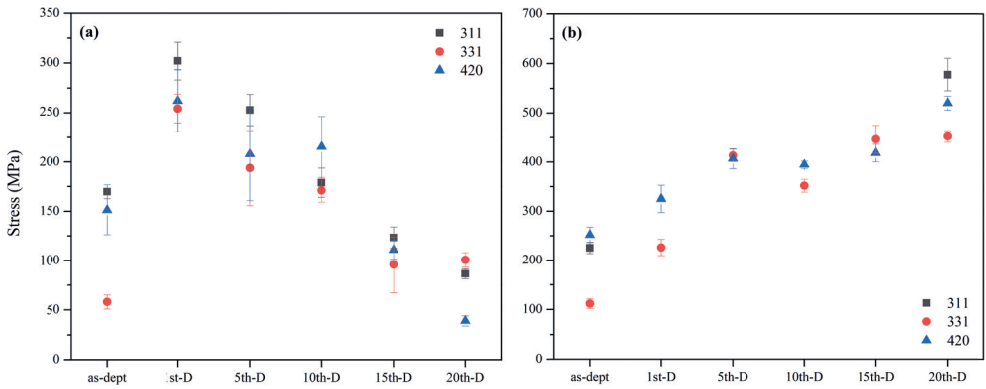


Figure 4.6 – Comparing residual stress in (a) Pd-SiO₂/Si and (b) Pd-Ti-SiO₂/Si films, after hydrogen L/D experiments, measured both *in-situ* (HT-XRD system) for the Pd- {331} & {420} reflections and *ex-situ* (PSI-XRD system) for the Pd-{311} reflection.

4.4. Conclusion

From the work done we can conclude that using the available focusing geometry, stress determination by ω -tilt method can be used to estimate the *in-situ* stress developed in Pd thin films during (de)-hydrogenation cycling. *In-situ* ω -tilt measurement results show similar trends for the Pd thin films residual stress as shown by *ex-situ* ψ -tilt measurements, within the estimated error. Alignment corrections for ω -tilt diffraction measurements were made, by performing verification measurements on a stress-free reference Pd-powder. Beside this, the experiments also showed the necessity of a detailed analysis of the *in-situ* XRD data from the HT-XRD system, i.e., appropriate choice of fitting method for obtaining peak positions.

This work also demonstrates that using Ti as an intermediate layer prevents pure Pd film failure due to $\alpha \leftrightarrow \beta$ phase transitions during hydrogen cycling. The results show that the compressive stress developed in Pd on Ti layer is about twice that in the Pd film. It is shown that the stress in the Pd film is released by buckling and that in the Pd on Ti layer the adhesive force is higher than the forces required to form buckles or to detach film from the substrate. Thus, a Ti adhesive intermediate layer can be used to enhance the lifetime of ultra-thin Pd films during hydrogen cycling.

4.5. References

- [1] Bryden KJ, Ying JY. Nanostructured palladium–iron membranes for hydrogen separation and membrane hydrogenation reactions. *J Membrane Sci.* 2002;203:29-42.
- [2] Wong M-f, Duan G, Wan K-t. Adhesion–delamination mechanics of a prestressed circular film adhered onto a rigid substrate. *The Journal of Adhesion.* 2007;83:67-83.
- [3] Pivak Y, Schreuders H, Slaman M, Griessen R, Dam B. Thermodynamics, stress release and hysteresis behavior in highly adhesive Pd–H films. *Int J Hydrogen Energ.* 2011;36:4056-67.
- [4] Welzel U, Ligot J, Lamparter P, Vermeulen A, Mittemeijer E. Stress analysis of polycrystalline thin films and surface regions by X-ray diffraction. *Journal of applied crystallography.* 2005;38:1-29.
- [5] Vermeulen AC. Considerations for collecting reliable XRD residual stress data across the full 2Theta range. *JCPDS-International Centre for Diffraction Data.* 2006:133-42.
- [6] Van Leeuwen M, Kamminga J-D, Mittemeijer E. Diffraction stress analysis of thin films: Modeling and experimental evaluation of elastic constants and grain interaction. *Journal of Applied Physics.* 1999;86:1904-14.
- [7] Welzel U, Mittemeijer EJ. Diffraction stress analysis of macroscopically elastically anisotropic specimens: On the concepts of diffraction elastic constants and stress factors. *Journal of Applied Physics.* 2003;93:9001-11.
- [8] Faurie D, Renault P-O, Le Bourhis E, Goudeau P. Study of texture effect on elastic properties of Au thin films by X-ray diffraction and in situ tensile testing. *Acta Materialia.* 2006;54:4503-13.
- [9] PANalytical X'Pert Stress Plus. PANalytical, Almelo, The Netherlands. 2012.
- [10] Hauk V. Structural and residual stress analysis by nondestructive methods: Evaluation-Application-Assessment: Elsevier; 1997.
- [11] Welzel U, Mittemeijer EJ. Diffraction stress analysis of elastic grain interaction in polycrystalline materials. *Zeitschrift für Kristallographie-Crystalline Materials.* 2007;222:160-73.
- [12] Voigt W. *Lehrbuch der Krystallophysik*, Teubner. Leipzig-Berlin. 1910.
- [13] Reuß A. *Zeitschrift für Angewandte Mathematik und Mechanik.* 1929;9:49-58.
- [14] Hill R. *Proc. Phys. Soc., London. Sect A.* 1952;65:349.
- [15] Hsu D, Leisure R. Elastic constants of palladium and β -phase palladium hydride between 4 and 300 K. *Physical Review B.* 1979;20:1339-44.
- [16] Welzel U, Mittemeijer EJ. Diffraction stress analysis of macroscopically elastically anisotropic specimens: On the concepts of diffraction elastic constants and stress factors. *Journal of Applied Physics.* 2003;93:9001 DOI: 10.1063/1.1569662.

5

Dislocations, texture and stress development in hydrogen-cycled Pd thin films: an *in-situ* X-ray diffraction study⁴

For Pd thin films, microstructural changes involved during hydrogen cycling provide the information needed to predict and optimize the film's mechanical strength. In this chapter, a systematic study of the morphology, microstructure, texture, and stress has been performed on Pd thin films during hydrogen loading and deloading cycles at room temperature. Pd thin films of similar morphology were prepared by magnetron sputtering on substrates of different compliances, i.e., Si-oxide, Titanium (Ti) and Polyimide (PI). The evolution of the morphology, grain-orientation distribution (texture), state of stress, and dislocation densities are analyzed for each of the film substrate types for 20 hydrogen loading/deloading cycles. The lattice expansion and contraction caused by the transition from Pd to Pd-hydride and back result in a strong stress increase. This stress increase stabilizes after a few cycles by grain boundary motion that leads to a gradual enhancement of the {111} texture and changes in the dislocation density for Pd films that are strongly clamped on to an oxidized Si(100) wafer substrate with an intermediate layer (Ti or PI). For Pd on PI, the stress is also partly released by a crack-based (crack widening/growth/propagation) pathway. Pd films on Ti and PI do not buckle or blister after 20 hydrogen cycles. By providing a sufficiently compliant substrate the traditional problems of buckle-delamination of a film on a stiff substrate are mitigated.

⁴ This chapter has been published as:

N. Verma, R. Delhez, N.M. van der Pers, R.W.A. Hendrikx, R.M. Huizenga, A.J. Böttger, *Dislocations, texture and stress development in hydrogen-cycled Pd thin films: An in-situ X-ray diffraction study*, International Journal of Hydrogen Energy, vol. 47, pp. 121119-12134, 2022.

5.1. Introduction

For the successful development of a hydrogen (H) economy [1-3], the palladium-hydrogen (Pd-H) system has been extensively studied [4-7]. Palladium (Pd) and its alloys are often used in industry as a sensor [8, 9], membrane [10, 11], and storage [12, 13] material for the detection, separation and purification of hydrogen. Pd interacts strongly with H and forms a solid solution hydride at room temperature [14]. Hydrogen readily dissociates on palladium surfaces. The hydrogen atoms adsorbed on the surface are in equilibrium with the absorbed subsurface hydrogen atoms that form palladium hydride within the metal lattice [15]. Nanostructuring of the metal hydrides provides a promising approach that has garnered substantial attention in the past decade [16, 17]. Nanostructured Pd is reported to exhibit unique hydrogen absorption and desorption behavior [7], size-dependent hydriding thermodynamics and kinetics [18, 19], as well as narrowing of the α -PdH_x and β -PdH_x miscibility gap [20, 21]. Recent works have shown that the defective Pd nanoparticle has the ability to remove crystallographic imperfections, thereby enhancing the nano-sized system's durability under the stresses resulting from large volume changes during hydrogen absorption and desorption [22, 23]. Hence, there is a lot of interest in studying the properties of Pd-based materials with significant potential for various hydrogen energy-related applications.

In nanocrystalline (nc) thin films, phase boundaries and hydrogen solubility depend strongly on film growth morphology and microstructure (including texture and stress) [24, 25]. The crystallographic orientation of the film depends on the deposition conditions as well as the substrate temperature [26]. Polycrystalline films can develop restricted crystallographic orientation distributions or textures during sputter deposition [27]. To estimate the orientation distribution of polycrystalline samples, it is often desirable to determine the volume fractions of different texture components. There are many methods to calculate these volume fractions, and the most commonly used is the orientation distribution function (ODF) [28]. For ODF analysis, at least three pole figures are required, thus leading to undesirably long data collection time. In addition, many ODF programs have difficulty handling weakly textured thin films. In the present study, texture is described in terms of simplified volume fraction analysis of the given components instead of an ODF or pole figure analysis. Since the studied Pd films have a fiber texture, the texture strength can be quantitatively represented from a single pole figure as a fiber texture plot (FTP).

For thin films, among various factors that affect hydrogenation [29, 30], stress is employed to explain changes in film behavior as caused by elastic constraining from the underlying layer

[31, 32], which is known as substrate clamping. The presence of residual stress distributions can significantly impact the adhesion [31] and fracture toughness of thin films [33]. From experimental and fundamental points of view, intense research has been conducted for decades towards the reliable assessment of stress on a submicron scale [34]. In thin films, specific microstructure (texture, columnar grains, defects), film thickness, and grain size are responsible for the macroscopic elastic anisotropy which influence diffraction-stress analysis [35]. In such a case, the so-called X-ray stress factors relate the lattice strain to mechanical stress and depend not only on the specific hkl reflections but also on the angles ψ and φ at which the strain was measured. Several grain interaction models have been proposed to study the elastic properties of thin films [36]; however, due to the actual geometric arrangement of grains, it is still quite difficult to take them into account. For thin films with fiber texture, one can use a technique that is similar to the one used for stress analysis in single crystals, the crystallite group method (CGM) [37]. This method was applied together with the conventional $\sin^2\psi$ method to estimate stress evolution in Pd thin film during hydrogen cycling.

The presence of stress in thin films leads to film cracking due to tensile stress, and buckling or blistering in the case of compressive stress. Global buckling and its driven delamination in thin films are typically observed on a stiff substrate [38]. The enormous field of fracture mechanisms has been developed to understand and predict the conditions under which cracks nucleate and propagate [39, 40] so that cracking can be avoided in thin films. Lee *et al.* [41] utilize crack formation in Pd thin films, which, when exposed to hydrogen, expand laterally, altering the width of the cracks to produce reliable and reproducible multiple-cracked Pd film as a highly sensitive H_2 sensor. In the multiple-cracking phenomena, stresses are shared and transferred from one component to another, which prevents reaching a critical value of the strain energy. Thus, cracking could be used as a means to release H stress, but also a good adhesion between the thin film and the stiff substrate is required to avoid further film rupture by necking [42].

In the Pd-H system, the initial volume of the Pd structure expands by 10.4 vol.% when the H/Pd ratio reaches about 0.6 [14]. This expansion can generate large compressive stresses if the deformation is deterred by a mechanical constraint imposed to a thin film lying on a thick substrate. Such fundamental issues have been addressed in previous studies [43, 44], where we used Pd thin films with open columnar morphology that stabilizes against embrittlement both at room temperature and at high temperature depending on the complicity of the

intermediate layer used. We further investigate the stability of such Pd thin film systems after a long-term operation during hydrogen cycling in the current chapter. Flanagan *et al.* [45] have reported plastic deformation both during hydriding and dehydriding processes in Pd which leads to an overall increase of the dislocation density. Several transmission electron microscopy (TEM) studies have been dedicated to studying the dislocation-hydrogen interaction mechanisms and dislocation-mediated relaxation in hydride nc palladium films [30, 46, 47]. It is found that in nc materials grain boundaries act as rapid diffusion paths for hydrogen but also hydrogen diffusion is retarded due to hydrogen trapping by dislocations. More generally, because of the complexity of the microstructure of nc metals, the microstructural changes associated with the phase transformations strongly differ from coarse-grained metals.

In this chapter, three different Pd thin films, sputter-deposited with and without intermediate layer but with practically identical microstructures, are studied. This allowed us to deduce the influence of the intermediate layer (substrate types) on the morphology, preferred orientation (texture), state of stress and dislocation density as a function of hydrogen cycling. It was found that the cyclic process results in an irreversible texture change. The stress analysis results show that the stress evolution during cycling is different for all three Pd thin film systems, and the film-substrate interface determines the deformation behavior. These findings are further supported by transmission and scanning electron microscopy (TEM and SEM) investigations for morphological changes. X-ray diffraction (XRD) line-broadening analysis was used to investigate the (plastic) deformation mechanism.

5.2. Experimental

5.2.1. Pd thin film preparation

The Pd thin films of $\sim 100 \pm 10$ nm thickness were dc-magnetron sputter deposited. The process details are described in our previous work [44], chapter 3. In brief, Pd was deposited for 900 s in an argon (Ar) atmosphere at 3 Pa. The gun (Pd target with 99.95% purity) was operated at 100 W dc power with an average deposition rate of 0.1 nm/s. The Pd thin films were deposited at room temperature onto three different substrate types: (i) thermally oxidized (~ 188 nm) single-crystal Si(100) wafer (SiO_2/Si), (ii) a sputter-deposited Titanium (Ti) interlayer on a SiO_2/Si wafer ($\text{Ti-SiO}_2/\text{Si}$) and (iii) a spin-coated polyimide (PI) interlayer on a SiO_2/Si wafer ($\text{PI-SiO}_2/\text{Si}$). About 6 nm Ti interlayer was deposited during 360 s at 3 Pa Ar

pressure (0.016 nm/s) [43]. The PI (5 μm) spin-coated SiO_2/Si wafers were prepared at Else Kooi Lab (EKL), TU Delft. After deposition, the Pd thin films were transferred into a single wafer container and stored at room temperature.

Investigation of cross-sectional morphology of Pd thin film was performed using CM30T and CM300UT-FEG Philips Transmission Electron Microscopy (TEM), type Tecnai F20ST/STEM (FEI Electron Microscopes) with energy dispersive spectroscopy (EDS). Scanning electron microscopy (SEM) JEOL JSM 6500F from Japan Electron Optics Ltd was used to investigate the changes related to the surface morphology of Pd thin film (e.g., microcracks and blisters) upon hydrogen loading/deloading.

5.2.2. X-ray diffraction (XRD)

In view of the availability and comparability of data from two different diffractometer settings, the hydrogen cycling experiments were performed in focusing geometry (Bruker-AXS D5005) and parallel-beam geometry (Bruker-AXS D8).

5.2.2.1. Focusing optics diffractometer: Hydrogen cycling

20 slow hydrogen loading/deloading cycles (20-L/D) were performed on an *in-situ* XRD set-up: Bruker-AXS D5005 diffractometer in a Bragg-Brentano focusing geometry ($\text{CuK}\alpha$; 45 kV, 30 mA), equipped with an MRI HT chamber (D5005). The chamber is supplied with a mass flow controller to conduct loading in $5\%\text{H}_2 + 95\%\text{N}_2$ ($(p\text{H}_2) = 0.05 \text{ atm}$) gas mixture and deloading in N_2 (1 atm) gas. The measurements were performed at room temperature and atmospheric pressure.

The *in-situ* set-up was used to monitor hydrogen cycling and measure stress developed during hydrogen loading/deloading in Pd films simultaneously. For slow 20-L/D cycles, continuous 2 min short scans (see Appendix B, Figure B1) in the range $36\text{--}43^\circ 2\theta$ (including peaks of the Pd- α and β phases) were made until complete loading and deloading had been achieved at each cycle. This was followed by a long overview scan (see Appendix B, Figure B2) over three ranges: $36\text{--}43^\circ 2\theta$ (including the Pd- $\{111\}$), $43\text{--}50^\circ 2\theta$ (including the Pd- $\{200\}$) and $74\text{--}90^\circ 2\theta$ (including the Pd- $\{311\}$ and $\{222\}$ reflections) for the numerical evaluation of microstructural changes. For each range, counting time and step size were chosen to take into consideration the counting statistics of the weaker diffraction peaks. The instrumental profile

was determined by measuring, under analogous conditions, NIST/NBS LaB6 powder (SRM660a) [48] on a Si(510) single-crystal substrate.

In between cycling, in-plane stress was measured after the 1st, 5th, 10th, 15th, and 20th L/D cycles by applying instrumental ω -tilt (tube: $\theta+\omega$; detector: $\theta+\omega$) using the Pd- α and Pd- β -{331} and {420} reflections (see Appendix B, Figure B3). ω -offset was provided for ψ -tilt angles 0°- 45° in step mode ($\sin^2\psi \approx 0 - 0.5$ in steps of 0.1). Pd- α at $\sin^2\psi \approx 0.2$ and 0.3 and Pd- β at $\sin^2\psi \approx 0.3$ and 0.4 of {331} and {420} reflections were not used because at these ω -tilt angles, the window frame of the MRI chamber obstructs the diffraction signal. Therefore, only four points were used for the lattice strain measurement (see Appendix B, Figures B13(b) and 14(b)). The total measurement times for ω -stress scans ranged from 22 to 24 hours. The counting time was rather long on purpose to detect minimal variations due to counting statistics. Since the D5005 system has focusing optics, defocusing errors due to omega-tilting are inevitable. For defocusing correction, Palladium powder (AlFa-D24F20) was used for which the stress-free state has been checked with the $\sin^2\psi$ method using a parallel-beam diffractometer.

5.2.2.2. Parallel-beam diffractometer: Hydrogen cycling

In contrast to the D5005 system, the parallel-beam geometry allows measurements at large tilt angles without defocusing, whereas also specimen position and roughness are not critical. However, primarily the hydrogen cycling experiments were repeated on this diffractometer to provide a way to simultaneously monitor texture and stress in Pd films during hydrogen cycling.

In this *in-situ* XRD set-up (see Appendix B, Figure B4), a Pd thin film for 20-L/D cycles was mounted (using vacuum grease) in the custom-made specimen holder connected to a Bruker D8 diffractometer in parallel-beam optics equipped with Huber ¼ Eulerian cradle, called the PSI-XRD system. The holder consists of a cavity covered by a transparent foil Chemplex Prolene® of 4 μm thickness, enabling direct visualization of the topographic changes in Pd thin film upon hydriding. CoK α radiation ($\lambda = 0.179026$ nm) appears from the point focus geometry of the sealed X-ray tube operated at 45 kV and 25 mA. The diffracted beam passed a parallel soller slit of 0.35° and a graphite monochromator before reaching the detector.

For each loading and deloading cycle, the transformation was monitored by a loop of short scans in the 2θ range 43–49° (see Appendix B, Figures B5 and 6), containing the Pd-{111} reflections of the α - and β -phase. Using a step size of 0.05° 2θ and a counting time per step of

1 s, the time per scan is 2 min. The loop scans enabled to follow the start and finish of each transformation in time and detail. In order to monitor change in line-width, overview long scan in the 2θ range 40–110° (see Appendix B, Figure B7), including the Pd {111}, {200}, {311} and {222} reflections was made with an omega offset of 2° to avoid the very strong Si{400} from the substrate. Under ambient conditions, hydrogen loading was conducted in a gas mixture of 5%H₂ + 95%N₂ (pH₂ = 0.05 atm) and deloading in N₂ gas (1 atm). The scanning sequence included: (1) loading short loop scans, (2) loading long overview scan, (3) texture/stress measurements under loading condition, (4) deloading short loop scans, (5) deloading long overview scan, and (6) texture/stress measurements under deloading condition. This sequence was repeated for each cycle, except that texture/stress measurements were performed only for cycle 1, 5, 10, 15, and 20. The data evaluation of the diffraction profiles was done with the program Bruker – EVA [49].

5.2.2.3. Texture and stress measurements

When high stresses are present, a conventional method based on pole figures cannot be used for texture determination since the 2θ peak position considerably changes with ψ -tilting [50]. In this work, after ensuring the fiber symmetry of the crystallographic texture (see Appendix B, Figure B8), the measurement strategy of collecting the entire diffraction peak (θ – 2θ scan) for different sample ψ -tilt angles at fixed rotation angle ϕ was adopted. The rotation direction was chosen such that no disturbance occurred by the diffraction from the single-crystalline Si wafer. The intensities of the diffraction lines Pd {111}, {200} and {311} were recorded as a function of ψ -tilt angle (see Appendix B, Figure B9). The ψ range is 0°–75° in steps of 10° and total scan time 30 hours. The incident beam size is adjusted with a crossed slits assembly which enables to limit the beam in two perpendicular directions: height and width. Sample size and incident beam size combination were carefully chosen, such that the irradiated area did not exceed the specimen surface area at all orientations of the samples [51]. The characteristic parameters of the individual peaks were evaluated by fitting pseudo-Voigt functions to the measured data using the software package PANalytical X'Pert Stress Plus [52]. Additional data processing was applied as required for texture and stress analysis.

5.2.2.4. XRD line-broadening: microstructure characterization

The deformation in terms of defect parameters such as crystallite sizes and dislocations densities were obtained by line-broadening analysis of X-ray diffraction profiles using the integral breadth [53]. The analysis was performed on long overview scans (see Appendix B,

Figure B2) from 20 hydrogen loading/deloading cycles run on the Bruker D5005 set-up (section 5.2.2.1.). The measurement and data analysis details are described in our previous work [44], chapter 3.

The measured XRD peak profile and broadening is the result of the convolution of the instrumental broadening of the diffractometer and the broadening introduced by microstructural imperfections in the sample called microstructural broadening. The instrument-corrected broadening β_{hkl} corresponding to the diffracted peak of Pd thin film was estimated using:

$$\beta_{hkl} = [(\beta_{hkl})^2_{measured} - (\beta_{hkl})^2_{instrumental}]^{1/2} \quad (5.1)$$

because the shape of all line profiles involved was close to Gaussian as found from profile fitting.

In the rest of this study β^*_{hkl} , the integral breadth in reciprocal space is used instead of β_{hkl} :

$$\beta^*_{hkl} = \frac{\beta_{hkl} \cos \theta}{\lambda} \quad (5.2)$$

It is assumed here that the microstructural broadening was caused by crystal imperfections and small crystallite size, and that the effects of broadening by crystallite size and by crystal imperfections are additive.

The more probable crystal imperfections appear to be dislocations. We concluded, based on the lattice constants obtained from the measured line profiles, that stacking and twin faults are very unlikely to significantly contribute to the line broadening [54]. Therefore the line breadths were evaluated by the modified Williamson-Hall (mod-WH) method [55, 56]. The method accounts for the anisotropic strain fields of dislocations by introducing the Contrast Factor C_{hkl} of dislocations. C_{hkl} depends on the types, densities, and arrangements of the dislocations present, as well as on the orientation distribution of the dislocations with respect to the diffraction vector g_{hkl} . The integral breadth is given by

$$\beta^*_{hkl} = \frac{K}{\langle D \rangle} + \left(\frac{\pi M^2 b^2}{2} \right)^{\frac{1}{2}} \left[\frac{h^2 + k^2 + l^2}{a^2} \right]^{\frac{1}{2}} \rho^{\frac{1}{2}} C_{hkl}^{\frac{1}{2}} \quad (5.3)$$

where K is a constant (here taken as 1), $\langle D \rangle$ (nm) is the average crystallite size (perpendicular to the Pd layers), M is a constant describing the dislocation arrangement [57] (here taken as 1), ρ is the dislocation density (m^{-2}), b is the length of the Burgers vector, and a

is the lattice constant. The calculated contrast factors for Pd thin films are provided in our previous work [44], chapter 3.

5.3. Results and discussion

5.3.1. Morphology analysis: evolution during cycling

To divulge the influence of the intermediate layer (substrate type) on hydrogen cycling, we envisioned growing comparable Pd films with open morphology (and texture) on all substrates. In previous works [43, 44, 58], chapters 2, 3 and 4, it was shown that a Pd thin film with an open columnar structure is stabilized against embrittlement. Figure 5.1 shows TEM bright-field images of Pd thin films with an adhesive intermediate layer (Pd on Ti and Pd on PI) in an as-deposited state and after 20 hydrogen loading/deloading cycles (20-L/D). One clear feature in all Pd thin film specimens is the presence of elongated voids at part of the grain boundaries (Figures 5.1(a–d)). Columnar structures are more or less elongated in shape, and some columns run (almost) from top to bottom. The observed Pd thin-film features like grain size, voids, and twins showed no major difference between the four investigated film specimens (Table 5.1). TEM could not be performed on Pd film without intermediate layer (Pd-SiO₂/Si) due to Pd layer buckle-delamination after 20-L/D cycles; contrarily, Pd-Ti/SiO₂/Si and Pd-PI/SiO₂/Si films remained strongly adhered to the substrate. TEM images of as-deposited Pd thin films with and without intermediate layer are also shown in our previous work [44], chapter 3.

Figure 5.2 shows the SEM planar view of as-deposited Pd films in the first row and Pd films at the end of 20-L/D cycles in the second row. Figures 5.2(a–c) at 10 μm scale have a smooth appearance in the as-deposited condition, and high magnification (100 nm) insets show low-density open morphology for all Pd films with and without intermediate layers. Exposure to hydrogen causes the Pd film to expand, and upon subsequent deloading, it returns to its original state [20]. During hydrogen loading films are subjected to biaxial compressive stress due to which the film buckles, thus releasing most of the stress [32]. However, the real-time monitoring of cycling experiments on the PSI-XRD system showed the absence of buckle formation during hydrogen loading for all Pd films studied. In other words, the open columnar structures allow Pd thin film clamped on a stiff substrate to breathe (expand) during hydrogen uptake. In contrast, Pd films with close columnar structures had shown buckle formation during loading and buckle-delamination after the $\alpha \leftrightarrow \beta$ phase transformation [44], chapter 3.

Table 5.1 – TEM investigated microstructural features indicated for Pd-Ti-SiO₂/Si and Pd-PI-SiO₂/Si films in as-deposited state and after 20 hydrogen loading/deloading cycles (20-L/D).

	Pd Thickness (nm)	Ti Thickness (nm)	Grain size (nm) (width x height)	Twins	Voids (nm) (width x height)
Pd-Ti-SiO₂/Si (as-dept.)	110–125	7.5 ± 0.7	15 x 15–20 x 80	yes	> 3 x 90
Pd-PI-SiO₂/Si (as-dept.)	110–140	–	(20–50) x (20–120)	yes	(2–6) x (20–50)
Pd-Ti-SiO₂/Si (after 20-L/D)	100–120	3 ± 0.5	(15–25) x (80–100)	yes	(2–7) x (7–25)
Pd-PI-SiO₂/Si (after 20-L/D)	105–135	–	6 x 20–25 x 75	yes	(2–3) x (20–60)

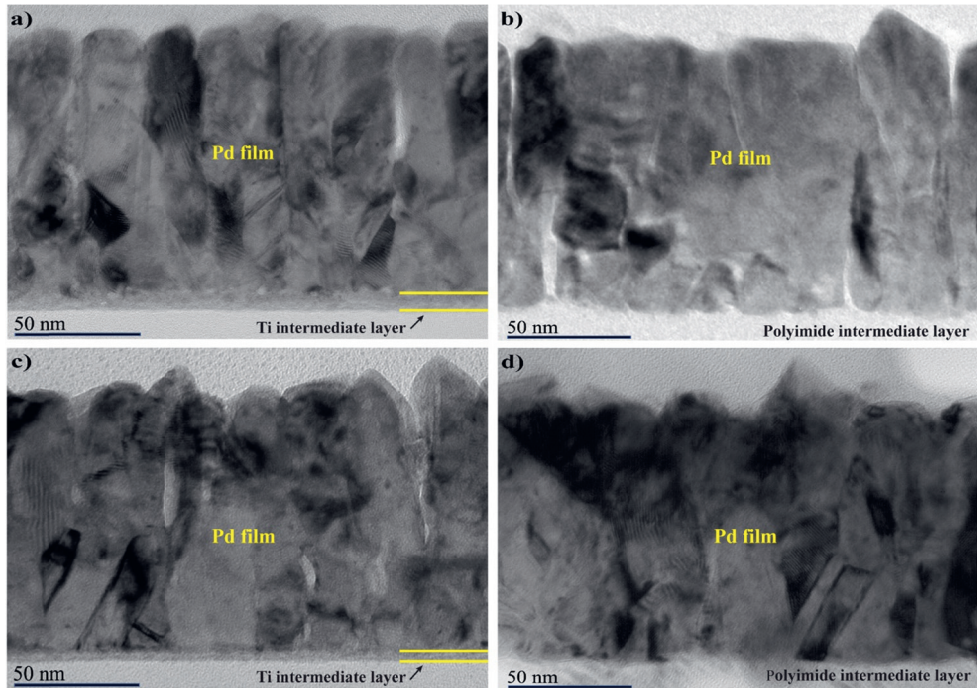


Figure 5.1 – A cross-sectional view of TEM bright-field (BF) images of ~100 nm Pd thin films. Film morphology in as-deposited state: (a) Pd-Ti-SiO₂/Si and (b) Pd-PI-SiO₂/Si, and after 20 hydrogen loading/deloading cycles (20-L/D): (c) Pd-Ti-SiO₂/Si and (d) Pd-PI-SiO₂/Si.

Ti-SiO₂/Si and (d) Pd-PI-SiO₂/Si. All Pd film specimens show open columnar structures which are more or less elongated in shape, often running from top to bottom.

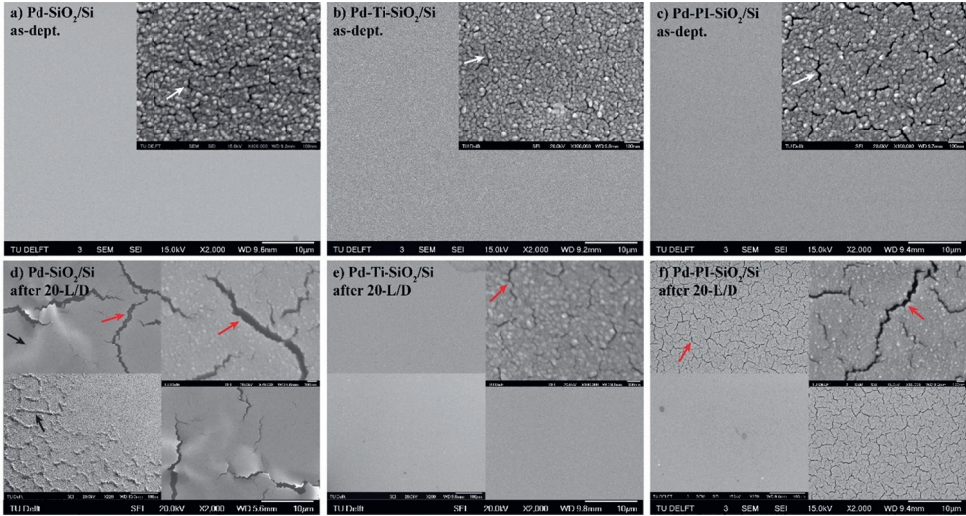


Figure 5.2 – SEM images illustrating surface morphology of as-deposited and hydrogen cycled Pd thin films. From left to right: a&d) Pd-SiO₂/Si, b&e) Pd-Ti-SiO₂/Si and c&f) Pd-PI-SiO₂/Si. The top layer contains as-deposited films with large images at a 10 μm scale and the inset images at a 100 nm scale. The bottom layer includes films after 20 hydrogen loading/deloading cycles (20-L/D) with large images of 10 μm scale and the inset images at 100 nm and 100 μm scales. The white arrows indicate as-deposited networks of primary microcracks associated with intercolumnar voids. The red arrows indicate hydrogen-induced microcracks, and the black arrows indicate delamination buckles or blisters in Pd-SiO₂/Si film after 20-L/D cycles. Note that the micrographs of as-deposited films and films after 20-L/D are from two different samples.

SEM micrographs in Figure 5.3 compare surface topography of Pd-SiO₂/Si film after 1, 5, 10, 15 and 20-L/D cycles with respect to its as-deposited state. Already after the first hydrogen cycle, Figure 5.3(b), Pd film shows widening of existing as-deposited microcracks. Microcrack initiation starts at a surface defect because of the highly localized strain concentration at the grain boundaries [59]. Further cycling increases microcrack width

gradually, as seen in subsequent SEM images Figures 5.3(c–f). In the beginning, microcracks form a fine web network (Figure 5.3(b) inset), but with cycling, scattered wide cracks occur, as seen in Figures 5.3(c–f) inset. In the evolving film morphology after cycling, islands of compact morphology between wide cracks are found. The microcrack propagation is followed by buckling. Complementary optical microscopy (OM) images in Figure 5.4(a) show buckled morphology on the film surface observed only after exposure to 10-L/D cycles. The onset of buckling starts from the specimen edge, propagating towards the center. Strain localization facilitates microcrack propagation through the buckled region, which provides the additional driving force for the film delamination. Consequently, after 20-L/D hydrogen cycles, the Pd film on bare SiO_2/Si substrate exhibits peel-off traces of buckles with wide microcracks and wrinkles all over the film specimen (Figures 5.2(d), 5.3(f) and 5.4(c)). Delaminated margins are seen as bright areas around the microcracks in SEM images. Here, due to weak cohesion between the Pd film and the substrate, the structural integrity of the thin-film system is compromised to facilitate stress relaxation.

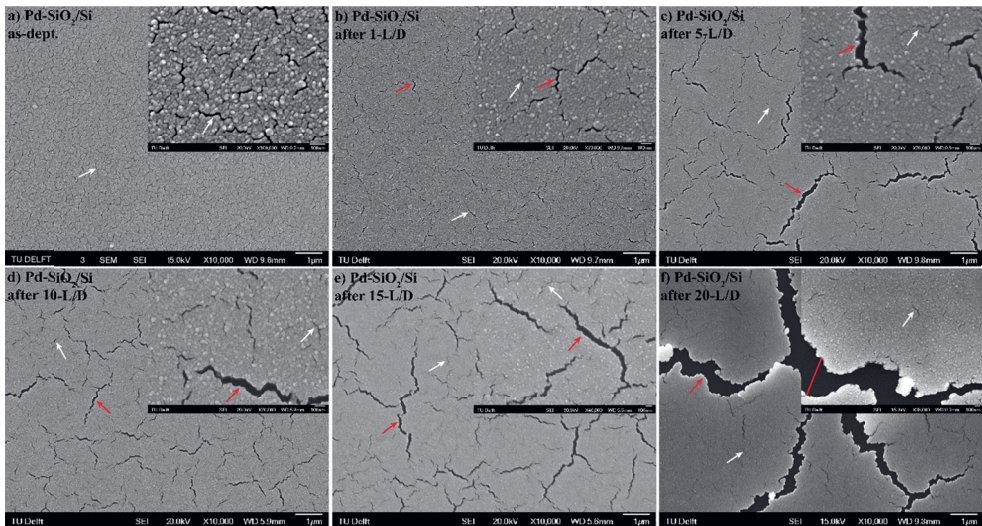


Figure 5.3 – SEM micrographs with low (10 μm) and high magnification (100 nm) illustrates surface morphology of a Pd- SiO_2/Si thin film in different states: (a) as-deposited, (b), (c), (d), (e), and (f) corresponds to the loading/deloading cycle numbers of 1, 5, 10, 15 and 20, respectively. The white arrows indicate as-deposited distributed microcracks and the red arrows indicate a hydrogen-induced widening of microcracks after loading/deloading cycle/cycles. Note that the micrographs were taken from six different samples.

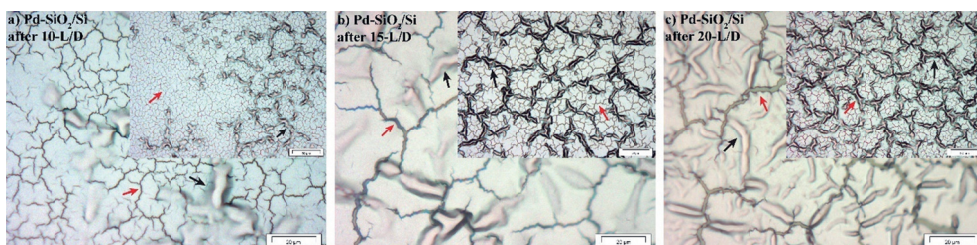


Figure 5.4 – Optical microscopy (OM) micrographs with low (50 μm) and high magnification (20 μm) illustrating the formation of the blister network in hydrogen cycled Pd-SiO₂/Si thin film after: (a) 10-L/D cycles, (b) 15-L/D cycles, and (c) 20-L/D cycles. The red arrows indicate hydrogen-induced microcracks and the black arrows indicate delaminated-buckles or blisters in Pd film after loading/deloading cycles. Note that the micrographs were taken from three different samples.

Microcrack propagation (growth and widening) during hydrogen cycling is limited for the Pd-Ti/SiO₂/Si film. After 20-L/D cycles, the film structure remained very similar to the as-deposited state (Figure 5.2(e)) with very few scattered and rather narrow microcracks visible only in high-magnification (100 nm scale), top inset of Figure 5.2(e). The surface morphological results demonstrate that a Ti adhesive intermediate layer substantially improves the Pd film compliance – the stability of the film during hydrogen cycling. For sputtered metal films of columnar morphology, intergranular spacing along grain boundaries can increase compliance [60]. Such morphology allows smooth phase transitions in the Pd-Ti/SiO₂/Si film, where the Pd film cannot be stretched due to reinforced film adhesion to the rigid substrate. The open morphology of the Pd film and the strong interface bonding between the film and underlying substrate facilitate each other, resulting in a stable Pd thin film system. However, the rigid substrate confines the deformation of the film in its plane. To rationalize these observations, further XRD microstructural analysis is conducted and reported in the following sections.

Similarly, Pd-PI/SiO₂/Si film endures strain accumulation and relaxation during 20-L/D cycles. As opposed to a blister-delaminated surface that is visible at 100 μm scale for Pd film without intermediate layer (Figure 5.2(d) bottom inset), Pd on PI film appears smooth at the same magnification (Figure 5.2(f) bottom inset). Hydrogen-cycling induced microcracks are uniformly spread in the large image of 10 μm scale (Figure 5.2(f)) contrary to a smooth surface in the as-deposited condition in Figure 5.2(c). In the high magnification top inset of

Figure 5.2(f), we see a few as-deposited primary microcracks and more compact morphology as compared to open as-deposited morphology in the inset of Figure 5.2(c). PI intermediate layer plays a pivotal role in providing a flexible alternative to elasticity limitation inherent to the thin film supported on a stiff substrate [42]. The enhancement of film-substrate adhesion can suppress strain localization [33, 61], allowing for a homogenous deformation, such that Pd film can recover from high total strain due to lattice expansion. An increase in microcrack spacing was noticed already after the 1st-L/D cycle (see Appendix B, Figures B10(a–c)); however, stress relaxation at the flexible film-substrate interface prevents subsequent microcrack widening or propagation. Here, free surfaces (due to microcrack widening during the 1st-L/D cycle) and interfaces play an important role that leads to a much higher stretchability of the Pd thin film during the cycling process. This microstructural stabilization mechanism implicates freedom to expand/contract during H loading/deloading and stress relaxation along the crack spacing. Therefore, one can expect that substrate constrain disappears in the metal thin film without debonding when clamped on a polymer substrate.

5.3.2. Texture analysis: Quantification of weak and broad fiber texture

For fiber texture that is not well developed (weak fiber texture), a method has been presented to quantify the volume fraction of the material associated with the texture and random component [62]. This method involves two steps to determine texture volume fraction from ψ -tilt measurements, which includes the entire reflection (2θ scans) (see Appendix B, Figure B9). From the 2θ scans, the measured (integrated) intensity, $I_{\text{net}}(\psi)$, after a linear background fitting was obtained using the Bruker – EVA software [49]. $I_{\text{net}}(\psi)$ was corrected for thin layer and instrumental intensity loss to obtain the corrected (integrated) intensity, $I_{\text{corr}}(\psi)$ [51]. In the first step, the spread of the texture components is defined by applying Gaussian fitting to the $I_{\text{corr}}(\psi)$ (see Appendix B, Figure B11). The occurrence of a texture component, defined as the density of poles, $n(\psi)$, is proportional to the $I_{\text{corr}}(\psi)$. The texture components from the separated intensity maxima (pole density) as a function of ψ are represented employing the pole density plots (PDP) as shown in Figure 5.5. The PDP is principally similar to fiber texture plot (FTP), with a cut in a crystallographic direction from the center ($\psi=0^\circ$) to the outer edge of the pole figure ($\psi=75^\circ$). The experimental results for the $\{111\}$ and $\{200\}$ reflections of Pd thin film in Figure 5.5 indicate that the orientation distribution of crystals in

the layer is composed of two components: (i) a $\langle 111 \rangle$ fiber texture and (ii) a randomly orientated fraction. The breadth of the maximum at $\psi = 0^\circ$ in the $\{111\}$ -PDP (Figure 5.5(a)) is a parameter which is indicative for the “sharpness” of the texture, *i.e.*, spread in the orientation distribution, which amounts to $35\text{--}40^\circ$ in the represented case of the weak fiber texture in Pd thin films.

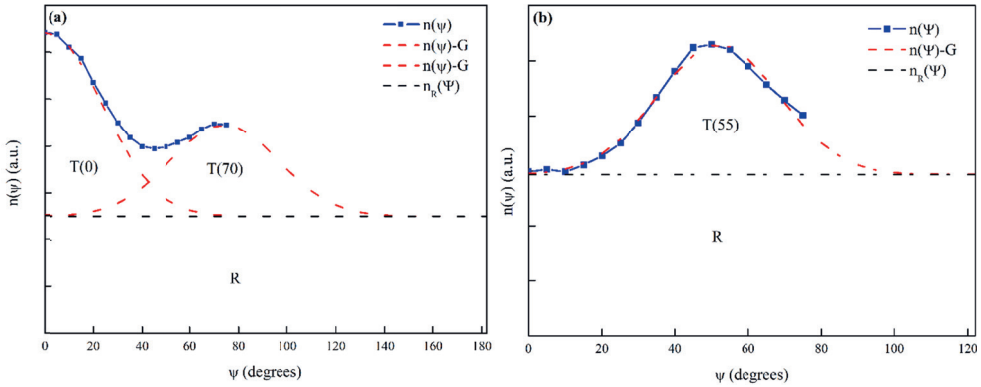


Figure 5.5 – Pole density plot (PDP). Density of $\{111\}$ poles, $n(\psi)$, versus specimen tilting angle ψ for a Pd thin film (Pd-SiO₂/Si) with weak fiber texture: (a) $\{111\}$ -PDP displaying $\langle 111 \rangle$ fiber texture maxima at $\psi = 0^\circ$ and 70° and (b) $\{200\}$ -PDP displaying a $\langle 111 \rangle$ fiber texture maxima at $\psi = 55^\circ$.

In the second step, texture components are calculated from the separate intensity maxima in the pole number plot (PNP), represented in Figure 5.6. To calculate the total number of poles, *i.e.*, the volume fraction of material associated with the respective texture components, we assumed that the film tilting angle ψ is varied stepwise with an increment $\Delta\psi$. The element of area, $\Delta A(\psi)$, on the surface of the reference hemisphere of the unit radius with the equatorial plane coinciding with the specimen surface is, $\Delta A(\psi) = 2\pi[\cos(\psi - \Delta\psi/2) - \cos(\psi + \Delta\psi/2)]$. The total number of $\{hkl\}$ poles, $\Delta N(\psi)$, intersecting this area is,

$$\Delta N(\psi) = n(\psi) * \Delta A(\psi) \quad (5.4)$$

For the Pd thin film, $\Delta N(\psi)$ as derived from $n(\psi)$ (*i.e.*, $I_{\text{corr}}(\psi)$) of $\{111\}$ and $\{200\}$ reflections (Figure 5.5) are plotted against specimen tilting angle ψ in Figure 5.6. The volume fractions of crystallites associated with the respective texture components can be calculated from the areas T (texture) and R (random) in Figure 5.6. First, the random component is considered. The number of poles in an element of an area associated with the random component varies

with ψ according to Eq. 5.4 with a constant value for $n(\psi)\text{-G} = n_R(\psi)$. This constant value is chosen such that the curve for $\Delta N_R(\psi)$ is tangent to the curve for $\Delta N(\psi)\text{-G}$, as shown in Figure 5.6. In pole density plots, the Gaussian fitting for the curve $n(\psi)\text{-G}$ was extrapolated beyond the measured $n(\psi)$, i.e., $\psi = 75^\circ$ up to a point, where, $n(\psi)\text{-G} = n_R(\psi)$ (Figure 5.5). Due to the presence of minor texture components (Pd $\langle 311 \rangle$ and $\langle 200 \rangle$) (see Appendix B, Figure B12(b)), that interfere with pole area of major $\langle 111 \rangle$ -texture component in $\{111\}$ -PDP, texture quantification for Pd thin film was performed using $\{200\}$ -PDP. For a $\langle 111 \rangle$ fiber texture, maxima in $\{200\}$ pole plot occur at $\psi \approx 55^\circ$ (T55), with a $\langle 111 \rangle$ pole multiplicity of 3 (3T(55)). Taking into account the multiplicity of poles, the volume fraction of crystallite, $f_{\langle 111 \rangle}$, associated with the $\langle 111 \rangle$ texture, was calculated exclusively from the maxima T(55) in Figure 5.6(b) from $\{200\}$ pole number plot:

$$f_{\langle 111 \rangle} = \frac{T(55)}{R + T(55)} = \frac{\sum_{i=1}^{m55} [\Delta N(\psi) - \Delta N_R(\psi)]}{\sum_{i=1}^N \Delta N_R(\psi) + \sum_{i=1}^{m55} [\Delta N(\psi) - \Delta N_R(\psi)]} \quad (5.5)$$

where i is the number of the steps in the extrapolated ψ step-scan, and the summation represents the numerical integration of the fitted experimental data over the areas T(55) and R in Figure 5.6(b). This extrapolation and integration method is suitable for simple texture quantification of a thin film with weak fiber texture. The method was first successfully established for strong fiber textured Pd thin films for which the overlapped major and minor texture components can be easily separated and calculated (see Appendix B, Figure B12).

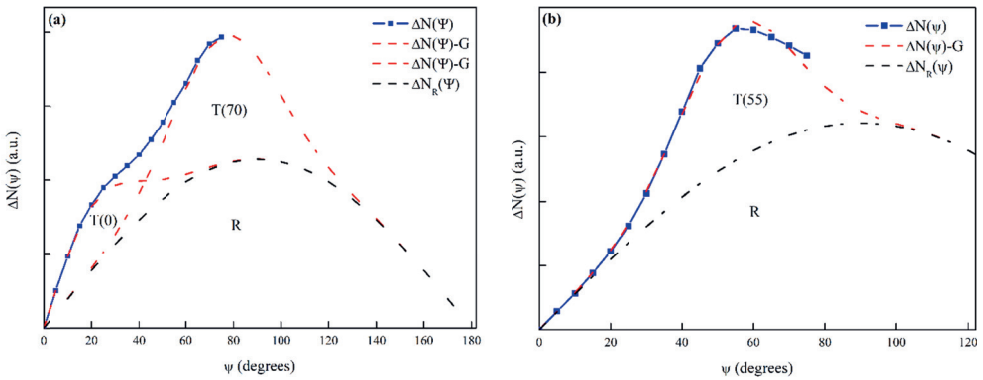


Figure 5.6 – Pole number plot (PNP). Number of poles, $\Delta N(\psi)$, in: (a) Pd- $\{111\}$ and (b) Pd- $\{200\}$ reflections generated from PDP in Figure 5.5. The area T(0) and T(70) in $\{111\}$ -PNP and area T(55) in $\{200\}$ -PNP is associated with the $\langle 111 \rangle$ fiber texture, whereas the area R is associated with the randomly oriented crystallites.

Table 5.2 – Volume fractions of $\{111\}$ -fiber texture ($f_{\langle 111 \rangle}$) and random component (R) calculated from $\{200\}$ -PDP in Figure 5.6(b). Texture quantification performed on hydrogen cycling experiments was conducted on: (a) D5005 system and (b) PSI-XRD system.

(a)	Pd-SiO ₂ /Si		Pd-Ti-SiO ₂ /Si		Pd-PI-SiO ₂ /Si	
	Volume fractions		Volume fractions		Volume fractions	
	$f_{\langle 111 \rangle}$	Random	$f_{\langle 111 \rangle}$	Random	$f_{\langle 111 \rangle}$	Random
as-dept. (Pd)	0.25	0.75	0.25	0.75	0.23	0.77
20-L/D (Pd)	0.32	0.68	0.34	0.66	0.30	0.70

(b)	Pd-Ti-SiO ₂ /Si		Pd-PI-SiO ₂ /Si	
	Volume fractions		Volume fractions	
	$f_{\langle 111 \rangle}$	Random	$f_{\langle 111 \rangle}$	Random
as-dept. (Pd)	0.32	0.68	0.32	0.68
1 st -L (PdH _{0.66})	0.35	0.65	0.39	0.61
1-L/D (Pd)	0.39	0.61	0.42	0.58
20 th -L (PdH _{0.66})	0.43	0.57	0.51	0.49
20-L/D (Pd)	0.46	0.54	0.47	0.53

5.3.2.1. Texture results for Pd thin films

In Table 5.2 are listed the volume fractions of (111)-fiber texture, $f_{\langle 111 \rangle}$, and the random (R) component calculated from the $\{200\}$ -PDP. Quantification of texture component fractions simplifies tracking the texture evolution with H-cycling in Pd thin films. Sharpening of (111)-fiber texture is observed for all Pd thin films studied for hydrogen cycling on two different diffractometers. Likewise, Harumoto *et al.* [63] have shown for a 48 nm Pd thin film, a change in the grain structure during the cyclic in-plane α - β grain boundary motion resulting in in-plane grain growth, lattice defect removal, and $\{111\}$ texture increase. The Pd thin film is subjected to repeated deformation both during the loading and deloading cycle. This cyclic deformation results in irreversible texture changes. Pivak *et al.* [31] and Germaud *et al.* [64],

reported film structure evolution in terms of an enhancement of the (111) texture and an increase in crystal size resulting from hydrogen loading and deloading. We found that already after the first H-loading enhancement of the {111} texture is observed as listed in Table 5.2(b). Furthermore, the volume fraction $f_{\langle 111 \rangle}$ increased both after the hydrogen loading and deloading cycles, indicating the film's structural evolution. This increase in fiber texture can also be correlated to the morphology evolution observed in section 5.3.1., Figures 5.2 & 5.3 show hydrogen cycled Pd thin films surface with higher packing density as compared to the as-deposited state, which has low-density open morphology. In our previous works [43, 44], we have shown that closed morphology leads to a strong and sharp fiber texture, and open morphology leads to a weak and broad fiber texture. This kind of morphology and texture evolution influence both the hydrogen uptake response and mode of deformation in the Pd thin film during hydrogen cycling.

5.3.3. Stress analysis

The two methods of tilting the specimen, ω -tilt and ψ -tilt, used for in-situ diffraction stress analysis, are compared in this section.

5.3.3.1. ω -tilt stress: $\sin^2\psi$ method

Due to the low intensity, asymmetry and poor profile shape of the measured peaks during ω -tilt (see Appendix B, Figure B3), it was challenging to determine peak positions with sufficient accuracy and precision. Lattice spacings were evaluated by fitting with the Centered Center of Gravity method using threshold intensity above 40% of the maximum intensity (see Appendix B, Figure B13 and 14). This method is most suitable to find peak positions for asymmetric peaks but cannot distinguish overlapping peaks. Therefore, peak half maxima were used for iteration to avoid overlapping regions between {331} and {420} peaks. Absorption/transparency correction, background subtraction, LP correction, and $K\alpha_2$ -stripping, as intensity corrections onto the measured scans, were also applied. By fitting the {331} and {420} diffraction peaks, the central peak positions were obtained for all ψ values. The lattice spacing, d_ψ , was calculated using the conventional $\sin^2\psi$ -method [65] and plotted as a function of $\sin^2\psi$ to deduce in-plane stress, $\langle\sigma_{11}\rangle$ in Pd films, from the slope of $d_{(hkl)}$ versus $\sin^2\psi$ for Pd-{331} reflection (see Appendix B, Figure B13 and 14). Hill's weighted average grain-interaction model [65] was applied to calculate the {hkl} dependent X-ray elastic constants for the Pd film reflections. The X-ray elastic constants S_1^{hkl} and $\frac{1}{2}S_2^{hkl}$

values, used for the Pd {331} and {420} reflections, are listed in Table 5.3. ω -tilt stress measurements were corrected by subtracting ghost stress using a Pd stress-free powder.

Table 5.3 – *X-ray elastic constants for grain-interaction models derived from X'Pert Stress program, using Pd single-crystal elastic constants taken from reference [66].*

Pd reflections $\{hkl\}$	Pd		PdH _{0.66}	
	S_1^{hkl} (TPa ⁻¹)	$\frac{1}{2}S_1^{hkl}$ (TPa ⁻¹)	S_1^{hkl} (TPa ⁻¹)	$\frac{1}{2}S_1^{hkl}$ (TPa ⁻¹)
{111}	-2.16	8.24	-2.38	9.05
{200}	-4.28	14.60	-4.14	14.33
{311}	-3.28	11.60	-3.31	11.84
{331}	-2.54	9.36	-2.69	9.99
{420}	-3.25	11.54	-3.30	11.79

Table 5.4 – *{hkl} reflections and corresponding ψ -tilt angles, considered for the diffraction stress analysis of the (111)-fiber textured Pd thin films employing a combination of crystallite group method (CGM) and $\sin^2\psi$ method.*

$\{hkl\}$	Strong fiber texture	Weak fiber texture
	$\Psi(^{\circ})$	$\Psi(^{\circ})$
{111}	0, 70.5	0, 10, 20, 60, 70 and 75
{200}	54.7	40, 50, 60
{311}	29.5 and 58.5	30

5.3.3.2. ψ -tilt stress: combining crystallite group method and $\sin^2\psi$ method

In addition to crystallographic texture, the sputter-deposited columnar grain structure is responsible for macroscopic anisotropy in thin films [67]. Therefore, we present an easy approach to estimate stress in Pd thin films by combining the crystallite group method (CGM)

[68, 69] and the $\sin^2\psi$ method [65]. All individual grains of one group are considered as one single crystal, i.e., possible grain interactions due to different surroundings are neglected. We used all planes parallel to the film surface (in our case, the $\{111\}$ oriented grains parallel to the surface) picked from 2θ scans of $\{111\}$, $\{200\}$ and $\{311\}$ reflections (see Appendix B, Figure B9). The measured ψ -tilted θ - 2θ scans used for texture quantification were also employed for diffraction stress analysis.

The fiber texture plots (FTP) were used to locate $\langle 111 \rangle$ pole positions. The expected $\langle 111 \rangle$ pole maxima at $\psi = 0^\circ$ and 70.5° in the $\{111\}$ -FTP, at $\psi = 54.7^\circ$ in the $\{200\}$ -FTP, and at $\psi = 29.5^\circ$ and 58.5° in the $\{311\}$ -FTP were considered for the crystallites with $\{111\}$ planes parallel to the film surface. The measured peak position at selected ψ -tilt angles corresponding to $\{111\}$ -oriented grains were used to obtain d-spacing (d_{ψ}^{hkl}). In the case of strongly textured Pd films, d-spacing for $\{111\}$ -oriented grains in $\{hkl\}$ diffraction lines were obtained at the chosen ψ -tilt angles by interpolating data points in d-spacing vs. $\sin^2\psi$ plot (Table 5.4). For weakly textured Pd thin films, at least three ψ -tilt angles were used at each $\{111\}$ maxima from $\{111\}$ -FTP and $\{200\}$ -FTP (Table 5.4). Since $\{311\}$ -FTP did not show maxima for the $\langle 111 \rangle$ texture component, the ψ -tilt angles for $\{111\}$ -oriented grains were based on the expected position, as was observed in strong texture Pd thin film ($\psi = 29.5^\circ$).

CGM requires the conversion of measured d-spacing (of each selected plane) to values of stressed lattice constant (a_{ψ}^{hkl}) for the cubic system: $a_{\psi}^{hkl} = d_{\psi}^{hkl} \sqrt{h^2 + k^2 + l^2}$. The experimentally determined lattice strain $\varepsilon_{\psi}^{meas}$ was calculated using the measured peak position ($2\theta_{\psi}^{hkl}$), the knowledge of the strain-free lattice constant (a_0^{hkl}) and using Pd lattice constant (a_{ref}) literature value, 3.890 Å, by

$$\varepsilon_{\psi}^{meas} = (d_{\psi}^{hkl} \sqrt{h^2 + k^2 + l^2} - a_0) / a_{ref} = (a_{\psi}^{hkl} - a_0) / a_{ref} \quad (5.6)$$

For the case of macroscopically elastically anisotropic specimens, the so-called diffraction X-ray elastic constants S_1^{hkl} and $\frac{1}{2}S_2^{hkl}$ relate lattice strain ε_{ψ}^{cal} to the components of stress tensor $\langle \sigma^S \rangle$. For cubic, $\{111\}$ fiber-textured Pd films the stress state is rotationally symmetric (i.e. $\langle \sigma_{11} \rangle = \langle \sigma_{22} \rangle \equiv \langle \sigma_{||} \rangle$) and ε_{ψ}^{cal} can be obtained from [70]:

$$\varepsilon_{\psi}^{cal} = \left(2S_1^{hkl} + \frac{1}{2}S_2^{hkl} \sin^2\psi \right) \sigma_{||} \quad (5.7)$$

We used Hill's weighted average grain-interaction model to estimate the calculated strain. The unknown components of the mechanical stress were evaluated by fitting the calculated

strain ε_{ψ}^{cal} (Eq. 5.7) to the measured strain $\varepsilon_{\psi}^{meas}$ (Eq. 5.6) by the use of a least-squares minimization function:

$$\chi^2 = \sum_{i=1}^N (\varepsilon_i^{cal}(\sigma_{ll}, hkl, \psi) - \varepsilon_i^{meas}(hkl, \psi))^2 \quad (5.8)$$

The error related to the measurement of absolute peak positions and imprecise knowledge of strain-free lattice constant can be circumvented if appropriate parameters are included in the fitting of Eq. 5.8 (see Appendix B, Figure B15) [70]. Thus, the strain-free lattice constants (a_0^{hkl}) have been considered as an additional fit parameter along with stress (σ_{ll}) (see Appendix B, Table B1).

5.3.3.3. Stress results for Pd thin films

The results of stress analysis, measured during hydrogen loading and deloading cycles, are plotted in Figure 5.7. The stress values derived by applying the CGM for the {111} crystallite group are shown for Pd on Ti and Pd on PI films as a function of the loading/deloading cycles in Figure 5.7(b), while in Figure 5.7(a) stress values obtained from the conventional $\sin^2\psi$ method are plotted. Tensile and compressive stresses measured on two different diffractometers and with two different analysis methods give similar trends for stress evolution in hydrogen cycled Pd thin films.

Before the hydrogen gas introduction, the as-deposited Pd thin films are under the influence of in-plane tensile stress, indicating residual stress attributed to sputtering-deposition conditions [44]. The hydrogen loading results in both lattice expansion and a large in-plane compressive stress. The maximum compressive stress during loading cycles was found for Pd-Ti-SiO₂/Si film (max. up to -490 MPa). The large in-plane compressive stress corresponds to the occurrence of the substrate clamping effect, which suppresses the in-plane lattice expansion. This suppression causes a delay in H-uptake in Pd on Ti film along with incomplete $\alpha \rightarrow \beta$ phase transformation as the number of cycles increase (a fraction of α -phase was not transformed) (see Appendix B, Figure B6(b)). This is in agreement with a previous observation that a Ti intermediate layer slows down the kinetics of hydrogen absorption/desorption significantly [43]. For Pd-PI-SiO₂/Si film, we see a gradual increase in compressive stress with cycling, but the magnitude is almost half the stress value for Pd on Ti film. The Pd-SiO₂/Si film (without an intermediate layer) shows a decrease in compressive stress with subsequent cycling (Figure 5.7(a)). This decrease in stress is correlated to weak

cohesion between the Pd film and the substrate, due to which the film is able to provide a free surface by microcrack widening and by film debonding from the substrate (Figures 5.3 and 5.4). In nanocrystalline metal thin films, cracking and delamination contributes to the relaxation of stresses and an additional mechanism of stress relief is that of dislocation motions [71].

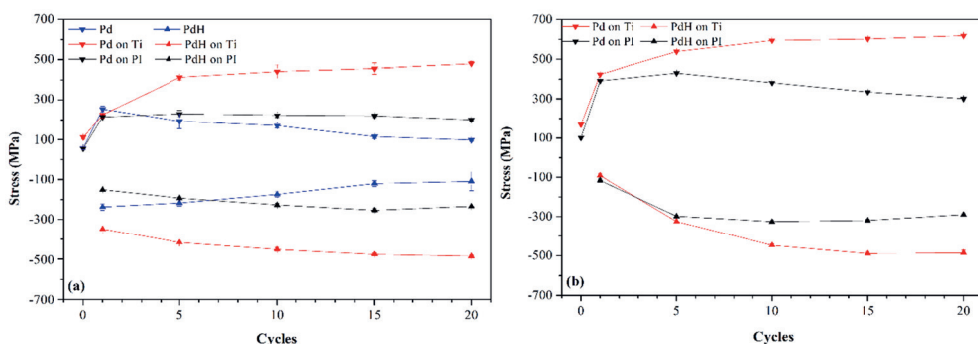


Figure 5.7 – In-situ stress vs. 20 H-L/D cycling plots (a) On D5005 system omega-stress analysis for Pd-SiO₂/Si, Pd-Ti/SiO₂/Si, and Pd-PI/SiO₂/Si films and (b) on PSI-XRD system ψ -tilt {111}-grain stress analysis for Pd-Ti/SiO₂/Si, and Pd-PI/SiO₂/Si films.

During the hydrogen deloading, the large compressive stress in the Pd film is released. After the completion of the first deloading, the stress in all Pd thin films does not return to the initial value (as-deposited) but instead exhibits a large tensile value (Figure 5.7). This also indicates that plastic deformation takes place already during the first hydrogen cycle. Note that a large increase in tensile stress is observed between as-deposited state and first deloading for all three Pd films. However, after subsequent cycles, the increase or decrease in tensile stress is small and gradual. Furthermore, for Pd on Ti film, tensile stress keeps increasing with cycling, while for Pd film without an intermediate layer, a decrease is found. For Pd on PI film, tensile stress increases up to 5-L/D cycles, and on further cycling, a gradual decrease is found, similar to Pd-SiO₂/Si film but without compromising its structural integrity. Here, we concluded that for Pd on PI film the large compliance of the polyimide substrate increase crack spacing rearrangements and distance over which stresses are relaxed in the neighborhood of a microcrack.

The overall sequence of hydrogen loading and deloading cycles (20-L/D) shows that the stress evolution behavior is different for the Pd thin-film systems, and this determines the

deformation behavior. In Pd-SiO₂/Si film, the stress relaxation is due to film debonding, while in Pd-Ti-SiO₂/Si film stress builds up due to strong film-substrate bonding. Pd-PI-SiO₂/Si film behavior is in-between the other two films but close to Pd-Ti-SiO₂/Si film. In light of morphology, texture, and stress results, the mechanisms of Pd thin film deformation based on XRD line-broadening analysis are discussed in the next section.

5.3.4. Defects from XRD line-broadening

The presence of crystallographic defects such as dislocations during the microstructural evolution in hydrogen-cycled Pd films was investigated based on the observed change in the integral breadth of diffraction profiles [72]. It is well established that the formation and decomposition of a hydride phase during two-phase transitions results in the generation of a significant dislocation density [47]. Pardoen *et al.* [46] using time-resolved TEM (HRTEM) demonstrated that the dislocation-mediated mechanism dictates the mechanical stability both during loading (deformation) and deloading (relaxation) in textured nanocrystalline Pd films. Using Bragg coherent diffractive imaging, Ulvestad *et al.* [23] imaged dislocations nucleated deep in the hydrogen-poor phase during the forward hydriding phase transformation that heal during the reverse transformation in Pd nanoparticles. We used XRD line profiles of the long overview scans from the D5005 system (section 5.2.2.4.) for the defect analysis during loading and deloading cycles. The modified Williamson-Hall (mod-WH) method was applied by analyzing the line breadths for all possible types of dislocations [44]. Based on weighted least-square fitted straight lines using the estimated standard deviations in the breadth, it is concluded that randomly oriented pure screw dislocations of the $\{111\}$, $a\langle 110 \rangle$ slip system leads to the best fit (see Appendix B, Figure B16).

In Figure 5.8 the values of crystallite size $\langle D \rangle$ and dislocation density ρ (obtained from Mod-WH plots) are compared to the previous deloading and loading cycles in steps of five. The evolution in $\langle D \rangle$ and ρ is seen during loading when Pd is in the hydrogen-rich phase (β -PdH_{0.66}) and during deloading when the film returns to the metallic phase (Pd), as in the as-deposited state. With respect to the as-deposited state, a large decrease in crystallite size is observed after 1st loading for all Pd thin films. This is followed by a gradual increase with subsequent cycling, reaching again to almost as-deposited size. While for deloading a stepwise gradual increase in crystallite size is found for all Pd thin films (Figure 5.8(a)). This suggests that, during the α -to- β phase transformation, for loading cycles the crystal size is small (Figure 5.9(a)). However, once the transformation is completed (α -to- β and β -to- α), the

crystal grows large and includes many lattice defects (Figures 5.9(a&b)). During the initial hydrogen loading cycles, the β -phase ($\text{PdH}_{0.66}$) exhibits a smaller crystal size than for the completely transformed state (Pd) (Figure 5.8(a)). However, after several cycles, the β -phase size reaches almost the same as that of the completely transformed state.

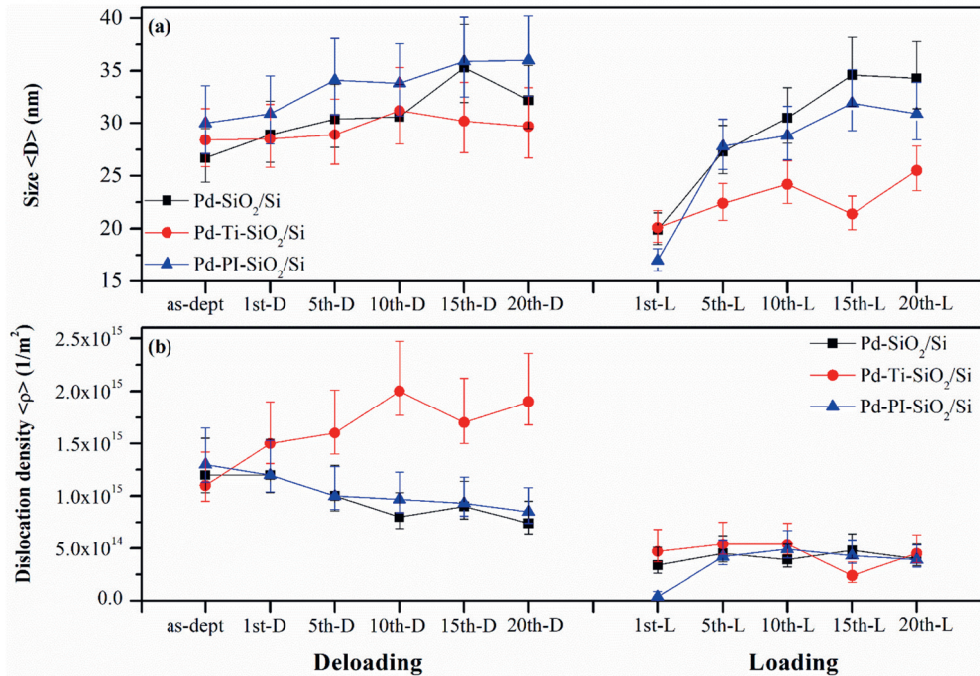


Figure 5.8 – Plots with the absolute values of the crystallite size $\langle D \rangle$ (a) and the dislocation density ρ (b) for each of the three Pd thin film systems during 20 hydrogen loading/deloading cycling (20-L/D). On the left side of the plots are Pd films in the metallic phase (Pd) and on the right side are Pd films in the hydrogen-rich phase (β -PdH_{0.66}).

A decrease in dislocation density for all Pd films was found during loading cycles relative to as-deposited and unloaded conditions. Also, the density of dislocations after loading cycles is nearly the same for all Pd films (Figure 5.8(b)). However, dislocation development differs for Pd films during deloading cycles. An increase in dislocation density upon deloading is seen for Pd on Ti film, in contrast to a gradual decrease for Pd on PI film and Pd film without an intermediate layer. The possible reason for the decrease in dislocation density for the Pd-SiO₂/Si film is through the formation of a buckled region that has two free surfaces that allow

dislocations to escape (Figures 5.4(a–c)). In Pd-PI-SiO₂/Si film, also a dislocation density decrease is observed, although no buckling occurred. Here the film and flexible intermediate layer interface explain the dislocation density decrease. The dislocations are annihilated at the crystalline-amorphous interface with the polyimide intermediate layer, which acts as a dislocation sink [73]. This suggests that the Pd-PI interface behaves like a free surface with respect to the stability of dislocations.

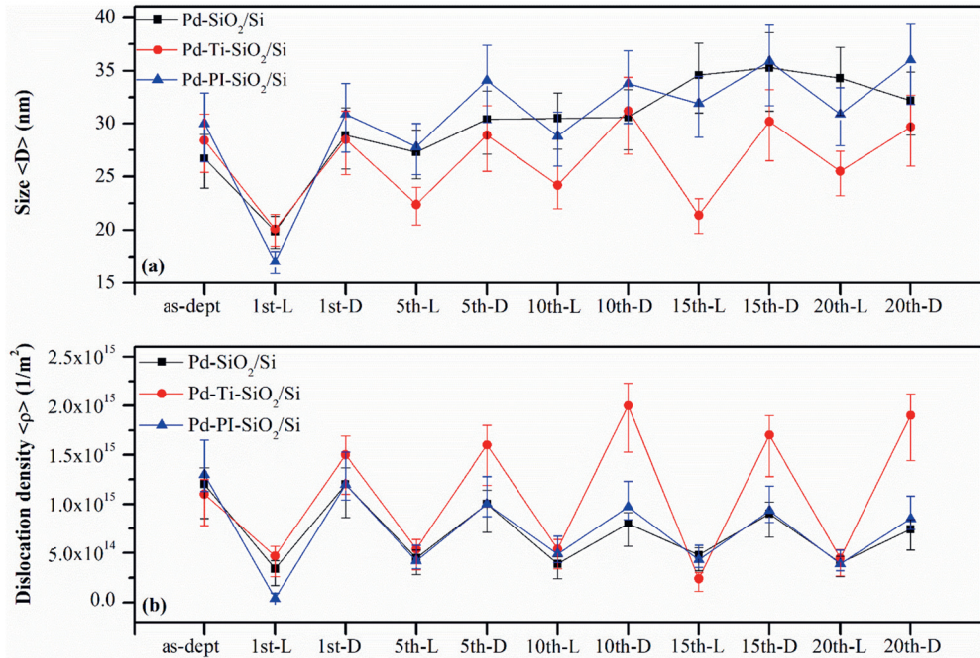


Figure 5.9 – The crystallite size $\langle D \rangle$ (a) and the dislocation density ρ (b) plots to show its cyclic behavior during 20 hydrogen loading/deloading cycling (20-L/D). During loading, films are in the hydrogen-rich phase (β -PdH_{0.66}) and during deloading films return to the metallic phase (Pd), as in the as-deposited state.

In Figure 5.9, the cyclic behavior of $\langle D \rangle$ and ρ during loading and deloading cycles is visualized. The general behavior (shapes of the plot) is the same for all three Pd films, which testifies that all Pd films contain similar kinds of defects, that differ only by their concentration. In all likelihood, the dislocations propagate and interact with pre-existing microstructure and also with each other, thus making up the final microstructure of the

deformed state. Figure 5.9(a) shows a different pattern of $\langle D \rangle$ towards the end (higher cycles) for Pd-SiO₂/Si film that can be explained by buckle formation (Figure 5.4). The cyclic evolution of crystallite size, decrease during loading and increase upon deloading confirm that the presence of GB-mediated mechanisms contributes to the relaxation process in columnar grained Pd thin films. Figure 5.9(b) shows also that during loading, when compressive stress develops, dislocation densities are reduced, and are strongly retrieved after deloading when the film is again under tensile stress. Thus, the change in residual stress from compressive to tensile increases lattice strain, resulting in high dislocation densities at the end of the loading/deloading cycle. The defect analysis shows the reversible pattern of grain growth and dislocation generation/motion when stresses change between tensile and compressive during hydrogen cycling. The correlation between stress relaxation and change in dislocation density is based on the idea that the dislocation decreases by the annihilation of dislocation at sinks (e.g. grain boundaries, microcrack or film-substrate interface). Ulvestad *et al.* [23] showed that at a certain critical size of Pd nanoparticles, dislocations are generated to relieve the stress. Further, they showed the formation and healing of structural defects in Pd nanoparticles during the $\alpha \leftrightarrow \beta$ phase transformation. A similar kind of stability and mobility of dislocation can be seen in our Pd films during cyclic phase transformations. We conclude that films with an open morphology successfully restrict internal stress from amplifying during hydrogen uptake, and thus no noticeable structural deformation occurs for films with a stable film-substrate interface.

Similar to Pd nanoparticles, Pd thin films follow similar behavior, except for the stress relaxation mode at critical stress values, which depends on film-substrate stability. The dislocation-based relaxation mechanism depends both on the generation of new dislocations and the propagation of the existing dislocations. The strengthening of thin films in terms of threading dislocations is possible when the increase in dislocation energy equals the film strain energy reduction, leading to the Nix-Freund relation [74, 75]. From a dislocation distribution point of view, on a strongly adhering substrate (Ti-SiO₂/Si), dislocation repulsions are higher at the interface than for film attached on a flexible substrate (PI-SiO₂/Si) or on to a substrate with poor adherence (SiO₂/Si). The possibility of concurrent microcracking and buckling allows delamination to occur in Pd film without the adhesive intermediate layer, while a flexible PI intermediate layer allows Pd film to “breathe” during hydrogen cycling, along with providing enhanced adhesive support to the film on the substrate.

5.4. Conclusion

In-situ X-ray diffraction study of hydrogen cycling on Pd thin films has been conducted to deduce the intermediate layer's (substrate types) influence on the morphology, preferred orientation (texture), and state of stress as a function of the film substrate types and hydrogen cycling. A simple method to estimate texture-components volume fractions in weak fiber texture Pd thin films is presented. This method can be immediately implemented to study texture evolution during hydrogen cycling. It was found that the hydrogen cycling results in an increase in $\{111\}$ -fiber texture. The diffraction stress analysis was performed by combining the $\sin^2\psi$ method and the crystallite group method (CGM) to enable the determination of stress values for macroscopically elastically anisotropic Pd thin films. The stress results show that the stress evolution during cycling is different for all three Pd thin film systems, and this determines the deformation behavior. These findings are further supported by transmission and scanning electron microscopy investigations for morphological changes and through diffraction line-broadening analysis to understand the deformation mechanism. The plastic deformation occurs both during loading and deloading in Pd film and leads to changes in the dislocation density in the final microstructure of the deformed state. Scanning electron and optical micrographs show that debonding plays a critical role in Pd-SiO₂/Si film failure mechanism. By using a flexible and adhesive intermediate layer – like with polyimide one can enhance the stability of the Pd thin films.

5.5. References

- [1] Barreto L, Makihira A, Riahi K. The hydrogen economy in the 21st century: a sustainable development scenario. *Int J Hydrogen Energ.* 2003;28:267-84 DOI: [https://doi.org/10.1016/S0360-3199\(02\)00074-5](https://doi.org/10.1016/S0360-3199(02)00074-5).
- [2] Ball M, Weeda M. The hydrogen economy–vision or reality? *Int J Hydrogen Energ.* 2015;40:7903-19 DOI: <https://doi.org/10.1016/j.ijhydene.2015.04.032>.
- [3] Abe J, Popoola A, Ajenifuja E, Popoola O. Hydrogen energy, economy and storage: review and recommendation. *Int J Hydrogen Energ.* 2019;44:15072-86 DOI: [https://doi.org/10.1016/S1369-7021\(11\)70143-2](https://doi.org/10.1016/S1369-7021(11)70143-2).
- [4] Boudart M, Hwang H. Solubility of hydrogen in small particles of palladium. *Journal of catalysis.* 1975;39:44-52 DOI: [https://doi.org/10.1016/0021-9517\(75\)90280-8](https://doi.org/10.1016/0021-9517(75)90280-8).
- [5] Flanagan TB, Oates W. The palladium-hydrogen system. *Annual Review of Materials Science.* 1991;21:269-304 DOI: <https://doi.org/10.1146/annurev.ms.21.080191.001413>.
- [6] Jewell LL, Davis BH. Review of absorption and adsorption in the hydrogen–palladium system. *Applied Catalysis A: General.* 2006;310:1-15 DOI: <https://doi.org/10.1016/j.apcata.2006.05.012>.

- [7] Griessen R, Strohfeldt N, Giessen H. Thermodynamics of the hybrid interaction of hydrogen with palladium nanoparticles. *Nature materials*. 2016;15:311-7 DOI: <https://doi.org/10.1038/nmat4480>.
- [8] Harumoto T, Nakamura Y, Shi J. Correlation among hydrogenation, magnetoelastic coupling, magnetic anisotropy, and magnetoresistance in magnetostrictive, hydrogen-absorbing palladium-cobalt alloy films for hydrogen sensing. *Int J Hydrogen Energ*. 2021;46:30204-15 DOI: <https://doi.org/10.1016/j.ijhydene.2021.06.163>.
- [9] Sousanis A, Biskos G. Thin Film and Nanostructured Pd-Based Materials for Optical H₂ Sensors: A Review. *Nanomaterials*. 2021;11:3100 DOI: <https://doi.org/10.3390/nano11113100>.
- [10] Westerwaal R, Den Besten C, Slaman M, Dam B, Nanu D, Böttger A, et al. High throughput screening of Pd-alloys for H₂ separation membranes studied by hydrogenography and CVM. *Int J Hydrogen Energ*. 2011;36:1074-82 DOI: <https://doi.org/10.1016/j.ijhydene.2010.10.014>.
- [11] Nayeibossadri S, Speight JD, Book D. Hydrogen separation from blended natural gas and hydrogen by Pd-based membranes. *Int J Hydrogen Energ*. 2019;44:29092-9 DOI: <https://doi.org/10.1016/j.ijhydene.2019.03.044>.
- [12] Narehood D, Kishore S, Goto H, Adair J, Nelson J, Gutierrez H, et al. X-ray diffraction and H-storage in ultra-small palladium particles. *Int J Hydrogen Energ*. 2009;34:952-60 DOI: <https://doi.org/10.1016/j.ijhydene.2008.10.080>.
- [13] Li G, Kobayashi H, Taylor JM, Ikeda R, Kubota Y, Kato K, et al. Hydrogen storage in Pd nanocrystals covered with a metal-organic framework. *Nature materials*. 2014;13:802-6 DOI: <https://doi.org/10.1038/nmat4030>.
- [14] Manchester F, San-Martin A, Pitre J. The H-Pd (hydrogen-palladium) system. *Journal of phase equilibria*. 1994;15:62-83.
- [15] Conrad H, Ertl G, Latta E. Adsorption of hydrogen on palladium single crystal surfaces. *Surf Sci*. 1974;41:435-46 DOI: [https://doi.org/10.1016/0039-6028\(74\)90060-0](https://doi.org/10.1016/0039-6028(74)90060-0).
- [16] Schneemann A, White JL, Kang S, Jeong S, Wan LF, Cho ES, et al. Nanostructured metal hydrides for hydrogen storage. *Chemical reviews*. 2018;118:10775-839 DOI: <https://doi.org/10.1021/acs.chemrev.8b00313>.
- [17] Callini E, Aguey-Zinsou K-F, Ahuja R, Ares JR, Bals S, Biliškov N, et al. Nanostructured materials for solid-state hydrogen storage: A review of the achievement of COST Action MP1103. *Int J Hydrogen Energ*. 2016;41:14404-28 DOI: <https://doi.org/10.1016/j.ijhydene.2016.04.025>.
- [18] Bardhan R, Hedges LO, Pint CL, Javey A, Whitlam S, Urban JJ. Uncovering the intrinsic size dependence of hydriding phase transformations in nanocrystals. *Nature materials*. 2013;12:905-12 DOI: <https://doi.org/10.1038/nmat3716>.
- [19] Sengar SK, Mehta B, Kulriya P. Temperature, pressure, and size dependence of Pd-H interaction in size selected Pd-Ag and Pd-Cu alloy nanoparticles: In-situ X-ray diffraction studies. *Journal of Applied Physics*. 2014;115:114308 DOI: <https://doi.org/10.1063/1.4868903>.
- [20] Eastman J, Thompson L, Kestel B. Narrowing of the palladium-hydrogen miscibility gap in nanocrystalline palladium. *Physical Review B*. 1993;48:84 DOI: <https://doi.org/10.1103/PhysRevB.48.84>.
- [21] Hakamada M, Nakano H, Furukawa T, Takahashi M, Mabuchi M. Hydrogen storage properties of nanoporous palladium fabricated by dealloying. *The Journal of Physical Chemistry C*. 2010;114:868-73 DOI: <https://doi.org/10.1021/jp909479m>.
- [22] Narayan TC, Hayee F, Baldi A, Koh AL, Sinclair R, Dionne JA. Direct visualization of hydrogen absorption dynamics in individual palladium nanoparticles. *Nature communications*. 2017;8:14020 DOI: <https://doi.org/10.1038/ncomms14020>.

- [23] Ulvestad A, Yau A. The self-healing of defects induced by the hydriding phase transformation in palladium nanoparticles. *Nature communications*. 2017;8:1-6 DOI: <https://doi.org/10.1038/s41467-017-01548-7>.
- [24] Pundt A, Kirchheim R. Hydrogen in metals: microstructural aspects. *Annu Rev Mater Res*. 2006;36:555-608 DOI: <https://doi.org/10.1146/annurev.matsci.36.090804.094451>.
- [25] Vlček M, Lukáč F, Vlach M, Wagner S, Uchida H, Baehtz C, et al. Influence of microstructure and mechanical stress on behavior of hydrogen in 500nm Pd films. *J Alloy Compd*. 2015;645:S446-S9 DOI: <https://doi.org/10.1016/j.jallcom.2014.12.086>.
- [26] Okolo B, Lamparter P, Welzel U, Wagner T, Mittermeijer E. The effect of deposition parameters and substrate surface condition on texture, morphology and stress in magnetron-sputter-deposited Cu thin films. *Thin Solid Films*. 2005;474:50-63 DOI: <https://doi.org/10.1016/j.tsf.2004.08.006>.
- [27] Thompson CV. Structure evolution during processing of polycrystalline films. *Annual review of materials science*. 2000;30:159-90 DOI: <https://doi.org/10.1146/annurev.matsci.30.1.159>.
- [28] Cortie M. Calculation of texture volume fractions by integration and gaussian fitting. *Textures and Microstructures*. 1997;29:155-84 DOI: <https://doi.org/10.1155/TSM.29.155>.
- [29] Wagner S, Pundt A. Combined impact of microstructure and mechanical stress on the electrical resistivity of PdHc thin films. *Acta Materialia*. 2011;59:1862-70 DOI: <https://doi.org/10.1016/j.actamat.2010.11.052>.
- [30] Delmelle R, Amin-Ahmadi B, Sinnaeve M, Idrissi H, Pardoën T, Schryvers D, et al. Effect of structural defects on the hydriding kinetics of nanocrystalline Pd thin films. *Int J Hydrogen Energy*. 2015;40:7335-47 DOI: <https://doi.org/10.1016/j.ijhydene.2015.04.017>.
- [31] Pivak Y, Schreuders H, Slaman M, Griessen R, Dam B. Thermodynamics, stress release and hysteresis behavior in highly adhesive Pd-H films. *Int J Hydrogen Energy*. 2011;36:4056-67 DOI: <https://doi.org/10.1016/j.ijhydene.2010.12.063>.
- [32] Vlček M, Lukáč F, Vlach M, Procházka I, Wagner S, Uchida H, et al. Hydrogen-Induced Buckling of Pd Films Deposited on Various Substrates. *Defect and Diffusion Forum*. 2015;365:55-62 DOI: 10.4028/www.scientific.net/DDF.365.55.
- [33] Li T, Suo Z. Ductility of thin metal films on polymer substrates modulated by interfacial adhesion. *International Journal of Solids and Structures*. 2007;44:1696-705 DOI: <https://doi.org/10.1016/j.ijsolstr.2006.07.022>.
- [34] Abadias G, Chason E, Keckes J, Sebastiani M, Thompson GB, Barthel E, et al. Stress in thin films and coatings: Current status, challenges, and prospects. *Journal of Vacuum Science & Technology A: Vacuum, Surfaces, and Films*. 2018;36:020801 DOI: <https://doi.org/10.1116/1.5011790>.
- [35] Welzel U, Mittermeijer EJ. Diffraction stress analysis of macroscopically elastically anisotropic specimens: On the concepts of diffraction elastic constants and stress factors. *Journal of Applied Physics*. 2003;93:9001-11 DOI: <https://doi.org/10.1063/1.1569662>.
- [36] Van Leeuwen M, Kamminga J-D, Mittermeijer E. Diffraction stress analysis of thin films: Modeling and experimental evaluation of elastic constants and grain interaction. *Journal of Applied Physics*. 1999;86:1904-14 DOI: <https://doi.org/10.1063/1.370986>.
- [37] Welzel U, Mittermeijer EJ. Applicability of the crystallite group method to fibre textured specimens. *Materials Science Forum: Trans Tech Publ*; 2004. p. 131-6 DOI: <https://doi.org/10.4028/www.scientific.net/MSF.443-444.131>.
- [38] Liu Y, Wang C, Tan H. Growth from buckling to buckling-driven delamination in a film/substrate system. *Composite Structures*. 2017;174:292-300 DOI: <https://doi.org/10.1016/j.compstruct.2017.04.062>.
- [39] Xia ZC, Hutchinson JW. Crack patterns in thin films. *Journal of the Mechanics and Physics of Solids*. 2000;48:1107-31 DOI: [https://doi.org/10.1016/S0022-5096\(99\)00081-2](https://doi.org/10.1016/S0022-5096(99)00081-2).

- [40] Liu D, Pons DJ. Crack propagation mechanisms for creep fatigue: a consolidated explanation of fundamental behaviours from initiation to failure. *Metals*. 2018;8:623 DOI: <https://doi.org/10.3390/met8080623>.
- [41] Lee J, Shim W, Lee E, Noh JS, Lee W. Highly mobile palladium thin films on an elastomeric substrate: Nanogap-based hydrogen gas sensors. *Angewandte Chemie International Edition*. 2011;50:5301-5 DOI: <https://doi.org/10.1002/anie.201100054>.
- [42] Lu N, Wang X, Suo Z, Vlassak J. Metal films on polymer substrates stretched beyond 50%. *Applied Physics Letters*. 2007;91:221909 DOI: <https://doi.org/10.1063/1.2817234>.
- [43] Verma N, Krishnamurthy G, Tichelaar FD, Böttger AJ. Controlling morphology and texture of sputter-deposited Pd films by tuning the surface topography of the (Ti) adhesive layer. *Surface and Coatings Technology*. 2019;359:24-34 DOI: <https://doi.org/10.1016/j.surfcoat.2018.12.053>.
- [44] Verma N, Delhez R, van der Pers NM, Tichelaar FD, Böttger AJ. The role of the substrate on the mechanical and thermal stability of Pd thin films during hydrogen (de)sorption. *Int J Hydrogen Energ*. 2020;46:4137-53 DOI: <https://doi.org/10.1016/j.ijhydene.2020.10.163>.
- [45] Flanagan TB, Bowerman B, Biehl G. Hysteresis in metal/hydrogen systems. *Scripta Metallurgica*. 1980;14:443-7 DOI: [https://doi.org/10.1016/0036-9748\(80\)90342-7](https://doi.org/10.1016/0036-9748(80)90342-7).
- [46] Colla MS, Amin-Ahmadi B, Idrissi H, Malet L, Godet S, Raskin JP, et al. Dislocation-mediated relaxation in nanograined columnar palladium films revealed by on-chip time-resolved HRTEM testing. *Nat Commun*. 2015;6:5922 DOI: <https://doi.org/10.1038/ncomms6922>.
- [47] Amin-Ahmadi B, Connétable D, Fivel M, Tanguy D, Delmelle R, Turner S, et al. Dislocation/hydrogen interaction mechanisms in hydrided nanocrystalline palladium films. *Acta Materialia*. 2016;111:253-61 DOI: <https://doi.org/10.1016/j.actamat.2016.03.054>.
- [48] SRM660a; lanthanum hexaboride powder line position and line shape standard for powder diffraction. Certificate, National Institute of Standards and Technology, US Department of Commerce: Gaithersburg, MD, USA. 2000 DOI: <https://www.nist.gov/srm>.
- [49] DIFFRAC.EVA. Bruker AXS Software, Karlsruhe, Germany. 2001 DOI: <https://www.bruker.com/>.
- [50] Scardi P, Leoni M, Dong Y. Texture determination in highly stressed PVD thin films. *Advances in X-ray Analysis*. 2000;42:492-501.
- [51] Welzel U, Leoni M. Use of polycapillary X-ray lenses in the X-ray diffraction measurement of texture. *Journal of applied crystallography*. 2002;35:196-206 DOI: <https://doi.org/10.1107/S0021889802000481>.
- [52] PANalytical X'Pert Stress Plus. PANalytical, Almelo, The Netherlands. 2012 DOI: <https://www.malvernpanalytical.com/>.
- [53] Scardi P, Leoni M, Delhez R. Line broadening analysis using integral breadth methods: a critical review. *Journal of applied crystallography*. 2004;37:381-90 DOI: <https://doi.org/10.1107/S0021889804004583>.
- [54] Velterop L, Delhez R, Keijser THd, Mittemeijer E, Reefman D. X-ray diffraction analysis of stacking and twin faults in fcc metals: a revision and allowance for texture and non-uniform fault probabilities. *Journal of applied crystallography*. 2000;33:296-306 DOI: <https://doi.org/10.1107/S0021889800000133>.
- [55] Williamson G, Hall W. X-ray line broadening from fcc aluminium and wolfram. *Acta metallurgica*. 1953;1:22-31 DOI: [https://doi.org/10.1016/0001-6160\(53\)90006-6](https://doi.org/10.1016/0001-6160(53)90006-6).
- [56] Ungár T, Dragomir I, Révész Á, Borbély A. The contrast factors of dislocations in cubic crystals: the dislocation model of strain anisotropy in practice. *Journal of applied crystallography*. 1999;32:992-1002 DOI: <https://doi.org/10.1107/S0021889899009334>.
- [57] Gubicza J. X-ray line profile analysis in materials science. Hershey, Pennsylvania :: Engineering Science Reference; 2014 DOI: <http://doi:10.4018/978-1-4666-5852-3>.

- [58] Verma N, Böttger AJ. Stress development and adhesion in hydrogenated nano-columnar Pd and Pd/Ti ultra-thin films. *Advanced Materials Research*. 2014;996 DOI: <https://doi.org/10.4028/www.scientific.net/AMR.996.872>.
- [59] Liu D, Pons D. Crack propagation mechanisms for creep fatigue: A consolidated explanation of fundamental behaviours from initiation to failure. *Metals*. 2018;8:623 DOI: <https://doi.org/10.3390/met8080623>.
- [60] Shamsutdinov N, Böttger A, Thijsse B. Grain coalescence and its effect on stress and elasticity in nanocrystalline metal films. *Acta materialia*. 2007;55:777-84 DOI: <https://doi.org/10.1016/j.actamat.2006.07.004>.
- [61] Li T, Huang Z, Xi Z, Lacour SP, Wagner S, Suo Z. Delocalizing strain in a thin metal film on a polymer substrate. *Mechanics of Materials*. 2005;37:261-73 DOI: <https://doi.org/10.1016/j.mechmat.2004.02.002>.
- [62] Hendriks M. X-ray Diffraction Study of Polycrystalline Silicon Layers. 1985 DOI: <http://resolver.tudelft.nl/uuid:b62d5d7f-b6fb-4f73-a880-a3c027d8ef9d>.
- [63] Harumoto T, Ohnishi Y, Nishio K, Ishiguro T, Shi J, Nakamura Y. In-situ X-ray diffraction study of hydrogen absorption and desorption processes in Pd thin films: Hydrogen composition dependent anisotropic expansion and its quantitative description. *AIP Advances*. 2017;7:065108 DOI: <https://doi.org/10.1063/1.4986214>.
- [64] Gremaud R, Gonzalez-Silveira M, Pivak Y, De Man S, Slaman M, Schreuders H, et al. Hydrogenography of PdH_x thin films: Influence of H-induced stress relaxation processes. *Acta Materialia*. 2009;57:1209-19 DOI: <https://doi.org/10.1016/j.actamat.2008.11.016>.
- [65] Hauk V. Structural and residual stress analysis by nondestructive methods: Evaluation-Application-Assessment: Elsevier; 1997.
- [66] Hsu D, Leisure R. Elastic constants of palladium and β -phase palladium hydride between 4 and 300 K. *Physical Review B*. 1979;20:1339-44 DOI: <https://doi.org/10.1103/PhysRevB.20.1339>.
- [67] Welzel U, Mittemeijer EJ. Diffraction stress analysis of macroscopically elastically anisotropic specimens: On the concepts of diffraction elastic constants and stress factors. *Journal of Applied Physics*. 2003;93:9001 DOI: <https://doi.org/10.1063/1.1569662>.
- [68] Gergaud P, Labat S, Thomas O. Limits of validity of the crystallite group method in stress determination of thin film structures. *Thin Solid Films*. 1998;319:9-15 DOI: [https://doi.org/10.1016/S0040-6090\(97\)01100-0](https://doi.org/10.1016/S0040-6090(97)01100-0).
- [69] Faurie D, Renault P-O, Le Bourhis E, Goudeau P. Study of texture effect on elastic properties of Au thin films by X-ray diffraction and in situ tensile testing. *Acta Materialia*. 2006;54:4503-13 DOI: <https://doi.org/10.1016/j.actamat.2006.05.036>.
- [70] Welzel U, Leoni M, Mittemeijer E. The determination of stresses in thin films; modelling elastic grain interaction. *Philosophical magazine*. 2003;83:603-30 DOI: <https://doi.org/10.1080/0141861021000042299>.
- [71] Thouless M. Modeling the development and relaxation of stresses in films. *Annual Review of Materials Science*. 1995;25:69-96.
- [72] Delhez R, De Keijser TH, Mittemeijer E. Determination of crystallite size and lattice distortions through X-ray diffraction line profile analysis. *Fresenius' Zeitschrift für analytische Chemie*. 1982;312:1-16 DOI: <https://doi.org/10.1007/BF00482725>.
- [73] Legros M, Cabié M, Gianola DS. In situ deformation of thin films on substrates. *Microscopy research and technique*. 2009;72:270-83 DOI: <https://doi.org/10.1002/jemt.20680>.
- [74] Nix WD. Mechanical properties of thin films. *Metallurgical transactions A*. 1989;20:2217-45 DOI: <https://doi.org/10.1007/BF02666659>.
- [75] Freund L. The stability of a dislocation threading a strained layer on a substrate. *Journal of Applied Mechanics*. 1987;54:553-7 DOI: <https://doi.org/10.1115/1.3173068>.

APPENDICES

APPENDICES

APPENDIX A: Supplementary material to Chapter 3

A1. Calculation of C_{hkl} values

Tables of C_{hkl} have been published for several types of Burgers vectors and glide planes for untextured cubic materials that contain randomly distributed dislocations (see Tables 2 and 4 of [1] and Tables I, II, III, and IV of [2]). However, some of these tables contain several rather obvious mistakes and therefore, we recalculated the erroneous values using the program Anizc [3] for all types of dislocations, with the exception of randomly oriented screw dislocations with a $\langle 110 \rangle$ Burgers vector. For these dislocations, we used the simple formulas for the C_{hkl} values for published by Scardi *et al.*[4]:

$$C_{h00} = \sqrt{A_i} / 6 \dots \dots \dots (A1.1)$$

$$q = 3 - 2 / A_i \dots \dots \dots (A1.2)$$

where A_i is the Zener ratio, characteristic of elastic anisotropy (A_z in Ref. [1] and [2]).

The calculations of all other HKL contrast factors C_{hkl} is based on the formula (just as in Ref. [1] and [2]):

$$C_{hkl} = C_{h00} - C_{h00} \cdot q \cdot H \dots \dots \dots (A1.3)$$

where $H = (h^2 k^2 + h^2 l^2 + k^2 l^2) / (h^2 + k^2 + l^2)^2$ and q is a constant.

The parametrization of C_{h00} and q proposed by Ungar *et al.* [1] is superfluous when determining the “average contrast factors” for dislocation with a random orientation distribution in an untextured cubic material. Then it is simpler and quicker to use only the appropriate C_{111} and C_{h00} , because:

- 1) two small tables are required for each slip system to obtain sufficiently accurate values for C_{h00} and C_{111} ; *i.e.*, one Table for C_{h00} , for all practically possible values of A_z (see text below *eq* (A1.2); 13 values between 0 and 10) and c_{12}/c_{44} (4 values between 0 and 5) and the analogous table for C_{111} (see: Table A1).
- 2) and q can be calculated simply from:

$$q = \{(C_{111} / C_{h00}) - 1\} / 0.33333 \dots \dots \dots (A1.4)$$

Table A1 – The numbers and layout of the table(s) with Contrast Factors C_{hkl} .

This block holds for $Az < 1$									This block holds for $Az \geq 1$								
S110-111									S110-111								
No table required. Analytical solution available.									No table required. Analytical solution available.								
Az -->	0.1	0.2	0.3	0.4	0.5	0.75	1		Az -->	1	1.5	2	3	4	8	10	
S111-110 c12/c44									S111-110 c12/c44								
C_100	0.5	0.0617	0.0906	0.1147	0.1359	0.1545	0.1928	0.2222	c12/c44	0.5	0.2222	0.2642	0.2930	0.3309	0.3560	0.4161	0.4377
C_100	1	0.0618	0.0914	0.1162	0.1376	0.1563	0.1940	0.2222	c12/c44	1	0.2222	0.2621	0.2888	0.3246	0.3493	0.4129	0.4373
C_100	2	0.0622	0.0930	0.1186	0.1404	0.1590	0.1956	0.2222	c12/c44	2	0.2222	0.2591	0.2842	0.3186	0.3431	0.4113	0.4386
C_100	5	0.0636	0.0968	0.1234	0.1452	0.1633	0.1977	0.2222	c12/c44	5	0.2222	0.2560	0.2793	0.3125	0.3375	0.4112	0.4415
C_111	0.5	0.4132	0.2766	0.2096	0.1681	0.1395	0.0969	0.0741	c12/c44	0.5	0.0741	0.0514	0.0407	0.0311	0.0267	0.0202	0.0186
C_111	1	0.4120	0.2735	0.2062	0.1649	0.1370	0.0959	0.0741	c12/c44	1	0.0741	0.0522	0.0419	0.0321	0.0273	0.0197	0.0179
C_111	2	0.4103	0.2690	0.2014	0.1607	0.1337	0.0945	0.0741	c12/c44	2	0.0741	0.0536	0.0437	0.0338	0.0289	0.0206	0.0185
C_111	5	0.4073	0.2617	0.1943	0.1547	0.1292	0.0929	0.0741	c12/c44	5	0.0741	0.0554	0.0460	0.0365	0.0314	0.0226	0.0203
E110-111 c12/c44									E110-111 c12/c44								
C_100	0.5	0.0691	0.0964	0.1154	0.1302	0.1423	0.1656	0.1820	c12/c44	0.5	0.1820	0.2108	0.2328	0.2687	0.2985	0.3859	0.4178
C_100	1	0.0680	0.0938	0.1116	0.1256	0.1372	0.1603	0.1776	c12/c44	1	0.1776	0.2098	0.2356	0.2789	0.3145	0.4126	0.4456
C_100	2	0.0665	0.0902	0.1082	0.1222	0.1344	0.1602	0.1806	c12/c44	2	0.1806	0.2201	0.2523	0.3050	0.3468	0.4535	0.4868
C_100	3	0.0656	0.0897	0.1075	0.1223	0.1355	0.1641	0.1870	c12/c44	3	0.1870	0.2315	0.2673	0.3248	0.3693	0.4784	0.5115
C_111	0.5	0.4250	0.3024	0.2547	0.2293	0.2136	0.1917	0.1808	c12/c44	0.5	0.1808	0.1669	0.1590	0.1493	0.1432	0.1314	0.1286
C_111	1	0.4315	0.3095	0.2608	0.2339	0.2167	0.1913	0.1779	c12/c44	1	0.1779	0.1602	0.1503	0.1385	0.1317	0.1199	0.1175
C_111	2	0.4435	0.3231	0.2739	0.2460	0.2276	0.2001	0.1851	c12/c44	2	0.1851	0.1654	0.1546	0.1424	0.1357	0.1254	0.1234
C_111	3	0.4543	0.3353	0.2861	0.2580	0.2393	0.2108	0.1941	c12/c44	3	0.1941	0.1747	0.1635	0.1511	0.1444	0.1345	0.1327
E111-112 c12/c44									E111-112 c12/c44								
C_100	0.5	0.0600	0.0833	0.0995	0.1120	0.1222	0.1418	0.1567	c12/c44	0.5	0.1567	0.1791	0.1965	0.2231	0.2434	0.2945	0.3104
C_100	1	0.0590	0.0809	0.0962	0.1082	0.1182	0.1383	0.1544	c12/c44	1	0.1544	0.1799	0.2003	0.2315	0.2547	0.3082	0.3234
C_100	2	0.0575	0.0785	0.0939	0.1066	0.1178	0.1416	0.1615	c12/c44	2	0.1615	0.1935	0.2186	0.2553	0.2811	0.3361	0.3507
C_100	5	0.0558	0.0789	0.0979	0.1146	0.1297	0.1614	0.1870	c12/c44	5	0.1870	0.2264	0.2552	0.2952	0.3218	0.3755	0.3891
C_111	0.5	0.4052	0.3012	0.2608	0.2393	0.2260	0.2076	0.1978	c12/c44	0.5	0.1978	0.1870	0.1808	0.1737	0.1696	0.1631	0.1618
C_111	1	0.4117	0.3075	0.2657	0.2426	0.2277	0.2058	0.1934	c12/c44	1	0.1934	0.1795	0.1716	0.1631	0.1586	0.1522	0.1510
C_111	2	0.4236	0.3196	0.2765	0.2519	0.2357	0.2115	0.1979	c12/c44	2	0.1979	0.1831	0.1752	0.1673	0.1636	0.1587	0.1581
C_111	5	0.4533	0.3488	0.3038	0.2777	0.2602	0.2343	0.2199	c12/c44	5	0.2199	0.2048	0.1971	0.1897	0.1864	0.1824	0.1819
E111-110 c12/c44									E111-110 c12/c44								
C_100	0.5	0.0594	0.0817	0.0973	0.1094	0.1196	0.1401	0.1567	c12/c44	0.5	0.1567	0.1850	0.2109	0.2608	0.3101	0.4982	0.5847
C_100	1	0.0583	0.0790	0.0932	0.1046	0.1144	0.1354	0.1543	c12/c44	1	0.1543	0.1904	0.2260	0.2960	0.3637	0.6016	0.7032
C_100	2	0.0567	0.0757	0.0894	0.1010	0.1116	0.1368	0.1615	c12/c44	2	0.1615	0.2107	0.2590	0.3511	0.4351	0.7099	0.8215
C_100	5	0.0545	0.0739	0.0894	0.1038	0.1180	0.1527	0.1871	c12/c44	5	0.1871	0.2513	0.3153	0.4262	0.5228	0.8210	0.9389
C_111	0.5	0.3977	0.2987	0.2607	0.2404	0.2275	0.2088	0.1978	c12/c44	0.5	0.1978	0.1834	0.1730	0.1572	0.1452	0.1158	0.1070
C_111	1	0.4045	0.3063	0.2673	0.2454	0.2308	0.2079	0.1934	c12/c44	1	0.1934	0.1739	0.1603	0.1412	0.1283	0.1005	0.0929
C_111	2	0.4172	0.3207	0.2811	0.2579	0.2418	0.2153	0.1980	c12/c44	2	0.1980	0.1745	0.1586	0.1376	0.1236	0.0970	0.0900
C_111	5	0.4483	0.3555	0.3155	0.2906	0.2726	0.2413	0.2200	c12/c44	5	0.2200	0.1912	0.1721	0.1477	0.1325	0.1031	0.0955

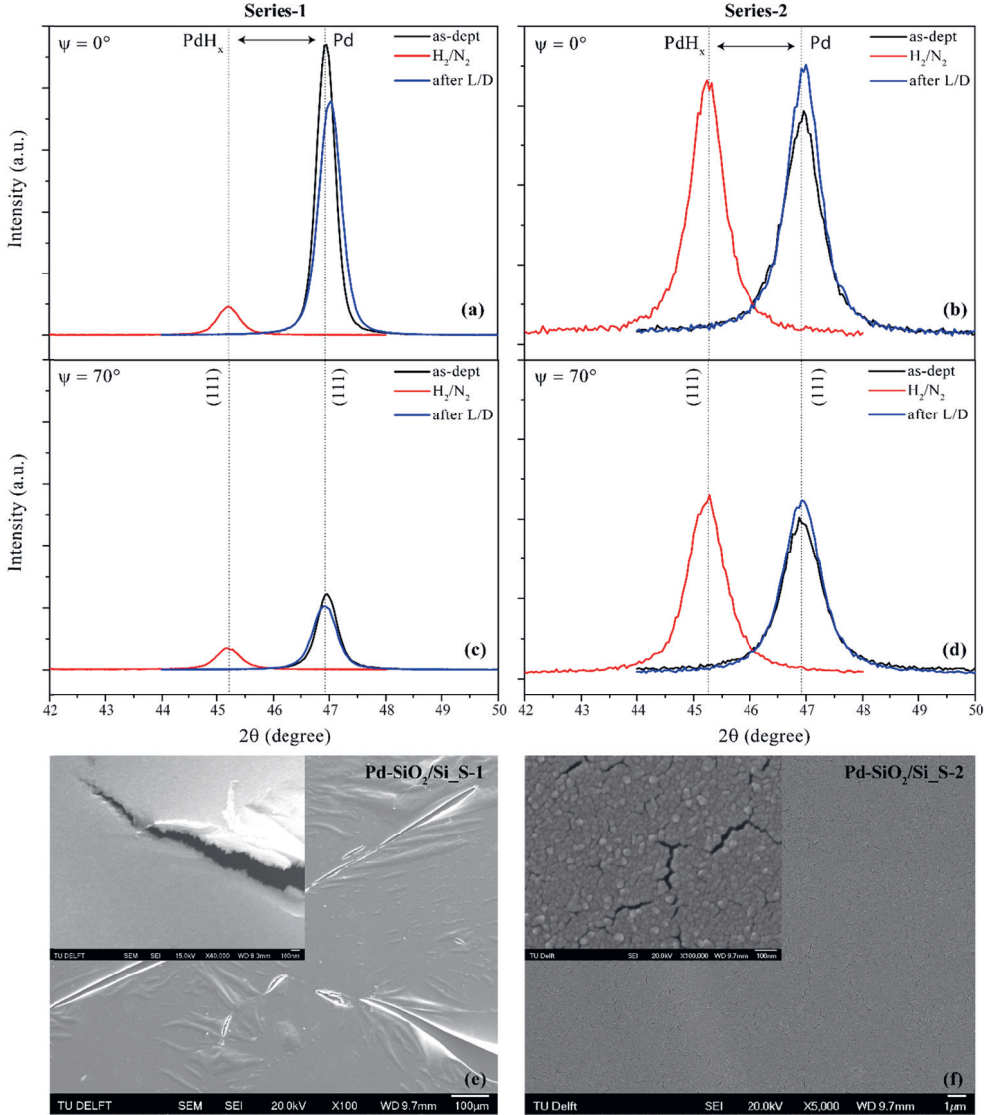


Figure A1 – Pd-SiO₂/Si films. Room-temperature in-situ XRD profiles consisting of the as-deposited film (Pd), PdH_x film in hydrogen, and film after single loading/deloading cycle (Pd). (a-d) Pd film diffraction patterns: out-of-plane 2θ line profiles at ψ=0° (a) series-1 and (b) series-2. In-plane 2θ line profiles at ψ=70° (c) series-1 and (d) series-2. (e-f) hydrogen-induced topography changes observed ex-situ by SEM images of Pd-SiO₂/Si film after loading/deloading cycle: (e) series-1 (S-1) showing scattered buckles in a large image (100 μm scale) and delaminated area in inset image (100 nm) and (f) series-2 (S-2) showing the flat surface in a large image (1 μm scale) and film in the as-deposited condition in inset image (100 nm scale).

Table A2 – Crystallite size $\langle D \rangle$ and dislocation density ρ as obtained using the modified Williamson-Hall method (mod-WH) for Pd-SiO₂/Si, Pd-Ti-SiO₂/Si and Pd-PI-SiO₂/Si series-2 films using Contrast Factors C_{hkl} for randomly oriented screw dislocations with Burgers vector $a/2\langle 110 \rangle$ and glide plane $\{111\}$ for phase transition (PT-only) and the annealing + phase transition (HT+PT) experiments.

Specimen	Experiment	Steps	Size $\langle D \rangle$ (nm)			Dislocation density $\langle \rho \rangle$ (10 ⁻¹⁴ m ⁻²)		
			-3 σ	average	+3 σ	-3 σ	average	+3 σ
Pd-SiO ₂ /Si	PT-only	as-dept	-3	17	+4	-8	21	+9
Pd-SiO ₂ /Si	PT-only	after-PT	-4	24	+5	-3	8	+4
Pd-SiO ₂ /Si	HT+PT	as-dept	-3	17	+4	-8	21	+10
Pd-SiO ₂ /Si	HT+PT	after-HT	-6	44	+8	-0.2	0.1	+0.2
Pd-SiO ₂ /Si	HT+PT	after-HT+PT	-9	45	+16	-2	6	+3
Pd-Ti-SiO ₂ /Si	PT-only	as-dept	-4	26	+7	-5	12	+6
Pd-Ti-SiO ₂ /Si	PT-only	after-PT	-6	30	+11	-7	22	+9
Pd-Ti-SiO ₂ /Si	HT+PT	as-dept	-5	30	+9	-4	11	+5
Pd-Ti-SiO ₂ /Si	HT+PT	after-HT	-4	29	+6	-1	3	+2
Pd-Ti-SiO ₂ /Si	HT+PT	after-HT+PT	-7	36	+13	-4	11	+5
Pd-PI-SiO ₂ /Si	PT-only	as-dept	-6	30	+9	-5	13	+6
Pd-PI-SiO ₂ /Si	PT-only	after-PT	-6	30	+9	-4	10	+5
Pd-PI-SiO ₂ /Si	HT+PT	as-dept	-5	28	+8	-5	0.5	+6
Pd-PI-SiO ₂ /Si	HT+PT	after-HT	-6	43	+9	-0.4	3	+0.6
Pd-PI-SiO ₂ /Si	HT+PT	after-HT+PT	-13	42	+25	-3	9	+4

References

- [1] Ungár T, Dragomir I, Révész Á, Borbély A. The contrast factors of dislocations in cubic crystals: the dislocation model of strain anisotropy in practice. Journal of applied crystallography. 1999;32:992-1002.
- [2] Dragomir I, Ungár T. The dislocations contrast factors of cubic crystals in the Zener constant range between zero and unity. Powder Diffraction. 2002;17:104-11.
- [3] Borbély A, Dragomir-Cernatescu J, Ribárik G, Ungár T. Computer program ANIZC for the calculation of diffraction contrast factors of dislocations in elastically anisotropic cubic, hexagonal and trigonal crystals. Journal of applied crystallography. 2003;36:160-2.
- [4] Scardi P. Recent advancements in Whole Powder Pattern Modelling. Zeitschrift für Kristallographie Supplements. 2008;2008:101-11.

APPENDIX B: Supplementary material to Chapter 5

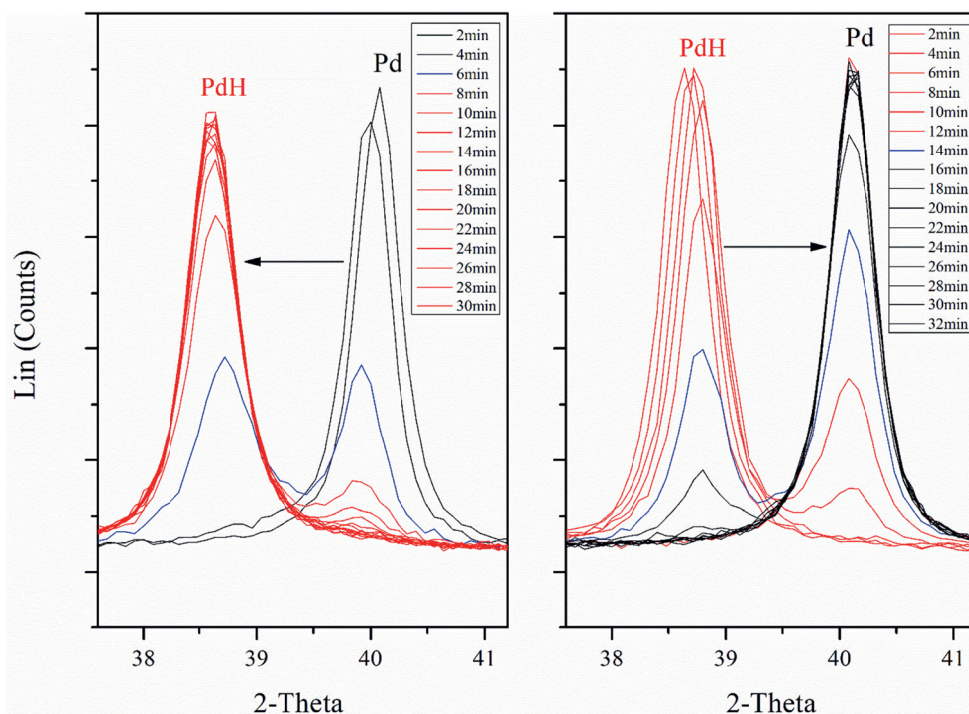


Figure B1 – Pd-{111} continuous 2 min short scans collected during hydrogen loading and deloading cycles performed on an *in-situ* XRD set-up in focusing optics diffractometer (Bruker-AXS D5005). These scans belong to Pd-PI-SiO₂/Si film: a) 1st loading loop scans and b) 1st deloading loop scans. The loop scans enabled to follow the start and finish of each transformation in time and detail.

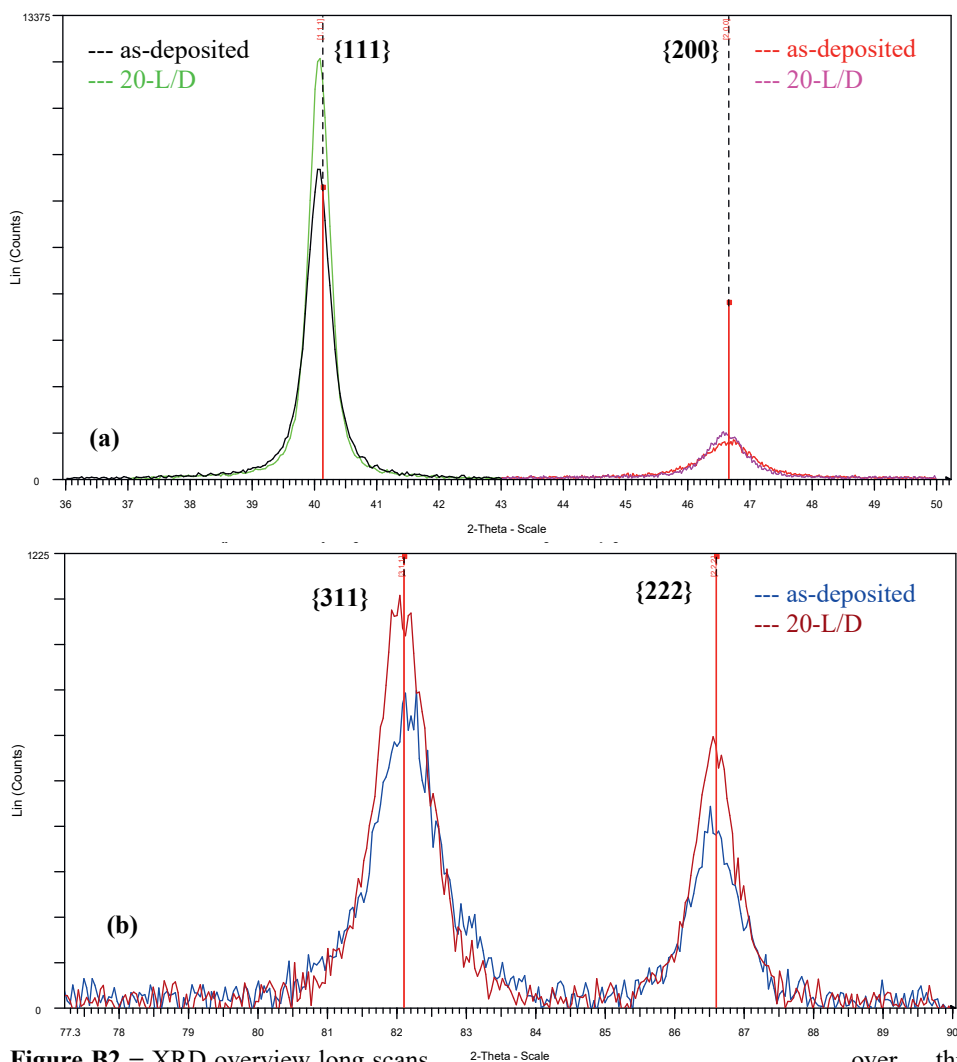


Figure B2 – XRD overview long scans over three ranges: a) 36–43° 2θ (including the Pd- $\{111\}$), 43–50° 2θ (including the Pd- $\{200\}$) and 74–90° (b) including the Pd- $\{311\}$ and $\{222\}$ reflections) monitoring change in line-width during hydrogen cycling performed on an *in-situ* XRD set-up in focusing optics diffractometer (Bruker-AXS D5005). These scans belong to Pd-SiO₂/Si film in an as-deposited state and after 20 hydrogen loading/deloading cycles (20-L/D) measured at room temperature in N₂ gas atmosphere. Such scans are used to monitor changes in line-width after hydrogen loading and deloading cycles.

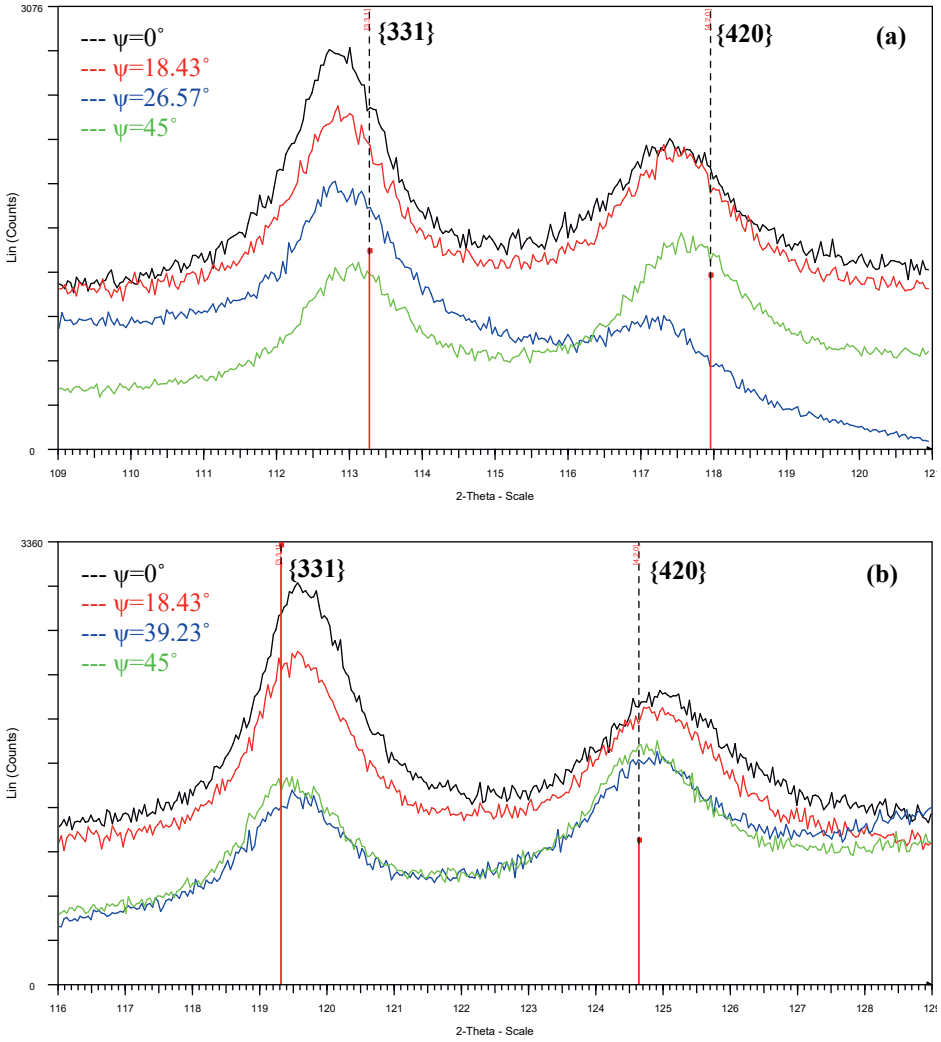


Figure B3 – ω -offset stress measurement on an *in-situ* XRD set-up in focusing optics diffractometer (Bruker-AXS D5005) for Pd- {331} & {420} reflections. The scans belong to Pd-PI-SiO₂/Si film: (a) measured at 30 °C in H₂N₂ gas atmosphere during 1st loading. Omega-offset provided for ψ -tilt angles 0°–45° in step mode ($\psi = 0^\circ, 18.43^\circ, 26.57^\circ, 45^\circ$). (b) Measured at 30 °C in N₂ gas atmosphere after 1st loading/deloading cycle. ω -offset provided for ψ -tilt angles 0°–45° in step mode ($\psi = 0^\circ, 18.43^\circ, 39.23^\circ, 45^\circ$).

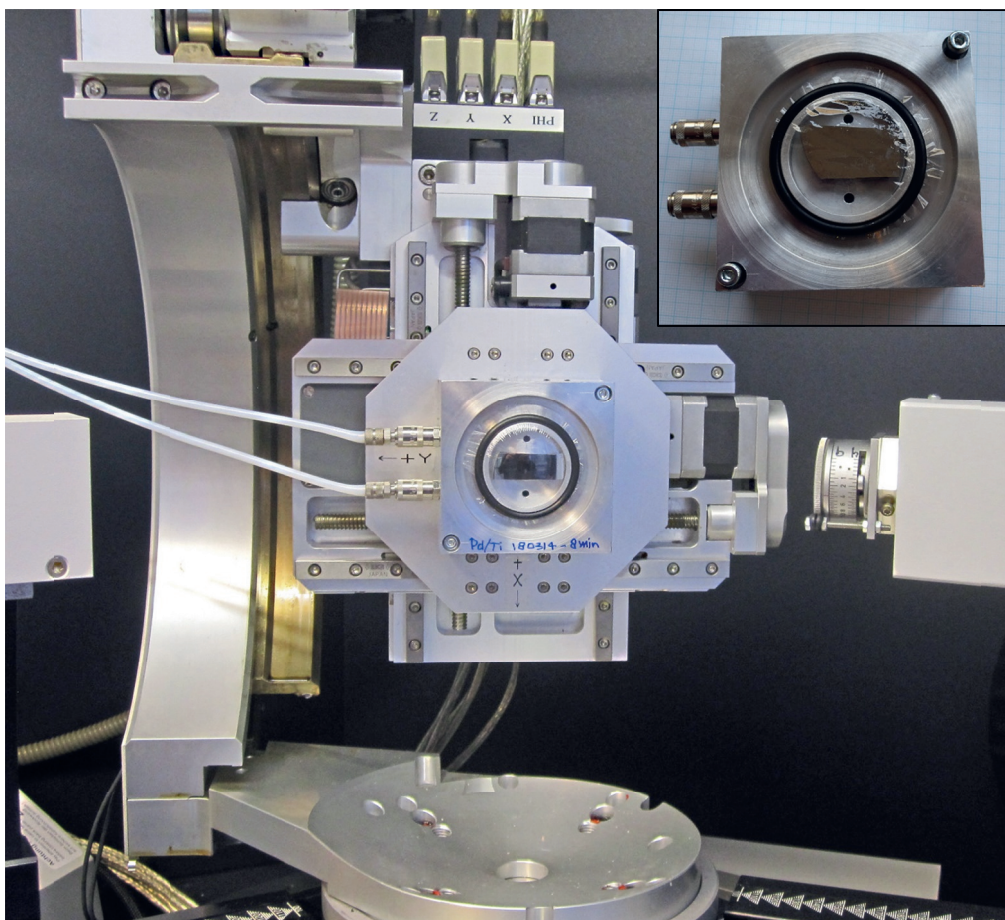


Figure B4 – *In-situ* XRD set-up: Bruker D8 diffractometer in parallel-beam optics equipped with Huber $\frac{1}{4}$ Eulerian cradle (Bruker-AXS D8). The custom-made specimen holder (in the center and top right inset) consists of a cavity covered by a transparent foil Chemplex Prolene of 4 μm thickness enabling in-situ measurements under continuous gas flow.

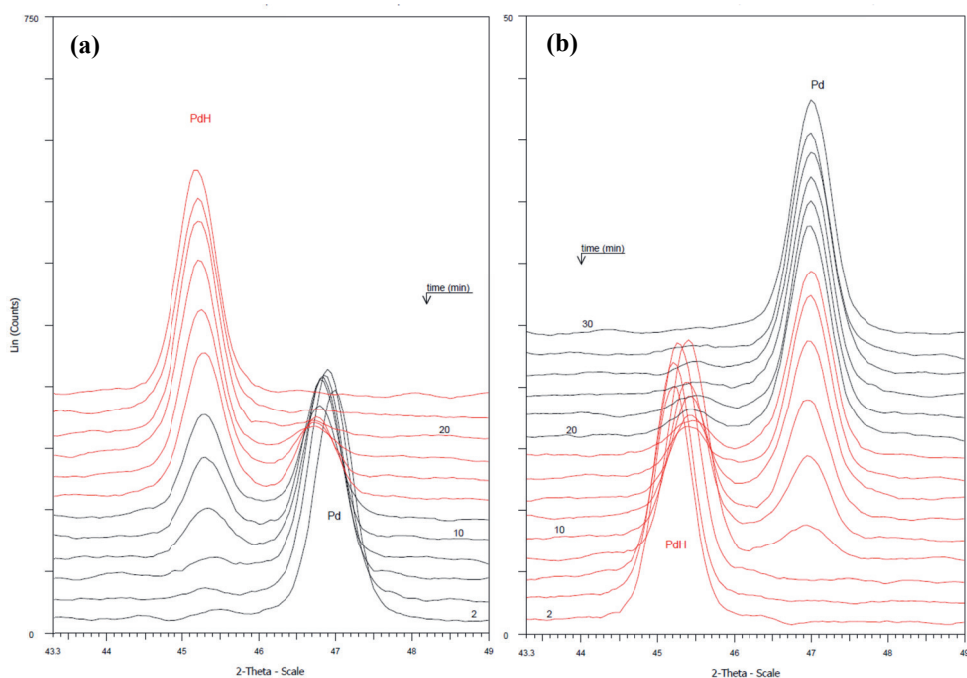


Figure B5 – Pd-{111} continuous 2 min short scans collected during hydrogen loading and deloading cycles performed on an *in-situ* XRD setup in parallel-beam diffractometer (Bruker-AXS D8). These scans belong to Pd-Pt-SiO₂/Si film: a) 20th loading loop scans and b) 20th deloading loop scans. The loop scans enabled to follow the start and finish of each transformation in time and detail.

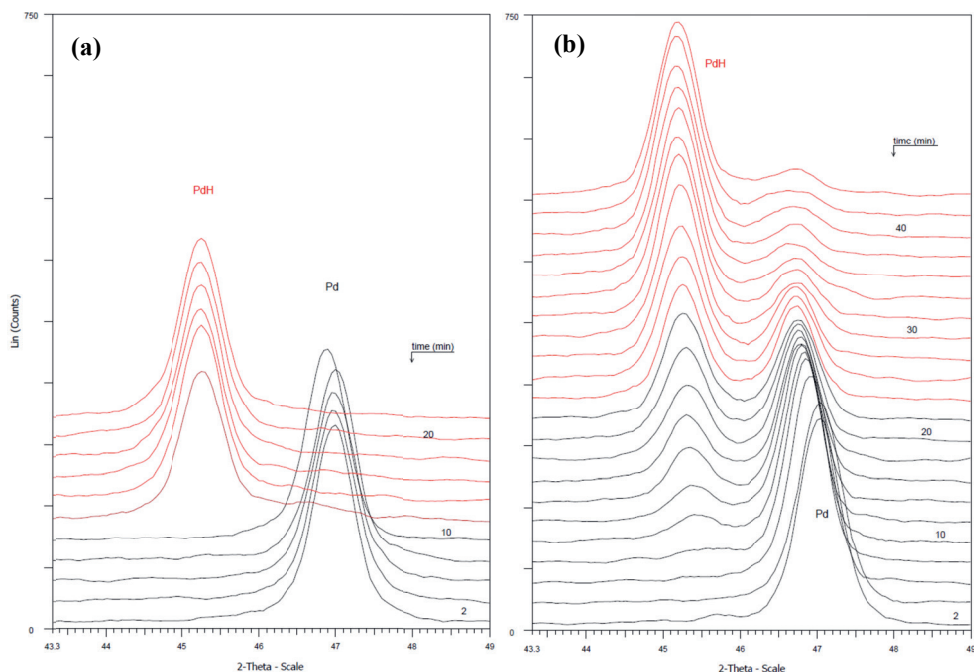


Figure B6 – Pd-{111} continuous 2 min short scans collected during hydrogen loading cycles performed on an *in-situ* XRD set-up in parallel-beam diffractometer (Bruker-AXS D8). The scans belong to Pd-Ti-SiO₂/Si film: a) 1st loading loop scans and b) 20th loading loop scans. The loop scans enabled to follow the start and finish of each transformation in time and detail.

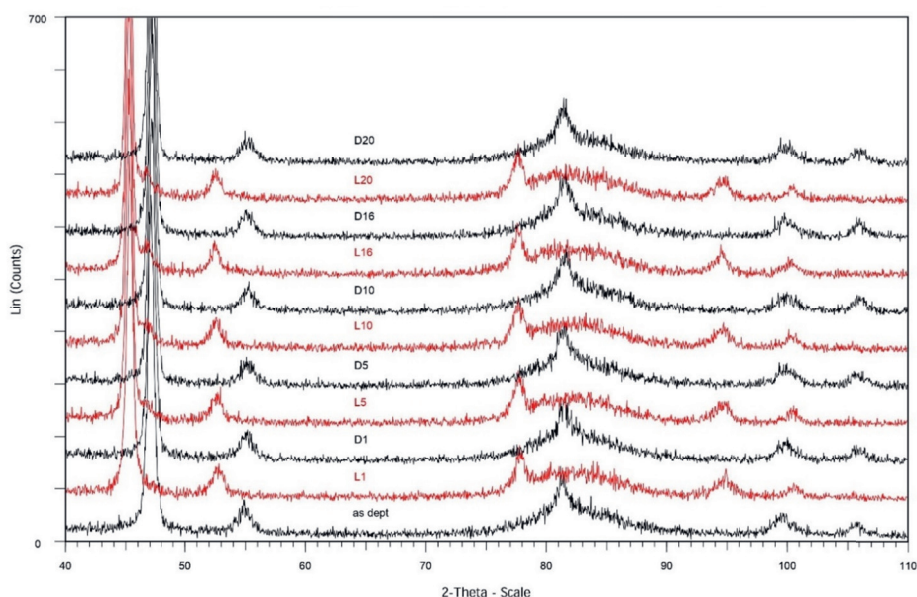


Figure B7 – XRD overview long scans for as-deposited, loading (red), and deloading (black) cycles performed on an *in-situ* XRD set-up in parallel-beam diffractometer (Bruker-AXS D8). These scans are used to monitor changes in line-width after hydrogen loading and deloading cycles. The Pd- $\{220\}$ reflection overlapping with $\{400\}$ reflection (bump in the XRD pattern) from SiO_2/Si wafer substrate is not considered for line-broadening analysis.

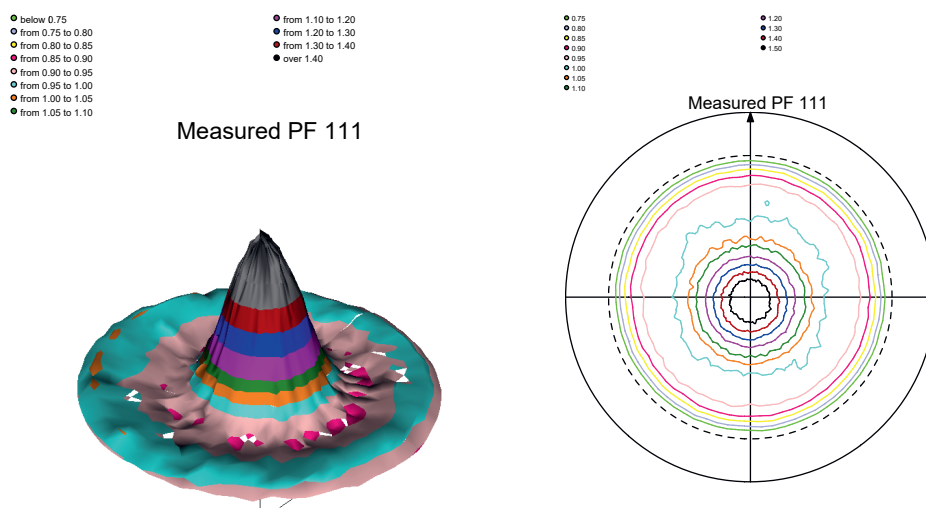
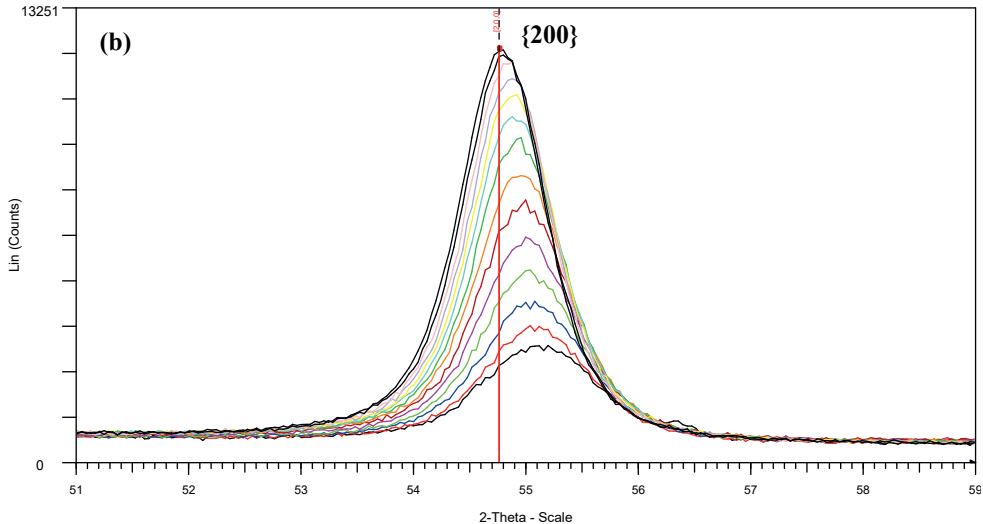
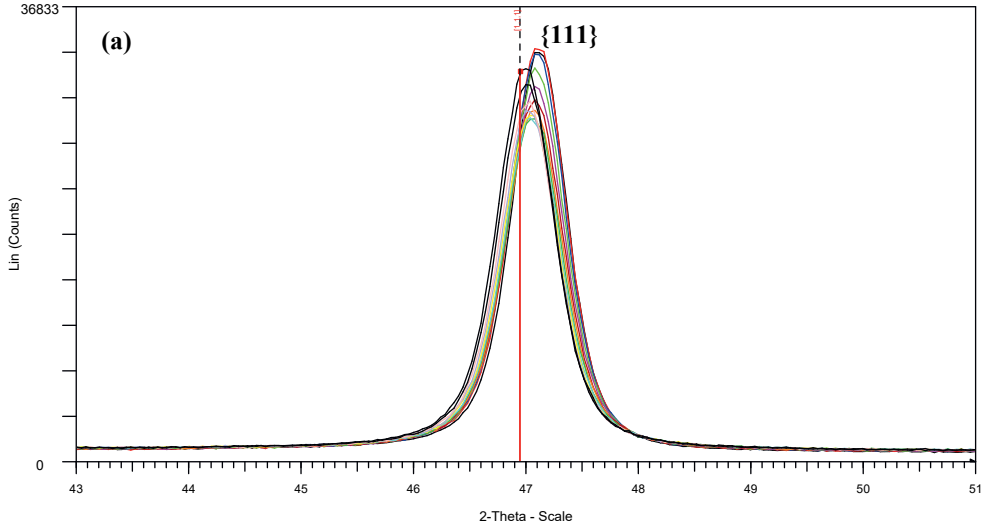


Figure 8 – 3D and 2D pole figures (111) of Pd- SiO_2/Si film in the as-deposited state showing weak fiber texture.



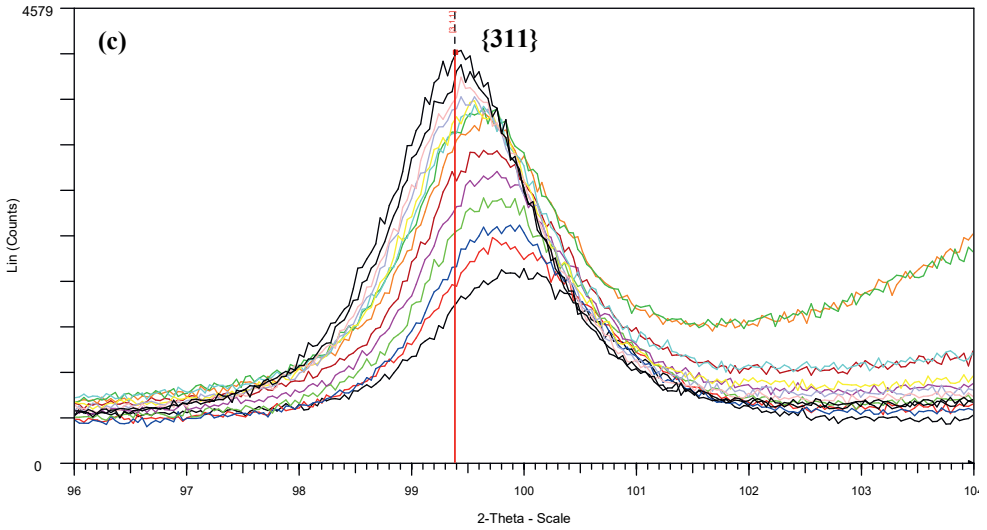


Figure B9 – Texture and stress measurements. The intensity of the diffraction lines collected over 2θ ranges that cover the whole diffraction peak: a) {111}, b) {200} and c) {311} at different sample orientations ($\psi = 0^\circ$ to 75° in steps of 5°) and at fixed rotation angle φ . The scans belong to Pd-Ti-SiO₂/Si film measured after 20 hydrogen loading/deloading cycles (20-L/D) on a parallel-beam diffractometer (Bruker-AXS D8).

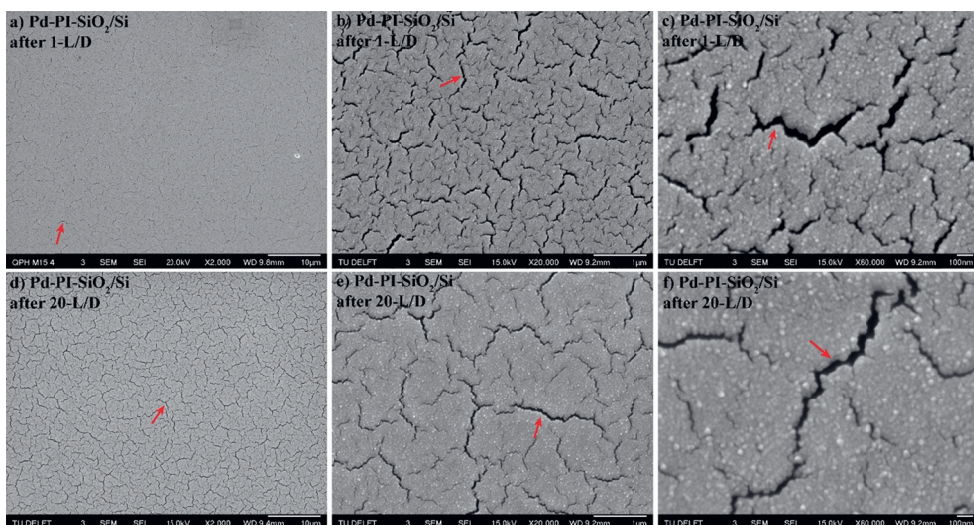


Figure B10 – Pd-PI-SiO₂/Si thin film SEM micrographs with 10 μm , 1 μm , and 100 nm magnifications from left to right illustrating the change in surface morphology: (a–c) after 1st loading/deloading cycle, and (d–f) after 20 loading/deloading cycles (20-L/D). The red arrows indicate a hydrogen-induced widening of microcracks after hydrogen cycling. Note that the micrographs were taken from two different samples: i) single hydrogen loading/deloading cycle (1-L/D) and ii) 20 hydrogen loading and deloading cycles (20-L/D)

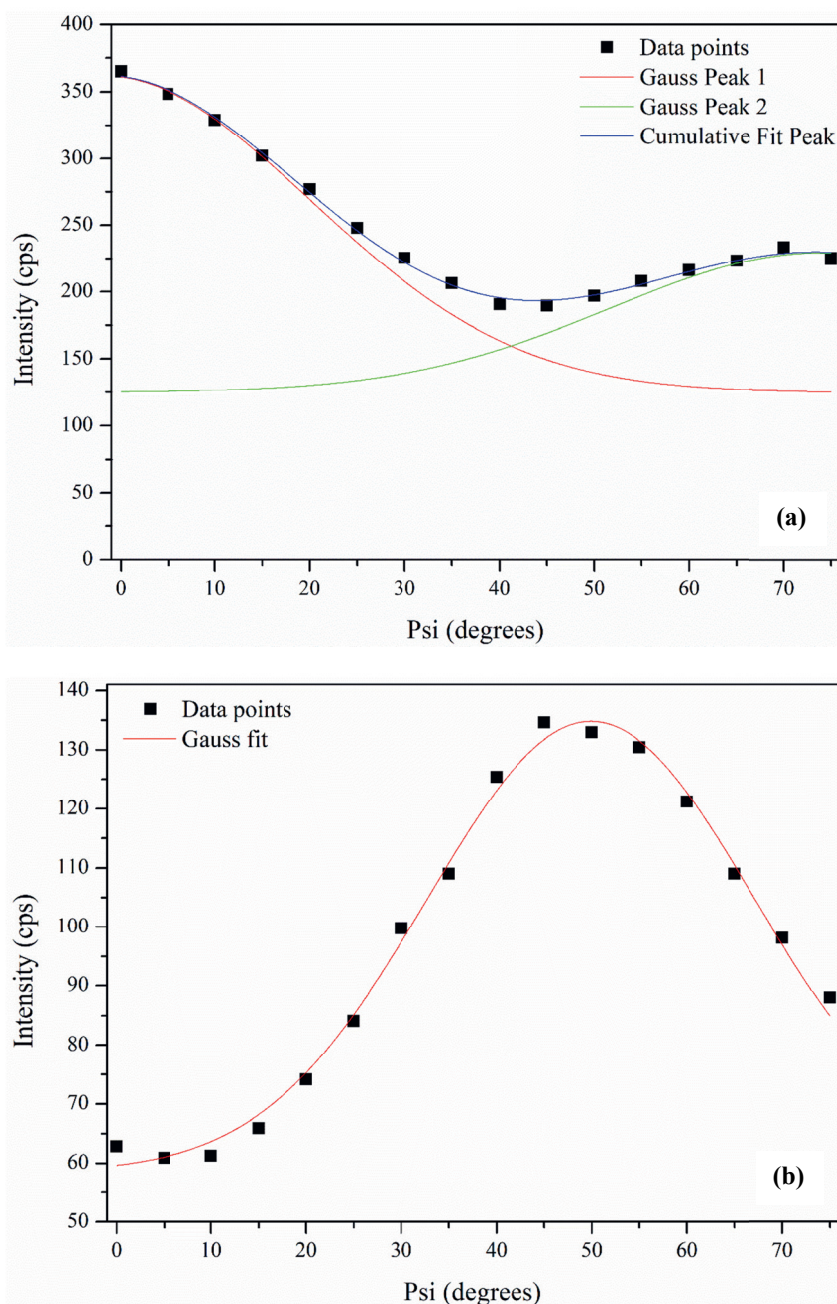


Figure B11 – Gaussian fitting of intensity vs ψ plot (Fiber texture plot) from XRD scans in Figure B9: (a) Pd-{111} and (b) Pd-{200}.

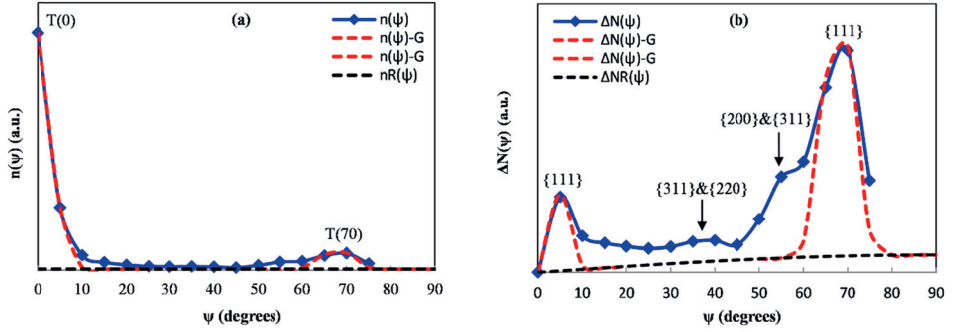


Figure B12 – Pd-SiO₂/Si thin film with strong fiber texture. (a) Pole density plot (PDP): density of {111} poles, $n(\psi)$, versus specimen tilting angle ψ . {111}-PDP displaying $\langle 111 \rangle$ fiber texture maxima at $\psi = 0^\circ$ and 70° . (b) Pole number plot (PNP): number of poles, $\Delta N(\psi)$, in {111} reflection generated from PDP in Figure B2(a). Besides major $\langle 111 \rangle$ fiber texture components other minor texture components that interfere with $\langle 111 \rangle$ volume fraction are marked in PNP.

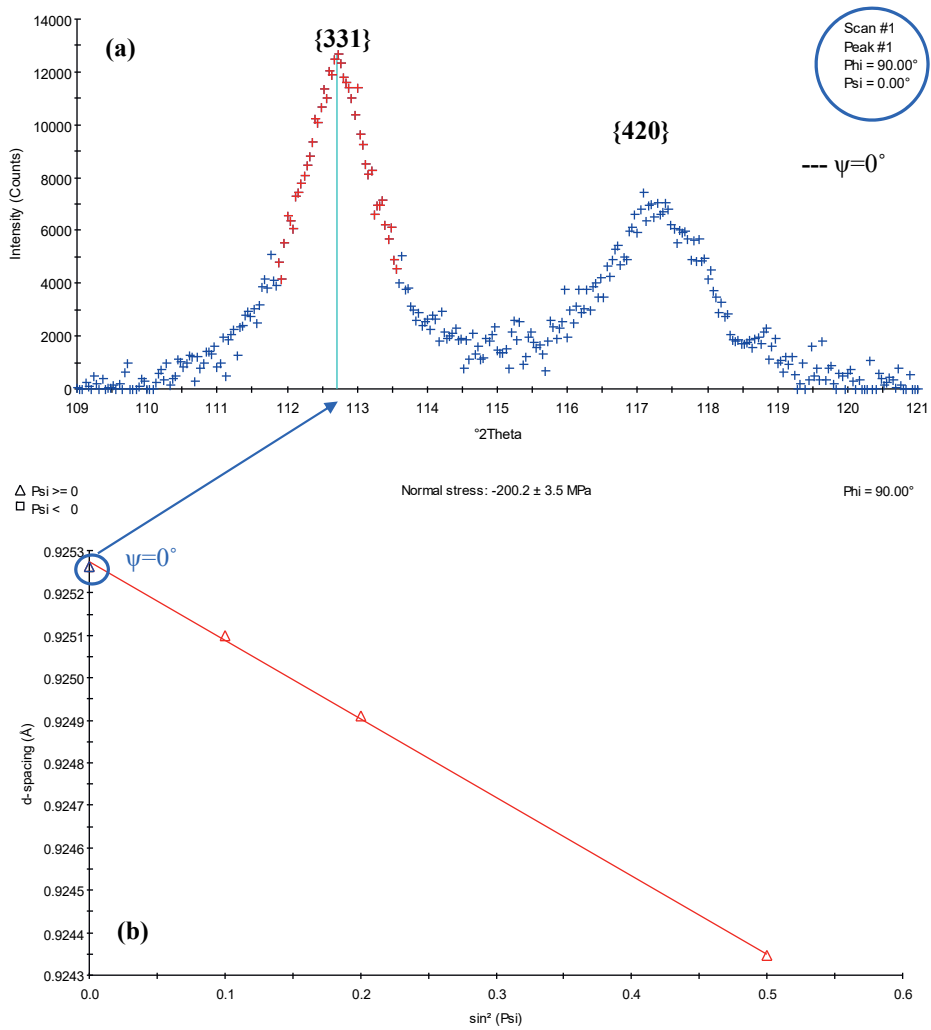


Figure B13 – Pd-PI-SiO₂/Si film omega-offset stress after 1st loading cycle. (a) From Figure B3(a) 2θ scan at $\psi=0^\circ$: lattice spacing evaluated by fitting profile with the Centered Center of Gravity method using threshold intensity above 40% of the maximum intensity. Absorption/transparency correction, background subtraction, LP correction, and $K\alpha_2$ -stripping, as intensity corrections were applied before fitting. (b) Plot of d_{hkl} vs $\sin^2\Psi$ for Pd-{331} reflection. Fittings performed on the X’Pert Stress Plus software package.

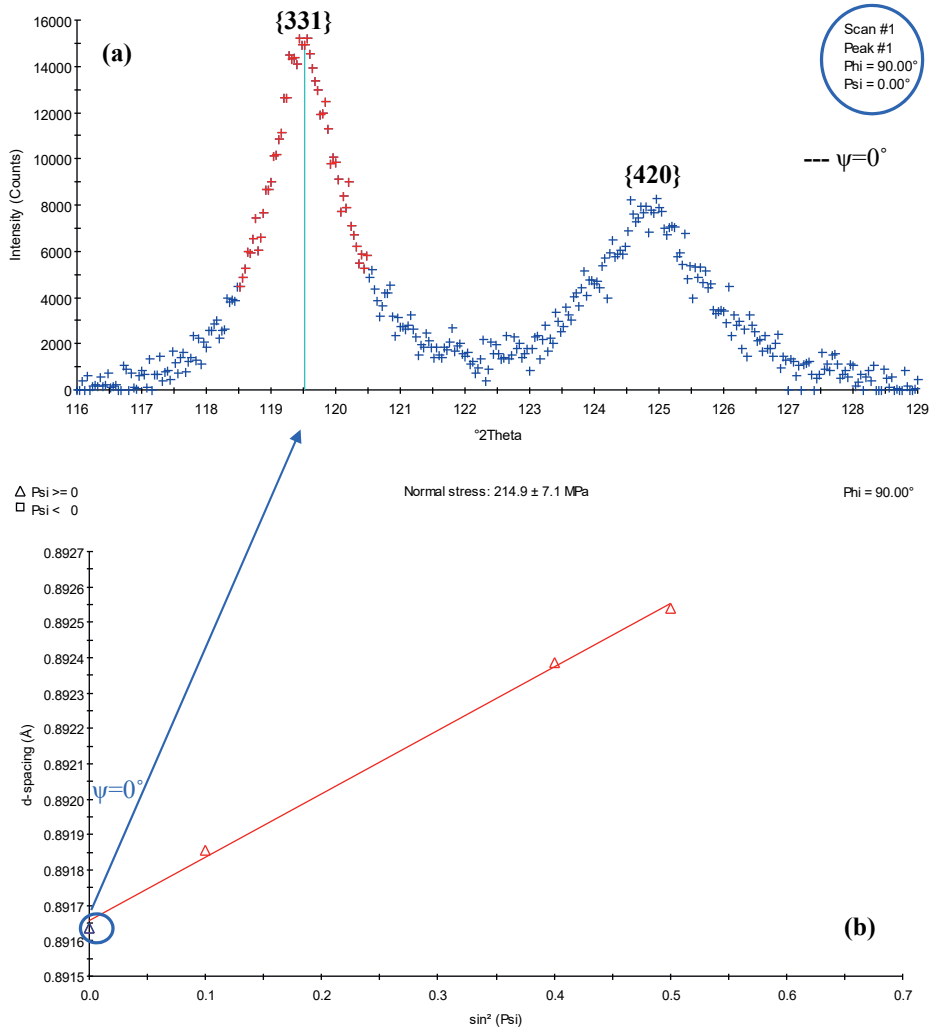


Figure B14 – Pd-PI-SiO₂/Si film omega-offset stress after 1st deloading cycle. (a) From Figure B3(b) 2θ scan at $\psi=0^\circ$: lattice spacing evaluated by fitting profile with the Centered Center of Gravity method using threshold intensity above 40% of the maximum intensity. Absorption/transparency correction, background subtraction, LP correction, and $K\alpha_2$ -stripping, as intensity corrections were applied before fitting. (b) Plot of $d(hkl)$ vs $\sin^2\psi$ for Pd-{331} reflection. Fittings performed on the X'Pert Stress Plus software package.

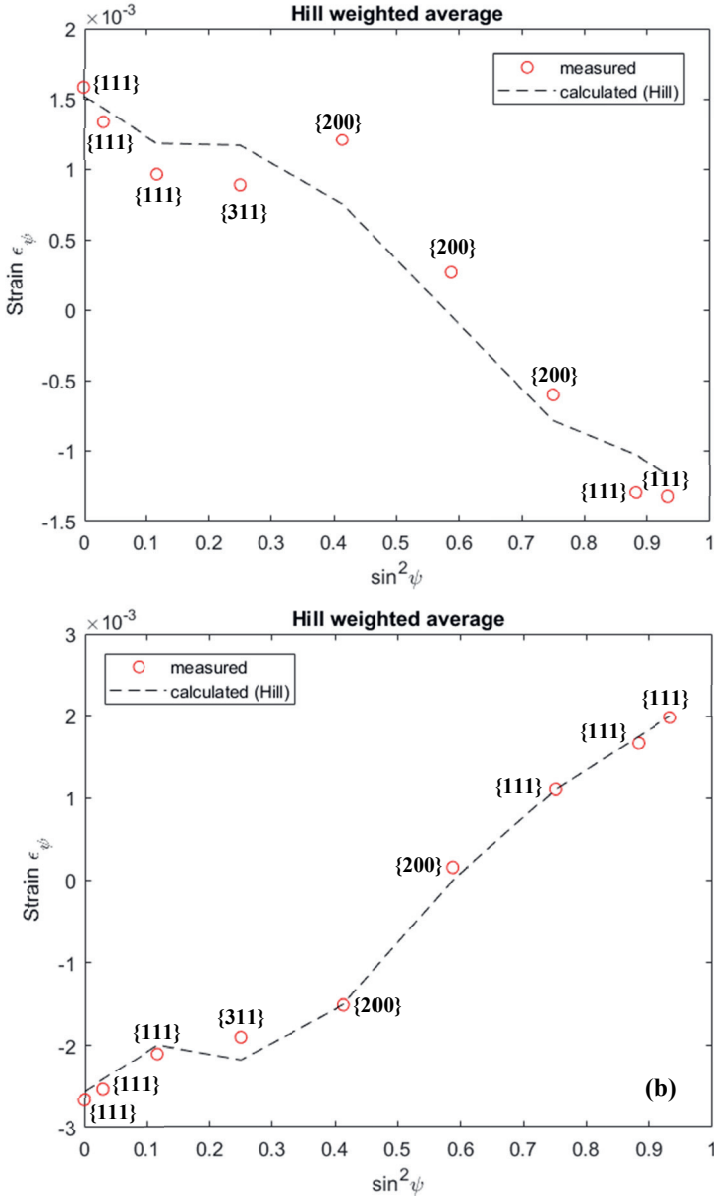


Figure B15 – Measured (o) and calculated (----) strain as a function of $\sin^2 \psi$ ($\sin^2 \psi$ plot), for the Pd-{111} oriented grains (multiple reflections are combined in a stress analysis). The calculated dashed lines are plotted using thin-film single-crystal compliances s_{11} , s_{12} , and s_{44} obtained from the least-squares process, using Hill's weighted average grain-interaction model. (a) loading plot and (b) deloading plot for Pd-Ti-SiO₂/Si film.

Table B1 – The mechanical stress evaluated by fitting the calculated strain to the measured strain by the use of a least-squares minimization of the difference χ^2 . Strain-free lattice constant as an additional fit parameter*.

$$\chi^2 = \sum_{i=1}^N (\varepsilon_i^{cal}(\sigma_{ll}, hkl, \psi) - \varepsilon_i^{meas}(hkl, \psi))^2$$

Pd on Ti	a_0 (Å)	χ^2	Stress (MPa)	Pd on Pt	a_0 (Å)	χ^2	Stress (MPa)
As-dept	3.89	5.9E-07	170	As-dept	3.89	3.4E-07	100
1st-L	4.03	1.1E-06	-90	1st-L	4.03	8.3E-07	-115
1st-D	3.89	2.0E-07	425	1st-D	3.89	6.9E-07	390
5th-L	4.03	1.0E-07	-325	5th-L	4.03	1.0E-06	-295
5th-D	3.89	9.6E-08	540	5th-D	3.89	2.5E-07	430
10th-L	4.03	9.1E-07	-450	10th-L	4.03	7.2E-07	-325
10th-D	3.89	1.4E-07	595	10th-D	3.89	3.9E-07	380
15th-L	4.03	8.7E-07	-490	15th-L	4.03	5.7E-07	-320
15th-D	3.89	5.6E-07	600	15th-D	3.89	1.7E-07	335
20th-L	4.03	1.3E-06	-485	20th-L	4.03	5.1E-07	-290
20th-D	3.89	4.1E-07	620	20th-D	3.89	1.2E-07	300

*Lattice parameter (a_0) literature value; Pd = 3.890 Å (Joint Committee on Powder Diffraction Standards 2000).

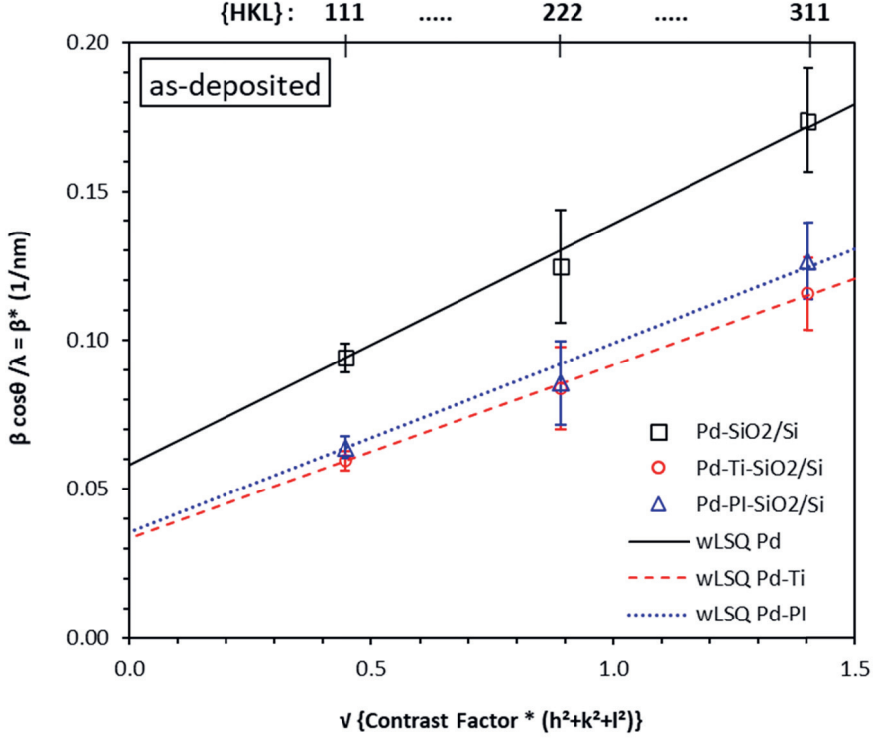


Figure B16 – The mod-WH plots for as-deposited Pd-SiO₂/Si, Pd-Ti-SiO₂/Si, and Pd-PI-SiO₂/Si films showing β^*_{hkl} versus C_{hkl} for randomly oriented screw dislocations with Burgers vector $a/2\langle 110 \rangle$ and glide plane $\{111\}$. The error bars shown are +3 and -3 times the standard deviation (see Eq. 5.3 in Chapter 5).

Acknowledgements

“Acknowledging the good that you already have in your life is the foundation for all abundance.”

—Eckhart Tolle

All these years, I imagined so many times writing this acknowledgement and finally, when the time has come when it is actually happening, my heart is only full of gratitude to acknowledge this reality. This long journey, with its all ups and downs, is now being logically concluded only because of the incredible support that I have received from so many people to whom I would like to convey my deep heartfelt gratitude.

First of all, I wish to extend my sincere gratitude to my daily supervisor Dr. Amarante J. Böttger for offering me this opportunity to pursue a PhD at TU Delft which was my then dream. I highly acknowledge and appreciate her dedicated guidance, great patience, and tremendous commitment for all these years. Amarante, I am eternally grateful to you for offering me your endless support, especially after I had moved out of TU Delft. Thank you for staying constantly in contact through emails and providing multiple guest contracts because of which I could conclude my PhD thesis.

I would like to extend my special thanks to my former promotor Prof. dr. Barend Thijsse in heaven for the valuable discussions on the topics relating to vast materials science. With his effortless and witty style, he taught us how to tackle challenging and complex problems and solve them effectively and independently. I will be ever grateful for his guidance and am sorry that he has not lived to see me graduate. I am very grateful to Prof. dr. ir. Jilt Sietsma for stepping in as my promotor at the very crucial stage of my PhD. I had heard so much about his gentle mentoring styles from MSE friends and colleagues that I feel so fortunate to have experience his guidance and support to reach the end of my PhD journey. A warm thank you!

Next, I would like to express my great appreciation to all my brilliant X-ray Diffraction lab technical staff colleagues, Niek van der pers, Dr. Rob Delhez, Ruud Hendriks, and Richard Huizenga. Niek, you generously helped me in planning my experiments, which demonstrably enhanced the quality of my research. Our spontaneous discussions at your desk in the XRD lab were incredible because of your enthusiasm and vast experience in x-ray diffraction. Rob,

I want to thank you from the bottom of my heart for your constant support and guidance all these years, most importantly for always being so kind, considerate, and caring towards me. This work would not have achieved significant progress without your contributions. A warm thank you! Ruud, without your help I would have never finished the XRD measurements. Thank you for all the efforts that you have put into this research work.

I would also like to thank the technicians of 3mE for the training sessions, and technical support in the labs of 3mE, TU Delft. Special thanks to Kees Kwakernaak and Hans Brouwer for SEM assistance, and Rob Luttjeboer for AJA sputter deposition assistance.

I am thankful to Dr. F.D. Tichelaar at the HREM group at the Kavli Institute for Nanoscience, TU Delft for the TEM images and data for this research.

I also wish to thank the management and support staff of the MSE department, Anke Kerklaan-Koene, Annemart Berendse, Mascha Toppenberg, Olaf Voorwinde, Saskia Brandt Corstius, Prisca Koelman, Saskia van der Meer, all of you were always happily willing to provide administrative assistance. Thank you!

Some of the best moments outside of work were the ones that I spend with my friends and colleagues from TU Delft. Many cordial thanks to Zeynep, Sebastian, Fidel, Vanya, Girish, Vahid, Yaiza, Olga, Georgina, Yulia, Gorze, Onaz, Ann-Sophie, Alexandra, Linda, Lu Shen, William, Ranjita, Casper, Syam, Kelvin, Jaysree, and Astrid for a great companionship. Special thanks to Vanya Uluc for all the discussions and assistance with cyclic voltammetry experiments. My appreciation and gratitude to Girish Kotnur for sputter deposition training sessions and also for always being there every time I was stuck with the instrument in the sputtering lab.

And, I must also thank my friends outside TU Delft who helped to bring a perfect work-life balance into my life. Thank you, Jyoti, Jeetu, Nalini, Geetha, Sakshi, Kishore, Venkat, Mahir, Aygul, Mohit, Vinod, Melaine, Jasvir, Manu, Vikram, Vishal, Jenny, Akshay, Juljia, and Deepak for a great friendship and an incredible Indian experience here in Europe. Meesha and Yashu, thank you buddies for your friendship which never lost its warmth despite of long distances between us. If I have missed thanking anyone here, it is not deliberate.

I wish to also express my gratitude to my former colleagues at the Conservation & Science department, Rijksmuseum, Amsterdam for an incredible time working on the material-historical aspects of Rijksmuseum's important collection of Dutch Delftware. Thank you,

Jolanda, Isabelle, Femke, Guus, Arie, Judith, Luc, and Annelies for being supportive, motivating, and a kind team to work with at one of the coolest places to work.

A ‘thank you’ cannot bear the weight of feelings that I have for my wonderful family for their endless love, support, patience, and encouragement. The unconditional faith of my parents in me and my decisions has been a constant source of all positivity and hope in my life. Thank you, Nikhil, Deepu, and Bhanu for taking care of our parents when I am away and living my professional pursuits. The consistent motivation, understanding, and belief of my soulmate, Ashu, and the infinite affection of my beloved son, Krishiv continues to provide all the strength I need in my life. This PhD research is dedicated to you guys.... Love you all!

Neha

India, June 2022

Publications

- N. Verma, R. Delhez, N.M. van der Pers, R.W.A. Hendrikx, R.M. Huizenga, A.J. Böttger, *Dislocations, texture and stress development in hydrogen-cycled Pd thin films: An in-situ X-ray diffraction study*, **International Journal of Hydrogen Energy**, 47, (2022), pp. 121119-12134, doi: [10.1016/j.ijhydene.2022.01.233](https://doi.org/10.1016/j.ijhydene.2022.01.233)
- N. Verma, R. Delhez, N.M. van der Pers, F.D. Tichelaar, A.J. Böttger, *The role of the substrate on the mechanical and thermal stability of Pd thin films during hydrogen (de) sorption*, **International Journal of Hydrogen Energy**, 46, (2020), pp. 4137-4153, doi: [10.1016/j.ijhydene.2020.10.163](https://doi.org/10.1016/j.ijhydene.2020.10.163)
- N. Verma, G. Krishnamurthy, F.D. Tichelaar, A.J. Böttger, *Controlling morphology and texture of sputter-deposited Pd films by tuning the surface topography of the (Ti) adhesive layer*, **Surface and Coatings Technology**, 359, (2019), pp. 24-34, doi: [10.1016/j.surfcoat.2018.12.053](https://doi.org/10.1016/j.surfcoat.2018.12.053)
- N. Verma, A.J. Böttger, *Stress development and adhesion in hydrogenated nano-columnar Pd and Pd/Ti ultra-thin films*, **Advanced Materials Research**, 996, (2014) pp. 872-877, doi: [10.4028/www.scientific.net/AMR.996.872](https://doi.org/10.4028/www.scientific.net/AMR.996.872)

Curriculum vitae

Neha Verma

Born on 01st December 1985 in Shimla, India

Jan. 2019 – Present

Stay at Home Mom
Tübingen, Germany

Jan. 2016 – Oct. 2018

Research Analyst
Conservation & Science department
Rijksmuseum
Amsterdam, The Netherlands

Oct. 2011 – April 2022

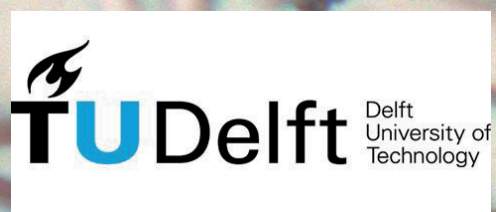
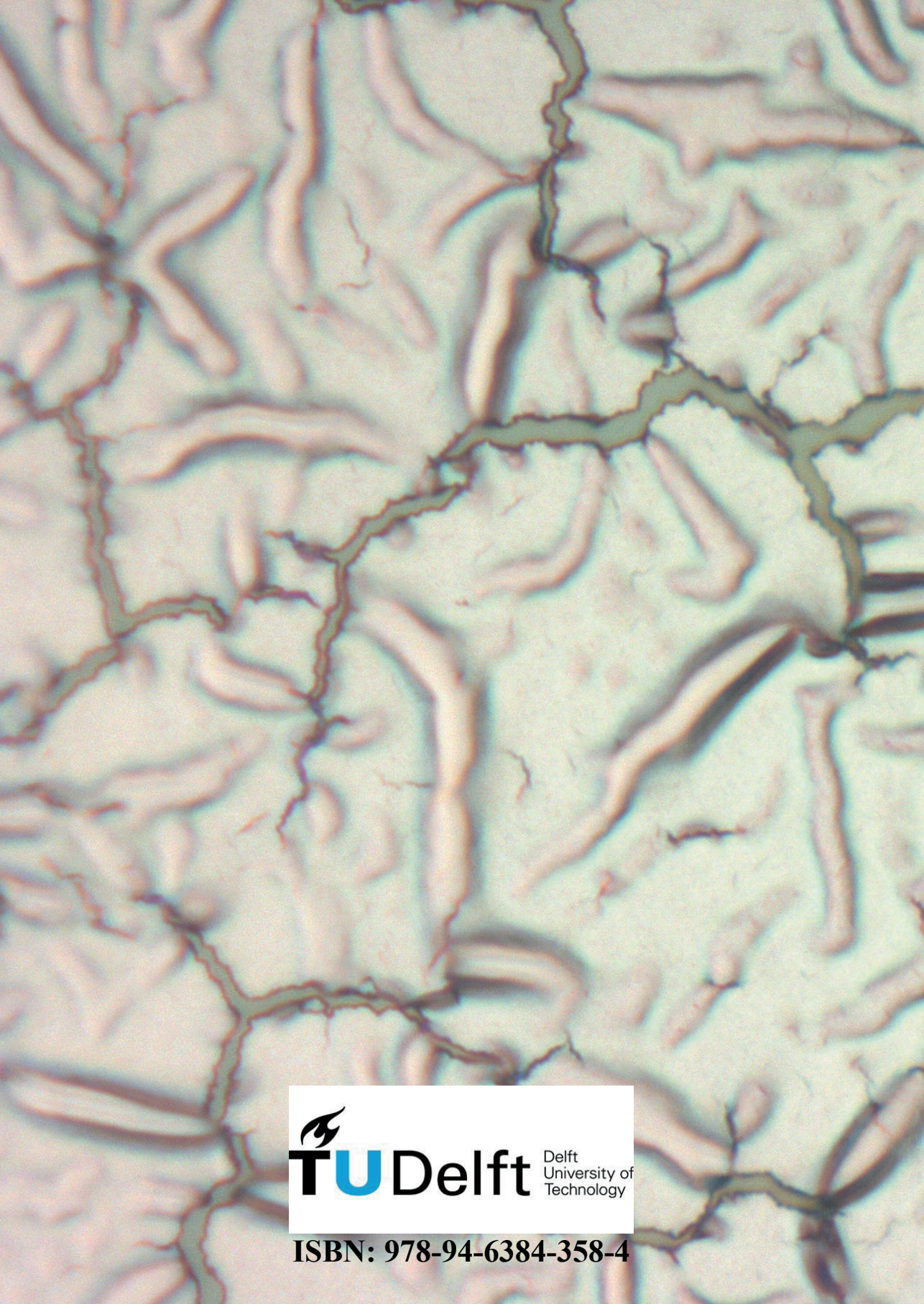
Doctor of Philosophy
Interfaces
Materials Science and Engineering
Delft University of Technology
Delft, The Netherlands

Sept. 2009 – May 2011

International Master's Degree Programme for Research Chemists
Advanced studies in Materials Chemistry
University of Eastern Finland
Joensuu, Finland

Sept. 2007 – May 2009

Master of Science (Honours School) in Chemistry
Department of Chemistry
Panjab University
Chandigarh, India



ISBN: 978-94-6384-358-4